Synthesis of 2D Janus Crystals and their Superlattices

by

Mohammed Yasir Sayyad

A Thesis Presented in Partial Fulfillment
of the Requirements for the Degree
Master of Science

Approved April 2020 by the
Graduate Supervisory Committee:

Sefaattin Tongay, Chair
Peter Crozier
Terry Alford

ARIZONA STATE UNIVERSITY

May 2020

ABSTRACT

Two dimensional (2D) Janus Transition Metal Dichalcogenides (TMDs) are a new class of atomically thin polar materials. In these materials, the top and the bottom atomic layer are made of different chalcogen atoms. To date, several theoretical studies have shown that a broken mirror symmetry induces a colossal electrical field in these materials, which leads to unusual quantum properties. Despite these new properties, the current knowledge in their synthesis is limited only through two independent studies; both works rely on high-temperature processing techniques and are specific to only one type of 2D Janus material - MoSSe. Therefore, there is an urgent need for the development of a new synthesis method to (1) Extend the library of Janus class materials. (2) Improve the quality of 2D crystals. (3) Enable the synthesis of Janus heterostructures.

The central hypothesis in this work is that the processing temperature of 2D Janus synthesis can be significantly lowered down to room temperatures by using reactive hydrogen and sulfur radicals while stripping off selenium atoms from the 2D surface. To test this hypothesis, a series of controlled growth studies were performed, and several complementary characterization techniques were used to establish a process–structure-property relationship. The results show that the newly proposed technique, namely Selective Epitaxy and Atomic Replacement (SEAR) is effective in reducing the growth temperature down to ambient conditions. The proposed technique benefits in achieving highly crystalline 2D Janus layers with an excellent optical response. Further studies herein show that this technique can form highly sophisticated lateral and vertical heterostructures of 2D Janus layers. Overall results establish an entirely new growth technique for 2D Janus

layers which pave ways for the realization of exciting quantum effects in these materials such as Fulde–Ferrell–Larkin–Ovchinnikov (FFLO) state, Majorana fermions, and topological p-wave superconductors.

ACKNOWLEDGMENTS

I am forever grateful to faith Dr. Tongay showed in a failing student such as me. He gave me an opportunity during the most challenging phase of my academic life. His constant encouragement helped me overcome academic probation, made me a better student, and further instilled in me the desire to pursue research with passion and enthusiasm. His immense knowledge in the field of 2-Dimensional materials has helped me through my journey as a master's student. I cannot think of a better advisor with such strategic guidance and enthusiasm towards every project I was involved at Arizona State University.

I would like to thank Dr. Guven Turgut and Dipesh Trivedi. You guys nurtured me during my initial phase at the 2D lab. Without your support in my research, I would have never learned CVD or let alone create any of the materials I have mentioned in this thesis. Next, I want to express my sincerest gratitude to Pranvera Kolari; you helped under challenging phases of my academic and social life. Without you, I would have never had such a different outlook on my life, I therefore cannot thank you enough for everything you've done for me.

I want to thank Ying Qin, your constant encouragement and bickering made me a better researcher and more proficient in my presentations and optical techniques. I want to thank Mark Blei; you always supported me in my work and continuously gave me new ideas to explore. I want to thank my fellow undergraduate students, Michael Durso, Patrick Hays, and Jeannie Kim. They undertook many of the time-intensive measurements on AFM and Raman setups. Without your exfoliations and datasets, I couldn't have compiled this thesis.

I am also thankful to all the group members, Silje, Debarati, Han, Kentaro, and Yuxia, for their much-needed ideologies and unceasing assistance on my projects. I am forever grateful to Benjamin Shindel, Amey Luktuke, Ronit Sawant, and Sagnik Dasgupta; without you guys, I would have never made it through my first semester at ASU.

A word of thanks to various collaborators from ASU and beyond, for their contribution to my research and for providing me with eloquent results that supported my conclusions more effectively. Special thanks to - Dr. Nathan Newman and Richard Hanes for helping me set up the plasma system, To Fred Pena, for helping me sort the grounding issues on the Z-Match, to Dr. Houlong Zhuang for providing the DFT calculations without which we would have never proven Janus. To Dr. Arshad Sayyad, Rakshanda, and Karishma for helping me during my initial days in the US.

Lastly, I am indebted to my family, who always supported me throughout my journey.

TABLE OF CONTENTS

Page

CHAPTER Page

CHAPTER Page

LIST OF TABLES

Table Page

LIST OF FIGURES

Figure Page

Figure Page

Figure Page

Figure Page

1. Chapter 1 Introduction

1.1. Graphene: a Brief History

Carbon is my favorite element. Often considered the *materia prima* of life, carbon forms the backbone of organic chemistry. The excellent flexibility of its bonding allows it from unique structures with novel mechanical, electronic, magnetic, and optical properties, i.e., Allotropes of Carbon. Hypothetically more than five hundred of these allotropes of carbon have been predicted, many of which have been experimentally realized and researched [1]. Of these, **Graphene**, a two-dimensional allotrope, gained considerable attention over the last decade and paved the way for the emergence of a two-dimensional materials field [2].

Although Graphene was theoretically predicted in 1947 by P.R Wallace, who first predicted its unusual semi-metallic behavior [3], it was not until 2004, when Novoselov and Giem successfully isolated graphene from Graphite, was it rediscovered [2]. The delay in the discovery is partly attributed to two reasons: (1) No one expected Graphene to be stable, and the idea of a purely 2D structure was not a reality since Wallace's time, (2) No experimental tools existed to search monoatomic thin flakes.

It was after Novoselov showed that graphene could be spotted due to a subtle optical effect it created on top of a chosen SiO2 structure that allowed for its observation using an ordinary optical microscope [4]. Graphene is often projected as a wonder material due to its many fascinating properties. Despite being atomically thin, it is impermeable to gases and liquids [5]. It is more robust and stiffer than diamond and still can be stretched by a quarter of its length; in fact, its surface area is largest known for its weight. Thanks to

its excellent mechanical flexibility and durability, graphene was soon seen as structural enhancement material, and it was employed as a constituent in composite materials[6, 7]. However, it is the unusual electronic properties that make graphene genuinely remarkable and worthy of its namesake as a wonder material.

Graphene has superb carrier mobility, extraordinary optical transparency, and incredible stability, which has led researchers to speculate its use in electronics[8]. Not only does it conduct heat and electricity better than copper, but its robust ambipolar electric field effect [9] [10] and high room temperature mobility [11] has also allowed researchers to fabricate metallic transistors, which are much faster than those made from silicon[12]. Arranged in a honeycomb structure made up of hexagons, graphene can be imagined as a ring of benzene stripped out of their hydrogen atoms, as shown in Figure1.1[13].

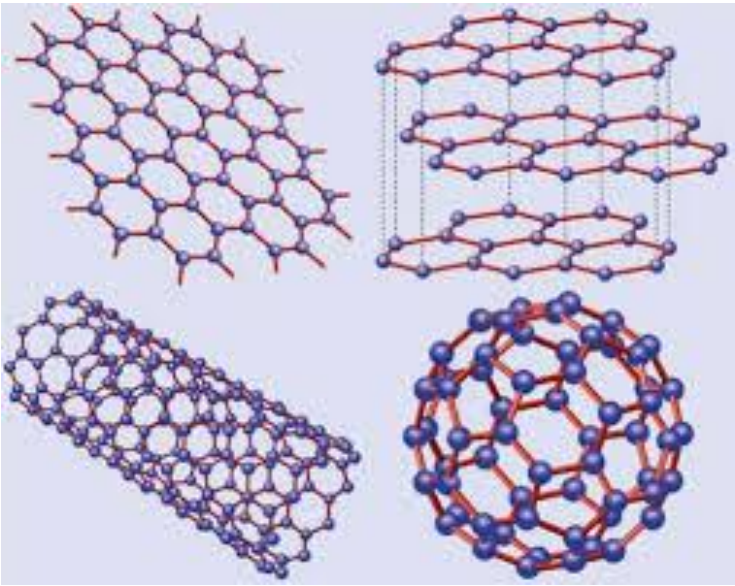

Figure 1.1 Graphene as a building block in various allotropes of carbon.

Panel adapted with permission from ref [8] American Physical Society.

It plays a vital role amongst other allotropes of carbon since it is used to define their electronic properties. Many other forms of carbon can be thought of as structures composed of graphene as its building block. Graphite, for instance, a 3D allotrope of carbon consists of sheets of graphene stacked on top of one another and held together by Vander walls force. Similarly, carbon nanotubes are obtained by rolling graphene along a given direction and reconnecting the carbon bonds. This extraordinary structural flexibility of graphene is resonated with its electronic properties. The sp^2 hybridization between the *1s* and *2p* orbitals leads to a trigonal planar structure, where a σ bond is formed between carbon atoms 1.42 Å apart [2]. This σ bond is responsible for the sturdiness of the lattice structure in all allotropes. Because of Pauli's exclusion principle, the bond has a completely occupied shell and, as a result, forms a deep valence bond. On the contrary, the p orbital, which is perpendicular to the planar structure, is mostly unaffected and binds covalently with neighboring carbon atoms. This leads to the formation of a π bond. Due to the extra electron within each p orbital, the π bond is partially filled. This peculiarity plays a crucial role in the physics of strongly correlated systems.

The Coulomb energies in such systems are mainly due to the strong, tight binding characteristics and often lead to strong collective effects. Examples of such effects include magnetism and Mottness (insulating behavior due to correlation gaps) [14]. Another critical aspect of graphene is the unusual two-dimensional Dirac like electronic excitation, which can be controlled by the application of external electric and magnetic fields Or by alternating the sample geometry or topology[15]. These Dirac electrons behave in unusual ways in tunneling, confinement, and integer quantum Hall effect[16]. The Dirac fermions

in graphene are massless chiral excitations and mimic the physics for quantum electrodynamics for massless fermions except that in graphene, the Dirac fermions move with the speed $\upsilon_{f,}$ and hence many unusual properties of QED show up in graphene but at lower speeds[17]. The Dirac electrons are particularly vital because they behave in a different way when compared to the ordinary electrons if subjected to magnetic fields, leading to a new quantum phenomenon [15]. Examples of such effects include anomalous integer quantum Hall effect observed in graphene at room temperature because of enormous cyclotron energies for relativistic electrons[18], a trait that makes it different from other material systems such as Si and GaAlAs for which IQHE is observed[16, 19, 20].

Under certain conditions, the Dirac electrons are immune to localization effects that are observed in ordinary electrons. This behavior arises due to the insensitivity of the Dirac fermions to external electrostatic potentials due to the Klein paradox[21, 22]. Entirely, on the contrary, the Dirac fermions behave unusually in the presence of confining potentials leading to Zitterbewegung motion of the wave function [23]. Another important aspect is the layer dependence in graphene. The stacking can change the electronic properties considerably, and the layering structure can be used in order to control the electronic properties [24]. This, when coupled with the chiral Dirac nature of fermions in graphene, makes them a potential candidate for valleytronics applications [25].

Furthermore, the existence of supercurrent flow and Andreev processes characteristic of the superconducting proximity effect has been shown when superconducting contacts are attached to graphene [26]. Interestingly due to the robust

electronic coherence of graphene, Cooper pairs are shown to propagate well in graphene[27]. In addition to this, quantum interference phenomena such as the Aharonov-Bohm effect[28], universal conductance fluctuations [29] as well as weak localization [30] have all been experimentally realized in graphene rings. Furthermore, the ballistic electronic propagation in graphene can be used for p-n field-effect devices [31]. Since the Coulombic interactions are enhanced in smaller geometries, for instance, graphene quantum dots [32-34], magnetic phenomenon such as the Kondo effect and unusual Coulomb blockade effects can also be observed in such confined geometries [35, 36].

Although the 2D materials field is still in its infancy, the unique structural and electronic properties observed in graphene has sparked tremendous interest in other 2D systems, particularly Transition Metal Dichalcogenides (TMD) [37]. Over the last decade, substantial economic resources have been devoted to study these systems. The scientific and technological opportunities for the materials seem to be unlimited, and a thorough comprehension of their properties can open doors for a new frontier in electronics and quantum technology [38]. Thus graphene, a material only two decades old, has paved the way for an emergent scientific field and hence propelled us into the quantum age.

1.2. 2D Layered Materials.

Two-dimensional layered **materials** are crystalline **materials** consisting of a single layer of atoms. These materials are usually categorized either as two-dimensional allotropes of various elements such as graphene, phosphorene, silicene, etc. or compounds consisting of two or more covalent bonding elements Hexagonal boron nitride, Boron

carbides, Germanane and TMDS [39, 40]. Layered combinations of different two-dimensional materials are called Vander walls heterostructures and are fabricated to tailor material properties to specific applications. Many two-dimensional layered materials are under close consideration for use in several industries and scientific thrusts, examples of which include optoelectronics[41], valleytronics [42], Quantum computing and cryptography [43], biological engineering, photovoltaics [44], medicine, quantum dots, thermal management, and energy storage, etc. [45-47].

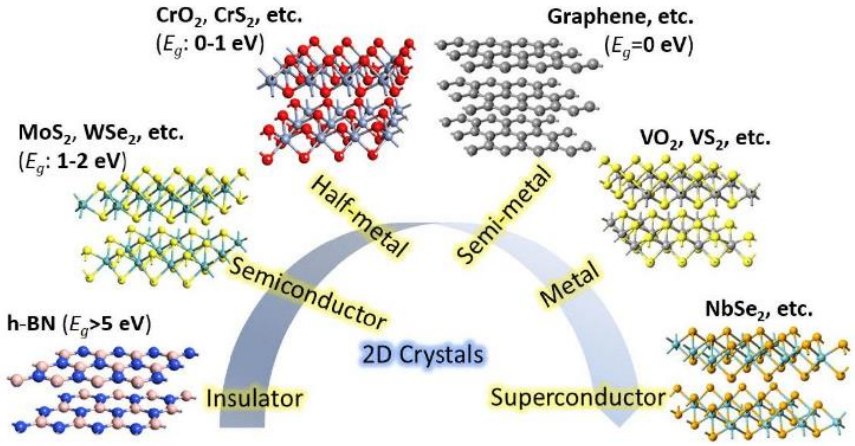

Figure 1.2 Family of various 2D material.
panel adapted with permission from ref [48], MDPI

1.2.1. Transition Metal Chalcogenides.

Atomically thin materials often exhibit remarkable physical properties resulting from the quantum confinement effect and crystal symmetry [49]. The best example of such systems remains graphene, which is very popular because of its many fascinating properties; however, the lack of an electronic bandgap has stimulated the search for two-dimensional materials with semiconducting character [2]. The family of two-dimensional transition metal dichalcogenides, which are semiconductors of the type MX_2 (where M is

a transition metal such as Molybdenum, Tungsten, or Niobium, and X is chalcogen atom such as Sulfur, Selenium or Tellurium) are an especially promising candidate [50].

TMDs have been under close consideration for potential application is valleytronics and optoelectronics due to their highly efficient light-matter coupling [42]. The broken inversion symmetry in these materials, in addition to the strong spin-orbit coupling, leads to a unique combination of valley and spin degrees of freedom. The monolayers are stable under ambient conditions when thinned down from their bulk counterparts that exist in a 2H phase and consist of X-M-X building blocks with weak van der Waals bonding in between the layers. These crystals are characterized by D_{6H} point group symmetry for stochiometric compounds [51]. Compared to the bulk samples, the monolayer TMDs are characterized by a lower symmetry point group D_{3H}. In bulk TMDs, the indirect bandgap is associated with the conduction band minimum (CBM) being located at the halfway point between Γ- K, in the first Brillouin zone, and the valence band maximum (VBM) being located at the Γ point at the center of the Brillouin zone [52]. The p_z orbitals from the chalcogen atoms and the d_z^2 contribute to the electronic states at this Γ point. Whereas, the electronic states associated with the K± point conduction and valence band states are very strongly localized in the metal atom plane. They contain a contribution from $d_{x^2-y^2} \pm id_{xy}$ states (VB) and d_z^2 states (CB) for transition metal atom and are slightly mixed with $p_x \mp ip_y$ orbital for the chalcogen atom [52]. There is considerable spatial overlap between adjacent MX_2 layers of the orbitals corresponding to the center of the Brillouin zone at the Γ point (VB) and the midpoint along Γ- K (CB). When one progresses from the bulk to a

monolayer sample, the indirect gap energy corresponding to the separation between the Γ and Γ-K increases.

In contrast to this, the K± point CB and VB energies remain unaffected. In the monolayer limit, the semiconductor undergoes a crossover to a direct bandgap from an indirect one, with the former being situated at the K± point; this results in a much stronger light emission for the monolayers.

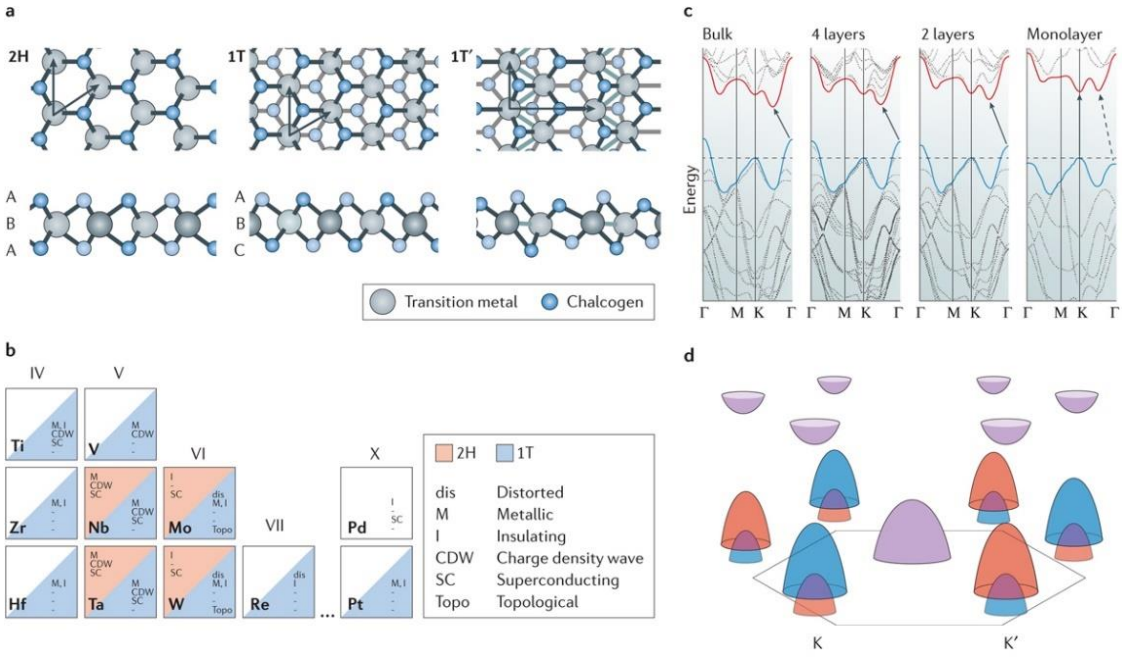

Figure 1.3 Structure and electronic properties of TMDS

(a) Various Phases in 2D materials **(b)** 'Periodic table' of known layered TMDCs, **(c)** band transition due to quantum confinement effect **(d)** band structure of monolayer 2H-MoS_2, showing the spin splitting of the bands. *The panel is adapted with permission from ref [37], Springer Nature.*

Additionally, The optical transitions at the bandgap are valley selective, and one can induce optical transitions at K+ or K- valleys using a circularly polarized light σ+ or σ- respectively. The presence of a direct gap is particularly interesting for potential device

applications, and promising device prototypes have already been demonstrated with various functionality, including phototransistors [53].

Compared to graphene, monolayer TMDS shows the presence of strong spin-orbit interactions, which introduce spin splitting of few to tens of meV in the conduction bands and several hundred meV in the valence band [54]. These spin states in the inequivalent valleys k+ and K− are linked by time-reversal symmetry. The spin-orbit interaction in transition metal dichalcogenides is stronger than in graphene since spin-orbit interaction is a relativistic effect and is more pronounced in TMDs due to the relatively heavy elements in the TMDs and the involvement of the transition metal d orbitals [55].

Furthermore, a significant enhancement of the Coulomb interaction is also observed in the 2D monolayers, and this is generally attributed to the weak dielectric screening from the environment. Since their inception in 2010 [53], the properties of these dielectric gap monolayers with valley selective optical selection rules have been extensively studied using linear as well as nonlinear optical spectroscopic techniques. In bulk semiconductors, an electron is promoted to the conduction band after the absorption of a photon of suitable energy, thus leaving behind a hole in the valence band. In TMD monolayers, however, the electron and the holes are tightly bound together due to the Coulomb interaction and results in the formation of bound electron-hole pairs (excitons) with typical binding energies of the order 0.5 eV. Formation of excitons in these material systems dominates the optical and spin properties at cryogenic as well as room temperature At the corresponding transition energies, the interaction of light with matter is strongly enhanced in comparison to the transitions in the continuum of unbound electrons and holes.

In addition to spin-orbit coupling, the Coulomb interaction in monolayers contributes to the splitting between optically bright and dark exciton states and determines the valley polarization dynamics of excitons. In conclusion, the physics of these excitons are of fundamental interest for engineering and exploiting the properties of these materials in potential device applications.

1.3. Group VI Transition Metal Chalcogenides

1.3.1. Molybdenum Based TMDs

Molybdenum based TMDS are metal dichalcogenide materials of the MX_2 type, where molybdenum serves as the transition metal (M). Within the family of Moly based TMDs, all three known variants, i.e., Molybdenum Sulfide (MoS_2), Molybdenum Selenide ($MoSe_2$), and Molybdenum Telluride ($MoTe_2$) exist, with MoS_2 and $MoSe_2$ being stable at room temperature. Molybdenum Telluride is unstable at room temperature and gradually oxidizes into molybdenum dioxide (MoO_2) [56].

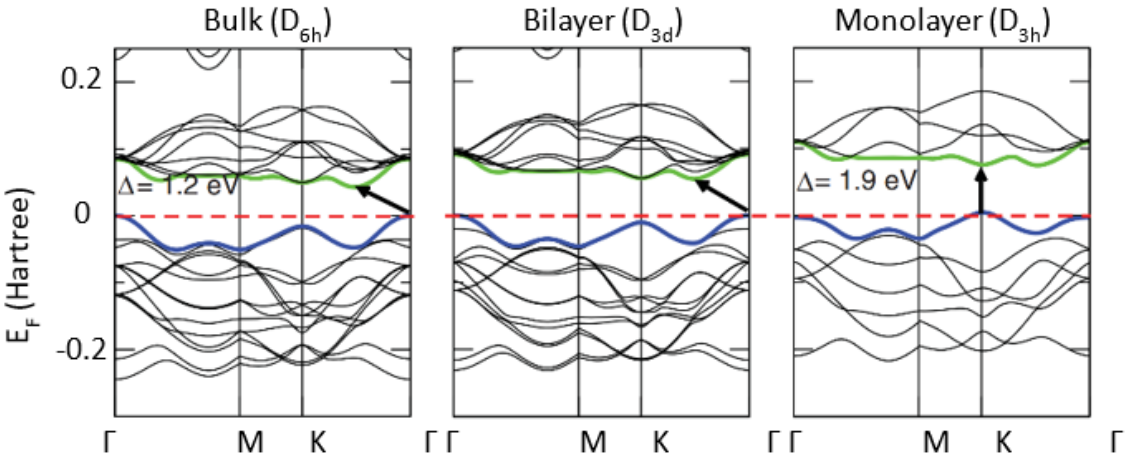

Figure 1.4 Band renormalization in MoS_2,
panel adapted with permission from ref [57], American Physical Society.

The crystal structure in these materials results from the stacking of sheets of hexagonally packed atoms, with two chalcogen atom separated by a plane of metal atoms, thus forming a three-layer configuration packed together by covalent bonds. A single sheet of three-layer atoms is referred to as a monolayer, and multiple stacks of monolayer sheets have held one another by van der Waals bonds that are much weaker than covalent bonds. Bulk TMDs can exist in several varieties of polyforms such as 1T, 2H, and 3R, where T, H, and R refer to trigonal, hexagonal, and rhombohedral[55, 58]. In contrast to this, monolayer TMDs such as MoS_2 ref. Fig1.4 exhibits only two polymorphs, both of which are directly related to metal coordination: trigonal prismatic (D3h point group) or octahedral (D3d point group)[37].

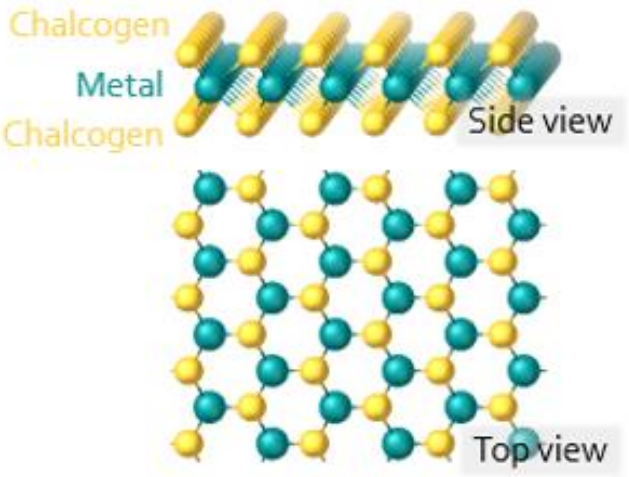

Figure 1.5 MoS_2 crystal structure

Of all the TMDs, MoS_2 is arguably the most extensively studied material within the two-dimensional materials community due to potential application in the lithium-ion battery (LIB)[59], the flexible electronic device [60], photoluminescence, valleytronics,

and field-effect transistors[61, 62]. The earliest report of synthesis date to 1963; however, the material gained extensive attention after a direct bandgap and photoluminescence were observed in monolayers in [53, 63]. Due to the research and development on the synthesis of graphene in the latter half of the decade, the methodology and growth routes were quite well-established and were quickly applied for the rapid, high-quality synthesis of monolayer TMDS [64]. Like graphene, Molybdenum can be obtained by mechanical exfoliation or solvent-based exfoliation methods [65, 66]. Mechanical exfoliation of the MoS_2 method always leads to the 2D trigonal prismatic structure labeled as H-MoS_2, which is semiconducting. Based on Density function Theory calculations H-MoS_2 phase has the space group of P6/mmc and is the most stable configuration under ambient conditions.[67]

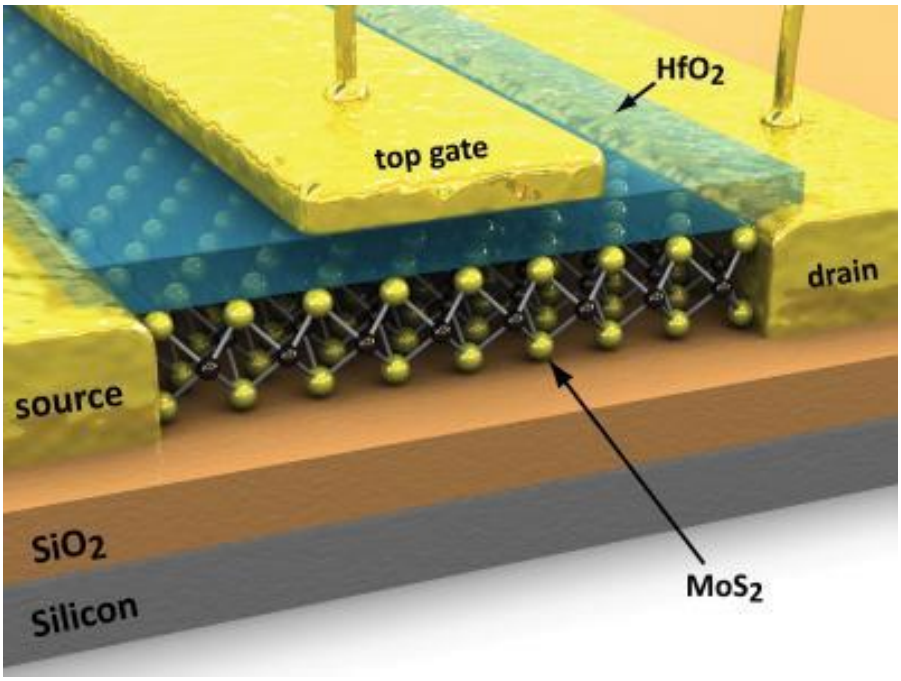

Figure 1.6 Encapsulated single-layer MoS_2 transistor.
Panel adapted with permission from ref [68], Springer Nature.

Solvent phase exfoliation is also another method of synthesis of 2D MoS_2 and results in octahedral configuration phases[69]. The trigonal prismatic H-MoS_2 has a bandgap of 1.67 eV, whereas the T-MoS_2, on the other hand, is metallic. It has been shown that the Li adsorption on the surface can induce a phase transformation from 2H -MoS_2 to an octahedral configuration [70]. Since exfoliation and the liquid phase solvent extraction yield quasi-2D material and is unreliable for an industrial scale-up, Synthesis monolayer TMD is mostly carried out by Chemical Vapor Deposition (CVD), Physical Vapor Deposition (PVD), Metal-Organic CVD (MO-CVD) and Molecular Beam epitaxy (MBE), etc.

The lack of bandgap in graphene has fundamentally restricted its use as a graphene field-effect transistor (FET) biosensor. This is mainly attributed to poor device performance due to increased leakage and reduced sensitivity [71]. MoS_2, on the other hand, is an n-type semiconductor bandgap of 1.67 eV, and gas sensing capability for monolayer MoS_2 has gained widespread attention over the last few years. MoS_2 has been proposed as a promising candidate for the detection of nitrogen dioxide, ammonia, and ethanol. Simple conductometric and FET devices fabricated from MoS_2 for the detection of solvents such as triethylamine have shown very promising results. Since the electrical resistance in FET MoS_2 can be tuned by gate bias, it makes the material more competitive for gas sensing compared to graphene [72, 73]. Apart from 2D monolayer devices, research groups have reported that different morphologies of MoS_2 exhibit different sensing properties compared to both its bulk and 2D counterparts. For Instance, an MoS_2/Si pn junction device, fabricated by magnetron sputtering, was shown to sense high

concentrations of ammonia, although with a low response (ΔG/G ≈19.1%@200ppm NH3) [74]

1.3.2. Tungsten Based TMDs

Atomic structure of the WX_2 (X = S, Se) monolayers at equilibrium belong to the symmetry D_{3h} group with tungsten and chalcogen atoms arranged in a hexagonal lattice. In bulk form, the monolayers are bonded together by the van der Waals force. In the bulk form, both WS_2 and WSe_2 are semiconductors with an indirect bandgap.[75] The indirect gap is formed between the valence band maximum (VBM) at the Γ-point and the conduction band minimum (CBM) locating on the S-Γ path where the energy gap of the bulk WS_2 0.909 eV is slightly larger than that of the bulk WSe_2 0.826 eV. [76]

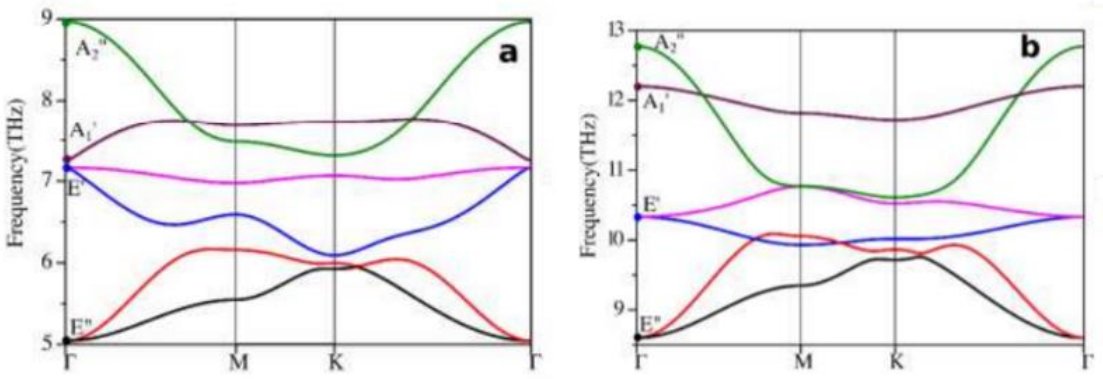

Figure 1.7 Phonon dispersion relation (a) WSe_2 (b)WS_2
Panel printed with permission from ref [77], Springer Nature.

Due to the quantum confinement effect, the electronic properties of the bulk crystal drastically change from their monolayer counterparts, undergoing an indirect to direct

bandgap transition in the monolayer limit. The phonon dispersion relations of the monolayers WSe_2 and WS_2 calculated from first principle methods are shown in Fig 1.8

It is evident from the given that there are no imaginary modes in the phonon spectrum of the monolayers implying that they are stable in their equilibrium state. First principle calculations show that at equilibrium, the band gaps of WS_2 and WSe2 monolayers are respectively 1.800 eV and 1.566 eV.

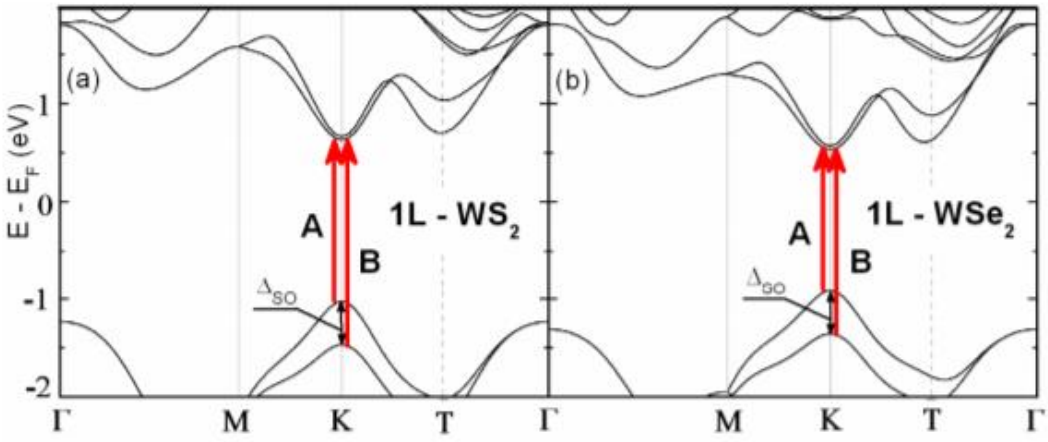

Figure 1.8: Calculated DFT electronic band structures of WS_2 and WSe_2 monolayer crystals. The red arrows indicate direct bandgap and the transition associated with the low-energy A and B excitons

Panel adapted with permission from ref [78], John Wiley and Sons

From a device application perspective, the characteristics of the backdated WSe_2 transistors with thick oxides are susceptible to the applied drain bias, especially for transistors in the sub-micrometer regime. The ambipolar conduction is essential for complementary metal-oxide-semiconductor (CMOS) circuits such as inverters, and since most TMDCs, such are naturally n-type doped they make an excellent choice for such applications[79]. Furthermore, the existence of room temperature ferromagnetism has been

shown to exist in Ni-doped WSe_2 [80]. Additionally, a significant enhancement in the device performance has also been observed in these monolayers by surface functionalization with cesium carbonate, with the photocurrent of the WSe_2-based phototransistor increasing by nearly three orders of magnitude [81].

1.4. 2D Janus TMD

1.4.1. Introduction

Asymmetric functionalization of monolayers to break its symmetry has received widespread attention over the past couple of years [82-86]. These materials are called "Janus," after the Roman god with two faces to emphasize the different material/properties they have on either face, as shown in Fig 1.8.

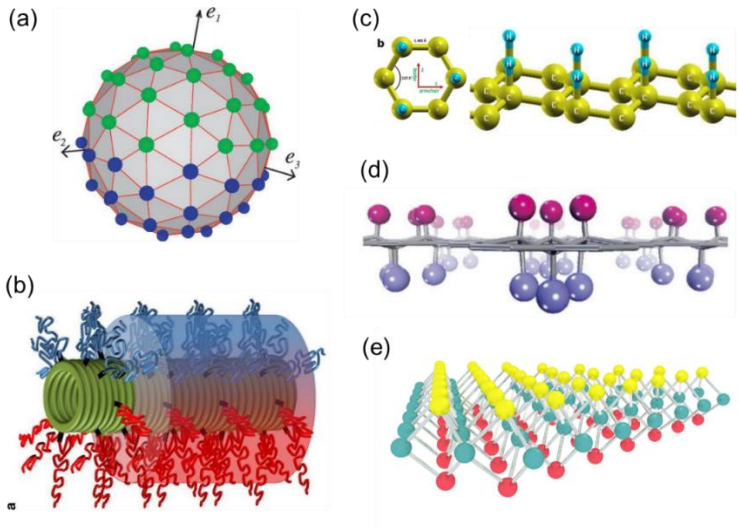

Figure 1.9 Different types of Janus materials

(a) 0D Nanoparticles (b)1-D nanotubes (c-d) Functionaalized graphene (e) 2D TMDs
Panel adapted with permission from ref [85], American Physical Society

The use of the “Janus” term dates in the scientific community dated to 1988 when Casagrande and his colleagues fabricated glass beads with hydrophobic properties on one side and hydrophilic features on the other [87]. Following this work, the use of Janus has expanded gradually, and the term is now commonly used to describe materials that have two vastly different chemical compositions and sometimes functionalities on each side. The rationale to create such materials stems can add more functionalities and is a way to engineer materials from a fundamental perspective

The first example of 2D Janus materials was seen in the form of asymmetric hydrogen functionalization of graphene called *graphane,* which consisted of hydrogenated graphene with H bonded on both sides of the carbon sheet [88]. Furthermore, the theoretical prediction of *graphane* sheets, have also shown selective hydrogen decorations mainly on one side of graphene, the resulting structure being named as *graphone*. Theoretical studies of this material have also shown that this new Janus material to be a ferromagnetic indirect bandgap semiconductor [89, 90]. Single-sided hydrogenated graphene has been reported to be a wide bandgap suitable for optoelectronic applications in the UV range [91].

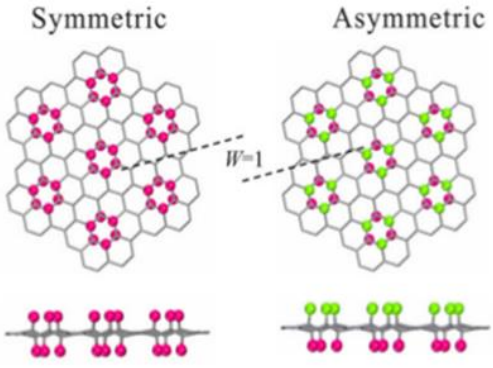

Figure 1.10 Symmetric and asymmetric arrangements of 2D Janus graphene layers
panel adapted with permission from ref [85], American Physical Society.

Surface functionalization in graphene has also been extended other chalcogens chlorine and Fluorine. For instance, Cl atoms tend to adsorb onto the graphene surface and form p-type doped, single-sided chlorinated graphene structures. The electronic bandgap for these structures shows a tunable bandgap ranging from 0 to 1.3 eV [92, 93]. Similarly, fluorine functionalized graphene sheet can be synthesized by exposing the graphene sheet to the XeF_2 atmosphere; it was demonstrated that the F coverage is almost saturated at 25%, yielding the formation of a C_4F structure [94]. The as-synthesized structure has been reported to be optically transparent and over six orders of magnitude more resistive than a graphene monolayer. Furthermore, other directions, such as the creation of asymmetric graphene layers, with two different types of atom on both sides of graphene, have also been reported [93]. For instance, a stable form of hydrogen fluorinated graphene has been proposed by saturating hydrogen and fluorine atoms on the wither end of the graphene sheet[95].

After successful synthesis of graphene-based Janus, recent experimental developments have also opened avenues for the synthesis of Two-Dimensional Janus TMDS. 2D TMDs exhibit many remarkable properties of graphene in addition to newer exotic quantum phenomenon such as Weyl fermions [96], Charge Density Wave (CDW) states, Type-II superconductivity [97], Tuneable Ising Pairing, [98], etc. However, asymmetric functionalization of these materials can potentially unlock much more substantial effects. For instance, in MoS_2, although the lack of inversion symmetry and spin-orbit coupling leads to spin and valley dependent behavior, lack of out of plane

potential gradient forbids phenomenon such as Rashba splitting which plays a vital role in potential spintronics and valleytronics applications [99]

1.4.2. Differences From Conventional TMDs

The idea for breaking the internal symmetry of monolayer TMDs was first proposed by Cheng et al.[99], by predicting the stability of polar single-layer TMDs. The proposed Janus structure MXY consisted of Metal atoms (M) that are sandwiched between two layers of different chalcogen atoms (X, Y) and comply with the same crystal structure as the parent TMD. The Janus monolayer structure evolves from TMD by completely replacing one layer of chalcogen atoms with another element of the same group [100].

Given the broken mirror symmetry, point group of monolayer changes from D_{3h} in TMDs to C_{3v} in Janus. The electronegativity difference between the top and bottom layer elements leads to asymmetric dipole distribution, which results in an intrinsic electric field build-up within the material, *within* the monolayer of the Janus structure. As a result of the polarization field, the top and the bottom layers of the Janus sheets have completely different potential energies, which has been predicted to be as high as 0.5 eV [85]. Symmetry breaking within Janus materials is also exciting and responsible for phenomena, such as phase transition, magnetism, ferroelectricity, and ferromagnetism [101]. DFT based calculation for several Janus materials has shown the phonon dispersion to be dynamically stable [83]. An exception, however, occurs, MoSeTe and MoSTe monolayers are predicted to be unstable. The phonon dispersion calculation for these monolayers shows apparent imaginary frequencies near the Γ point[102]. Recently the group three based Janus

chalcogenides have also been studied and predicted to be stable according to the formation of energy and phonon dispersion calculations.

1.5. Emergent Quantum properties of Janus TMD

A fundamental comprehension of the electronic structure is crucial in predicting the physical properties of materials. Studies on the band structures of 2D TMDs and their derivatives show that as a monolayer, the band structure in most TMDs changes from indirect to direct bandgap with tunable gaps, thus providing a high optical absorption coefficient for photovoltaic devices. The group-III chalcogenide Janus monolayers are shown to be semiconducting, with an indirect bandgap of 1.32–2.36 eV [83]. The high carrier mobility indicates that Janus TMDs are suitable for use in electronic devices, such as field-effect transistors. The monolayers of the group-VI chalcogenides, WSSe, MoSSe, and MoSeTe are direct bandgap semiconductors, with the conduction band minimum (CBM) and valence band maximum (VBM) located at the K point in the first Brillouin zone. Other variants of this class, namely, MoSTe and WSTe monolayers, have an indirect bandgap with the CBM located at the in-between K -Γ points and VBM located at the Γ point, respectively. Additionally, considering the spin-orbit coupling, the band structures of the Janus MXY monolayers show stable spin splitting at the band edges around the K point, just like their parent TMD structure. Thus, showing potential for applications in spintronic devices.

1.5.1. The Bychkov-Rashba effect

A momentum dependent splitting of spin bands, the Rashba effect is quite analogous to the splitting of the particles and anti-particles in the Dirac Hamiltonian [103] The splitting of the band is a combined effect of the spin-orbit interaction and the asymmetry of electric field potential within the crystal [104].

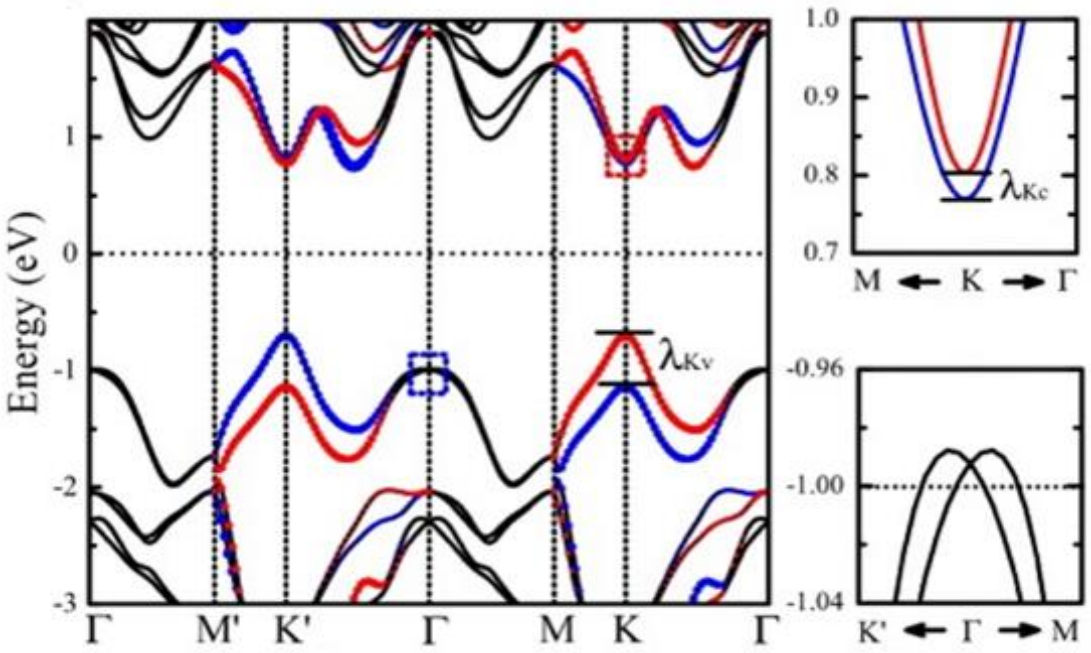

Figure 1.11 Electronic band structure of WSSe without with SOC, Where Rashba Splitting can be observed at the VBM

Panel adapted with permission from ref [105] Royal Society of Chemistry

Applications of this effect include the ability to control electron spins by electric fields and Anisotropic Magnetoresistance[106-108]. Over the years, researchers have carried out many studies in order to realize the Rashba effect within a variety of classes of materials, including bulk crystals as well low dimensional systems such as heterostructures and surface states.

The observance of Rashba splitting was confirmed in 2012 in bulk BiTeI as a potential candidate for spin-dependent electronic devices[109]. 2D $LaOBiS_2$, with a thickness of 1 nm, also shows large Rashba splitting of the bands. Due to the absence of mirror symmetry, materials with a large Rashba spin splitting and seem to be another promising candidate for spintronic applications[110]. The asymmetric electric field coupled with the spin-orbit coupling within Janus TMDs fulfill both the requirements to observe Rashba splitting within a material and after the synthesis of Janus MoSSe, researchers soon began to investigate electronic band structures of a series of Janus monolayer TMDs with chemical formula MXY. A Rashba-type spin splitting around the gamma point has been predicted for all the MXY systems based on first-principle calculations alone[111].

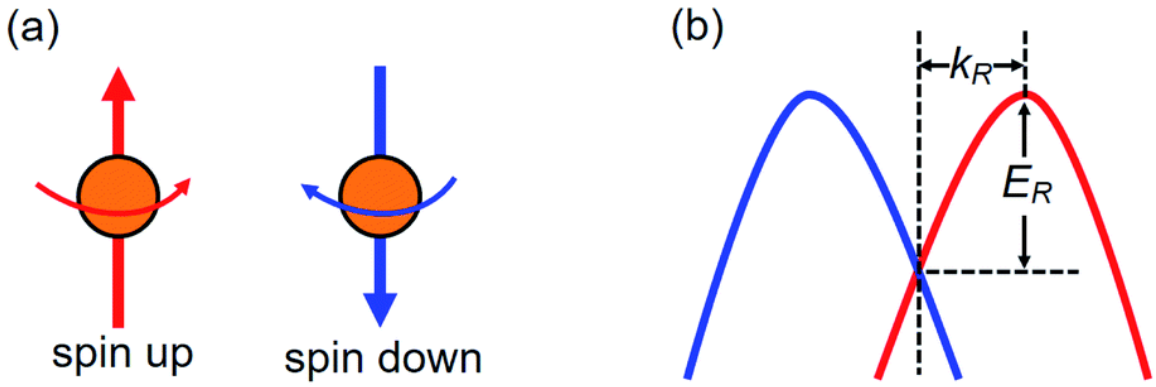

Figure 1.12 (a) Spin-up (red arrow) and down (blue arrow) chiral states. (b) A magnified schematic illustration of the Rashba spin splitting with Rashba energy E_R and momentum offset k_R

Panel Adapted with permission from ref [111] Royal Society of Chemistry

Additionally, group V based Janus TMDs Such as NbSSe have been predicted to show Ising superconductivity, in such materials, Rashba splitting might aid in the possible

realization of the Majorana fermions, Larkin–Ovchinnikov–Fulde–Ferrell phase and topological p-wave superconductors [111-113]. The spin splitting effect has been studied most extensively for MoSSe and WSSe Janus materials and their heterostructures, whereby Rashba spin splitting is shown to exist with the valley spin splitting. Compared with traditional TMDs such as MoS_2, the inversion asymmetry introduces spin-momentum locking, and the energy dispersion shows the two parabolas in k space are shifted by a momentum offset. This, however, can only be observed when a surface state or an external out-of-plane field is present in the crystal.

Synthesis and creation Janus MoSSe from MoS_2, allows us to break mirror symmetry through chalcogen alternation manually and introduces an intrinsic out-of-plane polarization field within the structure. This polarization has been shown to stabilize spin-nondegenerate states at the Γ point and thus induce a significant Rashba effect. Theoretical predictions have shown that the Rashba parameters for Janus materials can be much larger than current champion materials of this effect, e.g., STO and BiTeI [105, 114, 115]. The spin splitting can be enhanced by an external electric field collinear with the local electric field derived by the polar bonds and by the compressive strain. Interestingly, The Rashba parameters can be tuned to change linearly with an external electric field, or nonlinearly with the biaxial strain for MXY based Janus MoSSe. The anisotropic Rashba spin splitting was also found to be enhanced significantly by the introduction of a compressive strain within this class of material [115, 116]. A similar study on another MXY based Janus, WSSE showed that the Tungsten and Sulfur atoms contribute more than Selenium atoms in the valence- band maximum at the Γ point.

The Rashba effect can also be significantly affected by interlayer interaction between atoms, and a layer-dependent Rashba splitting can exist in asymmetry-ordered WSSe bilayers, that can be tuned by changing the interlayer distance [117]. While the results are still in their infancy, tuning the Rashba parameters offer opportunities that are particularly interesting for spintronics and quantum device applications.

1.5.2. Magnetism and Skyrmionics.

Two-dimensional ferromagnetism is critical in technological development and device modulation due to the quantization of electronic states. However, due to limited materials that show high-temperature 2D ferromagnetism, phenomenon such as anomalous quantum hall effect (AQHE) and thin-film spintronics remain elusive[118].

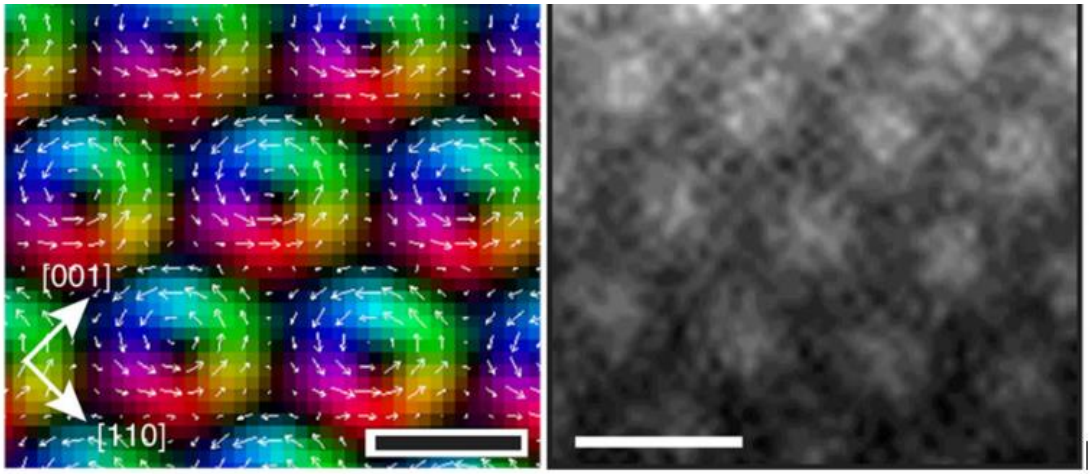

Figure 1.13 (left)in-plane magnetization textures of the skyrmion crystal deduced from TOI analysis (right) The under-focus Lorentz TEM image for the skyrmion crystal taken at 250 K and 150 mT

Panel Adapted with permission with from ref [119] Springer Nature

Furthermore, the isotropic Heisenberg model with finite-range exchange interactions contradicts the ferromagnetism in low dimensional materials. One can explain

this based on the Mermin-Wagner theorem, which states that long-range order in low dimensional materials with continuous symmetry at finite temperatures is severely limited by short-range isotropic interactions[120]. Theoretically, it can be shown that a two-dimensional isotropic Heisenberg model does not have a ferromagnetic solution[121, 122] Recent signs of progress have shown that CrI_3 and bilayer $CrGeTe_3$ at low temperature show that magnetic ordering can be stabilized in 2D systems, which dramatically broadens electronic applications of van der Waals materials [105, 123, 124]. Encapsulated CrI3 flakes present layer-dependent ferromagnetic phase transition from ferromagnetism in the monolayer limit, to antiferromagnetism in the bilayer, and ferromagnetism in the trilayer and bulk. Other 2D systems, such as VSe_2[125, 126], $MnSe_2$[126], and Fe3GeTe2[127, 128], have also shown near room temperature ferromagnetism down to the monolayer limit. However, many issues remain in the material preparation of 2D ferromagnets, examples of which include controllable synthesis with high speed of growth, massive area realization, and the stability under ambient atmosphere. The most commonly used method for preparing 2D ferromagnetic materials is mainly via mechanical exfoliation of CVT grown bulk crystal, that yield a quasi 2D crystal with bulkier regions, Mechanical exfoliation is also unsuitable for large scale synthesis.

With recent progress in 2D Janus layer synthesis, one can easily overcome these disadvantages. Furthermore, since the ferromagnetism in two-dimensional materials is mostly dependent on the anisotropy of the material, the Janus layers allow this quantum phenomenon naturally by breaking the mirror symmetry. Current theoretical articles on

Janus VSSe and CrIBr layers have shown that the intrinsic polarization enables high Curie temperature (T_c) ferromagnetism in these materials [129, 130].

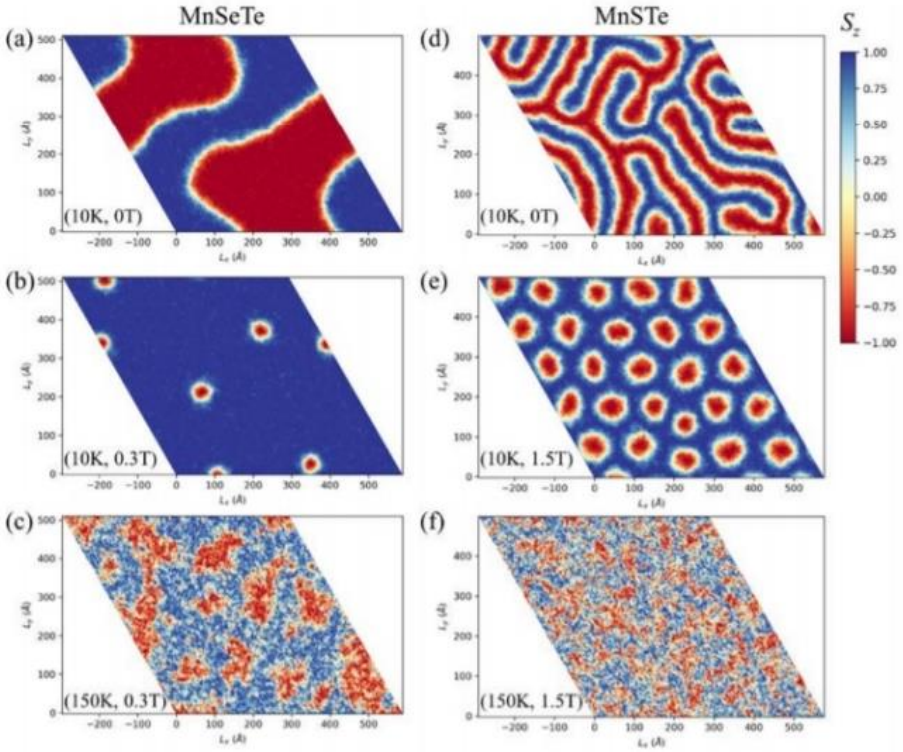

Figure 1.14 Spin textures for (a)-(c) MnSeTe and (d)-(f) MnSTe monolayers in real space

Panel adapted with permission from ref [131], preprint arXiv:1906.00648

One effect of the polarization field is the immediate change in the Dzyaloshinskii-Moriya interaction (DMI) strength. DFT calculations have shown that DMI interaction changes in Janus MnSeTe and MnSTe [131, 132]. This effect can potentially stabilize topologically protected skyrmion without the need of an external magnetic field and opens another pathway for quantum spin manipulation. Due to the out-of-plane geometric

asymmetry and strong spin-orbit coupling, monolayer MnSTe and MnSeTe can stabilize such intrinsic skyrmions, while monolayer VSeTe forms magnetic domains.

Realization of the moiré skyrmions in 2D Magnets originating from the moiré pattern vdW heterostructures can also be achieved by combining a ferromagnetic monolayer such as VSeTe, MnSeTe or MnSTe with antiferromagnetic substrate MnPX3 (X=Se, Te, Se)[133-135]. Due to the intense interlayer coupling situation between the layers, Skyrmion vorticity and location in the moiré can be switched by a magnetic field. Additionally, in the case of weak interlayer coupling, the metastable skyrmion excitations can be moved between the ordered moiré trapping sites by applying a current pulse [134]. These applications make two dimensional Janus magnets an up-and-coming candidate for quantum spin applications. Since most of these studies are mainly based on density functional theory and Bohr magneton per unit cell arguments, fundamental understanding of how the magnetic order in two dimensional Janus materials change under extreme polarization field remains unknown and thorough research is required in order to understand the underlying mechanisms

1.5.3. Excitonic and Spin-valley interactions.

Large spin-orbit coupling (SOC), when combined with the lack of inversion symmetry in two-dimensional TMDs, allows to individually control valleys in K-space at the K and K’ points in the first Brillouin zone[136]. As a result of the unique combination of spin and valley degrees of freedom, optically generated electrons and holes are both

valleys- and spin-polarized (spin-valley locking), a quantum property that is absent in other traditional semiconductors.

In Janus TMDs, excitonic behavior is observed due to the broken mirror symmetry and the presence of a permanent dipole offers. The homojunction of these layers can form type-II junctions with band offsets comparable to the potential difference between the top and the bottom faces of the Janus sheets[137]. Interestingly the valleytronic responses can be significantly tuned, depending on the stacking order, and large Berry curvature values are also (~100 Bohr2)[138]. Such properties open ways to achieve lossless valley polarization without a need for EM field, or electronic doping/gating[116, 139, 140]. Thus, Janus materials new ways to tune the spin polarization ratio without the use of any external electric or magnetic fields.

1.5.4. Piezoelectric response:

Many materials, such as crystals and certain ceramics, will accumulate a certain amount of charge in response to applied mechanical stress. This effect is called piezoelectricity and arises due to a linear electromechanical interaction in insulating crystalline materials without inversion symmetry. Piezoelectric materials are of tremendous importance and have had a wide variety of applications in devices, sensors, actuators in the past century.

Within two-dimensional materials, Piezoelectricity has been obtained in a series of substances, including h-BN and MX2 layers, with the in-plane inversion asymmetry and insulating properties being the standard feature. As mentioned before, due to the absence

of mirror symmetry, a large in-plane and out of plane piezoelectric effect can be realized in the monolayers Janus 2D TMDs. Janus structures exhibiting piezoelectric properties starting from the group-III monochalcogenide are predicted to be thermodynamically stable[141]. Ga2STe, Ga2SeTe, In2STe, and In2SeTe monolayers are shown to be direct gap semiconductors materials with a bandgap in between 0.89–2.03 eV. The piezoelectric coefficients for these materials are up to 8.47 pm/V, and this value is reported to be over four times the maximum value obtained in perfect group-III monochalcogenide TMD monolayers [83]. The broken mirror symmetry in these Janus structures also induces an out-of-plane dipolar polarization, yielding out-of-plane piezoelectric coefficients of 0.07–0.46 pm/V [83].

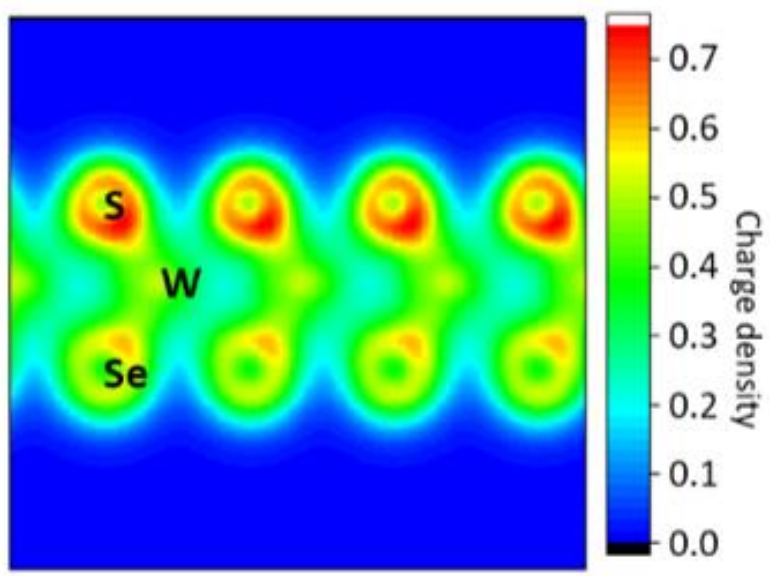

Figure 1.15 Atomic view and calculated charge distribution for 2D Janus TMDs

Janus MXY monolayers have both in-plane and out-of-plane piezoelectric response under a uniaxial strain. The smaller the radius of the transition metal elements, the higher there the values of the piezoelectric coefficients. This therefore shows, the

MoSeTe and MoSTe monolayers have the highest in-plane piezoelectric response amongst all the Janus MXY monolayers.

Piezoelectricity in 2D van der Waals materials has received considerable interest because of potential applications in nanoscale energy harvesting, sensors, and actuators. For MXY monolayers, both strong in-plane and much weaker out-of-plane piezoelectric polarization can be induced by a uniaxial strain in the basal plane. In multilayer MXY, a very strong out-of-plane piezoelectric polarization was obtained. The out-of-plane piezoelectric coefficient was found to be strongest in multilayer MoSTe.

1.5.5. Photocatalysis:

The limitations for the current three-dimensional photocatalyst arises mostly from their inefficiency to utilize the full spectrum of the sunlight, hence limiting the solar to hydrogen conversion efficiency. Another disadvantage for the three-dimensional systems is the high rate of electron-hole. Recently, interest in the production of hydrogen using two-dimensional semiconductor-based photocatalysts has received widespread attention. The large surface area, abundant surface states, and tunable electronic property make two-dimensional materials an attractive candidate for such an application. Strong excitonic effects within traditional TMDs has led to faster recombination and have limited their use in this area, Janus TMDs However shows a promise. Recent studies in the functionalization of Janus TMDs, namely MoSSe nanotubes, have been predicted to be one of the forerunners for photocatalytic application. Janus nanotubes have shown to be a direct bandgap with 1.44 even, this is only too suitable for band edge positions and pronounced

light absorption within the visible spectral range [142, 143]. Janus MXenes have also theoretically been predicted to show much promise for photocatalysis [144].

1.6. Janus Experimental Review

The first experimental realization of these Group VI- Janus based materials were realized in the independently by two groups at Rice and Columbia [145, 146]. Although the ability to synthesize other Janus material based on the same method should have been straight forward, studies have been limited to date, and no other experimental evidence has been published. This is mainly due to the challenges in 2D Janus synthesis, sample preparation, and material quality. The prime difficulty presented in the synthesis of these Janus materials is that they are thermodynamically unstable in their bulk form, except for the BiTeI family. While the creation of thermodynamically stable 2D alloys is more natural to Janus layers, unlike their alloy counterparts, it must be produced at unit cell level with atomic precision.

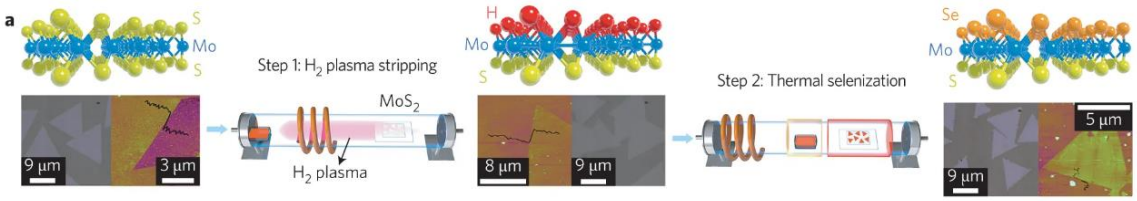

Figure 1.16 Synthesized Janus MoSSe by the plasma-assisted surface decoration of CVD grown MoS_2

Panel adapted with permission from ref [146], Springer Nature

Another reason that experimental studies have been much limited for these materials is perhaps due to inadequate understanding of their reaction kinetics and

thermodynamic stability. Of the two experimental results, the first relied on the selenisation of monolayer thin films. In this study, Lu et al. synthesized Janus MoSSe by the surface decoration of CVD grown MoS_2 via an in-situ Selenization process.

This process relied on the stripping of the top layer of the MoS_2 monolayer under the influence of ionized hydrogen plasma that was generated via an inductively coupled plasma setup. After the stripping process, the second step of thermal Selenization is undertaken by which the recently stripped off top layer is replaced by thermally activated selenium ions. The entire process was carried out at a lower pressure within a vacuum tube to avoid oxidation. The process was especially important in establishing the synthesis of Janus MoSSe from MoS_2 and relied on thermodynamically driven reaction engineering.

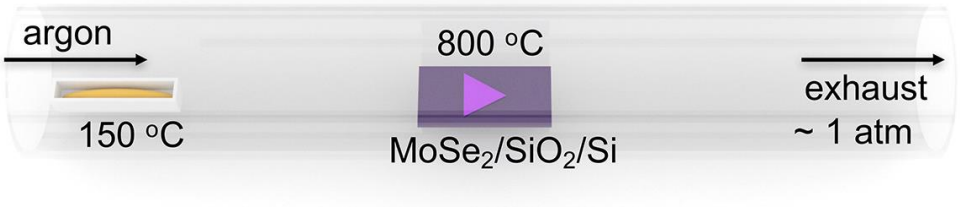

Figure 1.17 Thermal sulfurization of $MoSe_2$ monolayers

Panel adapted with permission from ref [145] American Chemical Society

In the same year, Zhang et al. also synthesized Janus MoSSe via an in-situ sulfurization process of chemically vapor deposited molybdenum selenide monolayers. Their approach vastly differs from the first group, Starting with $MoSe_2$ instead of MoS_2, the synthesis is entirely thermodynamically driven and carried out at very high temperatures. The top layer of $MoSe_2$ monolayer is sulfurized within a tube at 800°C temperatures at 1 atm pressures. Both studies characterized and confirmed the existence of these materials by Raman Spectroscopy, XPS, and STEM, with their results in agreement

with the established theoretical literature. Even though the Raman and PL spectra matches to those predicted from theory, it remains unclear how alloying can be prevented at such high temperatures. In these two studies, the presence of Janus layers was confirmed mainly by comparing the calculated phonon dispersion relation with the measured Raman spectrum, and room temperature PL spectra were also provided to show light emission from these layers. More importantly, it appears that reproducing these remains significantly challenging, as evidenced by no experimental verification since 2017. This suggests that the growth mechanism is highly complex, and possibly it depends on a variety of growth parameters including flow rate, sample positioning, temperature window, plasma power, initial material quality, and many other parameters related to the kinetics of the reaction.

2. Chapter 2 Synthesis And Characterization

2.1. Top-Down Approach

While there exists a variety of top-down approaches that could be incorporated for synthesizing bulk crystals, chemical vapor transport (CVT) remains one of the most reliable, economic, and simplified approaches. In the context of this work, all exfoliated monolayer samples were obtained from the bulk crystal that was grown via. Chemical Vapor Transport.

2.1.1. Chemical Vapor Transport of bulk Crystal

Chemical Vapor Transport (CVT) is a technique for growing high-quality bulk crystals. CVT growth is a thermally driven chemical reaction that relies on the stoichiometry and thermodynamics of the system. In general, a reactive precursor in the solid phase is sublimed and transported with the help of a transport agent in a sealed quartz ampule. The reaction takes place at a higher temperature, and the formation of the bulk crystal is usually observed in the cold zone of the quartz ampule. Since the technique relies heavily on the thermodynamic, transport phenomena, and kinetics of the reactants involved, the rate of precursor diffusion and thermal convection is incredibly crucial for synthesizing high-quality crystals. Other key factors that influence the growth include but are not limited to, reaction temperature gradient, the stoichiometry of the precursors involved, catalysts, and use of transport agent. A transport agent also plays a vital role in the growth mechanism where the reaction rate is limited by surface diffusion. In general, Group 17 elements such as bromine and Iodine are often used as transport agents

Since the phase diagrams and thermodynamic stability data for a wide variety of compounds and alloys already exist, Chemical Vapor Transport growth can be used to synthesize a wide variety of two-dimensional materials very efficiently. However, bulk synthesis of Janus structure with a perfect ratio where all the atomic layers are unique is severely limited by current technology and CVT growth techniques, Since CVT growth is carried out at a high temperature, the atoms are thermally excited, and it is near impossible to control the growth of individual atom on individual planes. Preferably, at such temperatures and growth conditions, chances of creating a randomized structure of two different phases are more favorable energetically.

This drawback can be mitigated by exfoliation of bulk crystals into monolayers and then changing their structure at an atomic level since TMD bulk crystal are already layers and can be easily exfoliated by a variety of methods, Exfoliation can be of bulk crystal to followed by Janus processing is a very lucrative approach. The drawbacks, in this case, is the minimal yield from the exfoliation process. Exfoliation will also yield quasi-two-dimensional structures that may interfere with Janus post-processing, such as thermal selenisation at high temperatures. For instance, exfoliation of bulk crystal usually always leaves bulk and few layers region surrounding the monolayer, in addition to this, depending on the exfoliation technique one might expect contamination from tape residue or likewise Lastly exfoliation of single monolayer from bulk crystals is dimension limited and large monolayer sheets are unobtainable. Hence although CVT growth followed by exfoliation sounds very appealing at a lab-scale, the technique is severely limited at industrial or pilot scale levels.

2.2. Mechanical Exfoliation

Two-dimensional materials such as transition metal dichalcogenides have been identified and drawn much attention over the last few years due to their ability to be successfully isolated from their layered assemblies into individual monolayers. Exfoliation and transfer remain one of the most accessible and successful techniques to obtain high-quality single or few-layer nanocrystals from their native multi-layer structures. In the scope of this thesis, mechanical exfoliation of bulk crystals such as Molybdenum Selenide and Niobium selenide was undertaken in order to obtain their monolayer equivalent.

2.3. Bottom-Up Approach

The bottom-up approach refers to synthesis methods such as Physical Vapor Deposition (PVD), Plasma Enhanced-Chemical Vapor Deposition (PE-CVD), Metal-Organic Chemical Vapor Deposition (MOCVD) and Atmospheric Pressure – Chemical Vapor Deposition (AP-CVD). These methods are a family of vapor deposition techniques in which atomically thin monolayers and few-layer thick films are fabricated via self-assembly of vaporized reactants on a substrate. In this work, Atmospheric Pressure Chemical Vapor Deposition was used to synthesize all types of CVD grown monolayers.

2.3.1. Chemical Vapor Deposition

A CVD system, besides, temperature control (Like CVT), is also equipped with a pressure and mass flow controller. The setup consists of a single or two-zone furnace inn which a quartz tube is supported. The tube is connected on both ends to a gas line through which a carrier gas is continuously passed. Depending on the type of synthesis, the carrier

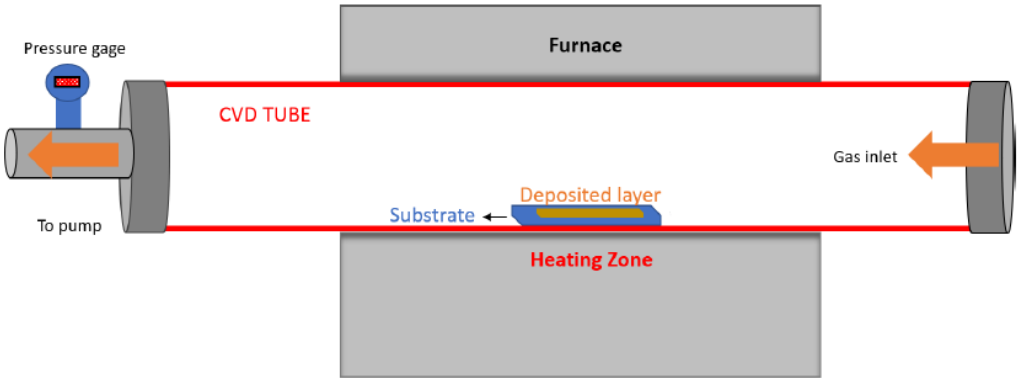

Figure 2.1 Schematic of a simple CVD steup

gas may also act as a reducing agent in addition to be a transport agent for the reaction precursors. The growth process is more kinetically driven, unlike CVT, which only relies on the thermodynamics of the precursors.

Chemical Vapor Deposition can be used for deposition or coating of any chosen material layered material, although, synthesis of group IV and group V is very underdeveloped. In most CVD setups, sublimed precursors are flown over the desired substrate such as Si/SiO_2 or AL_2O_3 inside the reaction tube using an inert carrier gas such as Ar or N_2. The chemical reaction occurs on the surface of the substrate that is placed in a hot zone. This results in a deposition of thin-film / monolayer over the substrate. This process is also accompanied by

byproducts that are purged out of the reaction chamber by using a pump. Since most of the CVD growth involves toxic precursors, a proper reduction system is required in order to render the purge line safe for atmospheric release. A typical CVD schematic is displayed in the figure. As mentioned before, CVD can be performed at varying pressure levels, ranging from millitorr to atmospheric pressure, which can be controlled by a capacitance manometer connected to the downstream side of the chamber.

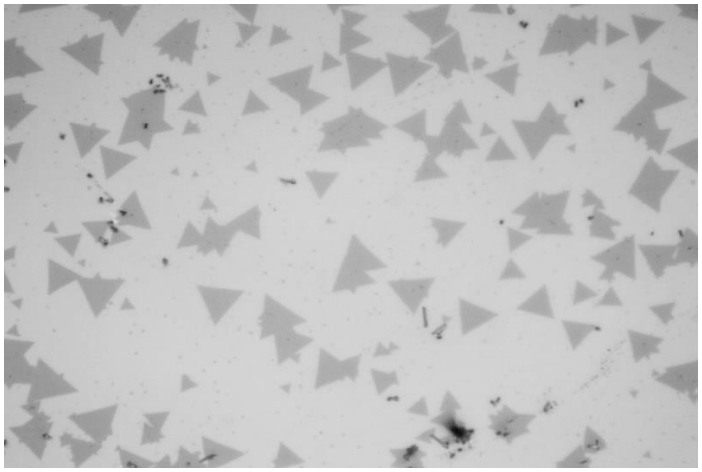

Figure 2.2 Monolayer domains of CVD grown TMDS observed on an optical microscope

Compared with chemical vapor transport, CVD is somewhat more complicated, and successful growth relies on a wider variety of parameters other than temperature alone. These include nut are not limited to, the stoichiometry of the reactive precursors, flowrate of the process gas, rate of cooling, wettability of the substrate and effects of fluid flow along with the boundary layer of the substrate. Another crucial aspect of CVD is sample preparation, which will affect the growth quality and crystallinity of these films. Adequate sample preparation can make the substrate more favorable for nucleation, which eventually

grows into a more massive lateral size film over the substrate. The wettability of the substrate surface is often increased by removing any oxide layer deposited on the surface; additionally, the use of nucleating agents such as perylene might be employed for promoting growth. Sapphire or SiO_2/Si substrates are generally favored because of their high surface energy

2.3.2. AP-CVD Synthesis of Molybdenum Based TMDs

The synthesis of monolayer $MoSe_2$ was achieved via the ambient pressure chemical vapor deposition (AP-CVD) method previously reported in the literature. Initially, 285 nm substrates of Si/SiO2 are cut in a 16 X 6 mm area under a dicing saw. This is to ensure that all the substrates used for the synthesis are of the same dimensions and will not introduce any form of local fluid flow effect. The substrates are then cleaned and sonicated in absolute ethanol followed by isopropanol, after which they are dried with nitrogen. The substrates are then treated with Argon plasma for 15mins to remove any residual impurities. A single cleaned Si/SiO2 substrate is then treated with one drop of 50 μ-molar Perylene-3,4,9,10-tetracarboxylic acid tetra potassium salt solution (PTAS) as a nucleating agent. In a ceramic boat, About 1 mg of MoO_3 precursor (Sigma-Aldrich, ≥99.5% purity) mixed with NaCl was placed inside a clean one-inch diameter quartz tube supported on a Lindberg/Blue M Tube furnace. The position of the boat is at the center concerning the furnace. Before loading the boat inside the tube, SiO_2/Si substrates, the polished side facing downwards, were placed on the ceramic boat. Selenium precursor was placed upstream in a ceramic crucible in excess, where the temperature was maintained at 300 $^{\circ}$C. High purity Ar (≥99.99%) is initially passed to purge the chamber of any contaminant gases, after

which 46 sccm flow of argon is maintained till the furnace reaches the reaction temp. After this, high purity H_2 gas is introduced into the system at four sccm during the growth time.H_2 acts as a reducing agent for Selenium-based growths, and it is crucial to $MoSe_2$ growth.

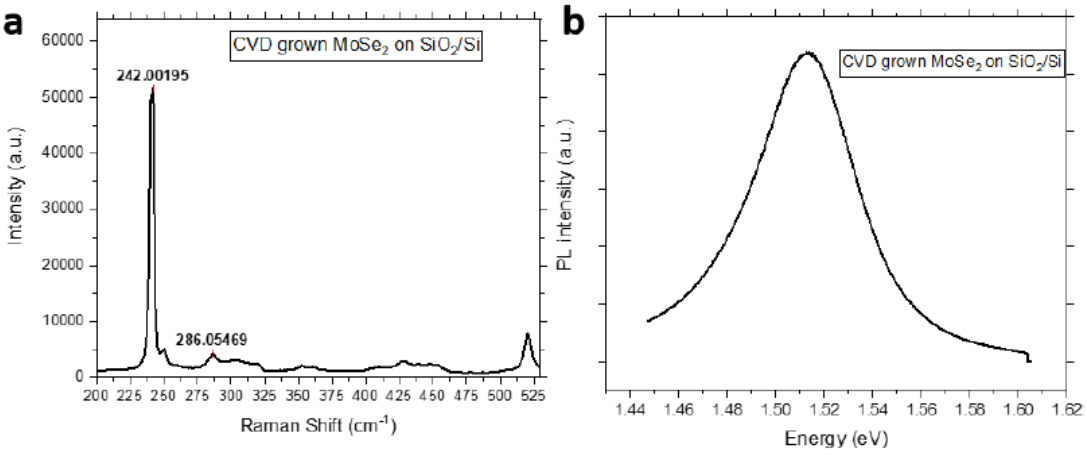

Figure 2.3 (a) Raman Spectra of CVD grown $MoSe_2$ (b) PL Spectra of CVD grown $MoSe_2$

The furnace was ramped up with a rate of 30 ˚C/min to 790 ˚C and held at 790 ˚C for a growth time five minutes before natural cooling to room temperature; The H_2 is cut off after the growth and 200 sccm Ar is introduced into the system for rapid cooling. The as-grown $MoSe_2$ is then characterized using Raman and PL spectroscopy. The height of the sample is also verified using AFM to confirm the monolayer nature of the sample. Synthesis of molybdenum sulfide is also carried out similarly. Since the synthesis of MoS_2 does not require a reducing environment, only Argon is used as a carrier gas. Briefly, The synthesis of monolayer/bilayer MoS_2 was achieved via the AP-CVD method via the following recipe. 3 mg of MoO_3 precursor mixed with NaCl in 50:1 ratio was placed in a ceramic boat at the center of the single-zone tube furnace. 285 nm SiO_2/Si substrates were

placed polished side down on the ceramic boat. Sulfur was placed upstream in a ceramic crucible in excess, where the temperature was maintained at 200 °C. High purity Ar was passed at 20 sccm during the entire growth process. The furnace was ramped up with a rate of 30 °C/min to 700 °C and held for 13 min before naturally cooling to room temperature

2.3.3. AP CVD Synthesis of Tungsten Based TMDs

The synthesis of monolayer WSe_2 was achieved via the AP-CVD method. 60 mg of WO_3 precursor was placed in a ceramic boat at the center of the single-zone tube furnace. Double side polished sapphire substrates were placed on the ceramic boat. Selenium powder was placed upstream in a ceramic crucible in excess, where the temperature was maintained at 250 $^{\circ}$C. High purity Ar (≥99.99%) and H_2 gas were passed at 36 sccm and four sccm flow rates, respectively, during the entire growth process. The furnace was ramped up with a rate of 30 $^{\circ}$C/min to 850 $^{\circ}$C and held at 850 $^{\circ}$C for 20 minutes before natural cooling to room temperature.

The synthesis of monolayer WS_2 was achieved via the AP-CVD method. 50 mg of WO_3 precursor was placed in a ceramic boat at the center of the single-zone tube furnace. Double side polished sapphire substrates were placed on the ceramic boat. The sulfur powder was placed upstream in a ceramic crucible in excess, where the temperature was maintained at 250 $^{\circ}$C. High purity Ar (≥99.99%) and H_2 gas were passed at 50 sccm and 1.5 sccm flow rates, respectively, during the entire growth process. The furnace was ramped up with a rate of 15 $^{\circ}$C/min to 870 $^{\circ}$C and gradually cooled to 760 $^{\circ}$C in 40 minutes before natural cooling to room temperature.

2.4. Raman Spectroscopy

Raman spectroscopy is a nondestructive spectroscopic technique that has been used to analyze and fingerprint vibrational, rotational, and low-frequency modes of materials. The technique is highly versatile and is also used to analyze the defect concentration, crystallinity, and strain-induced effects in a material at the microscopic level. The most common Raman setups consist of a microscope, an excitation source in the form of a laser, a CCD detector, and an edge filter.

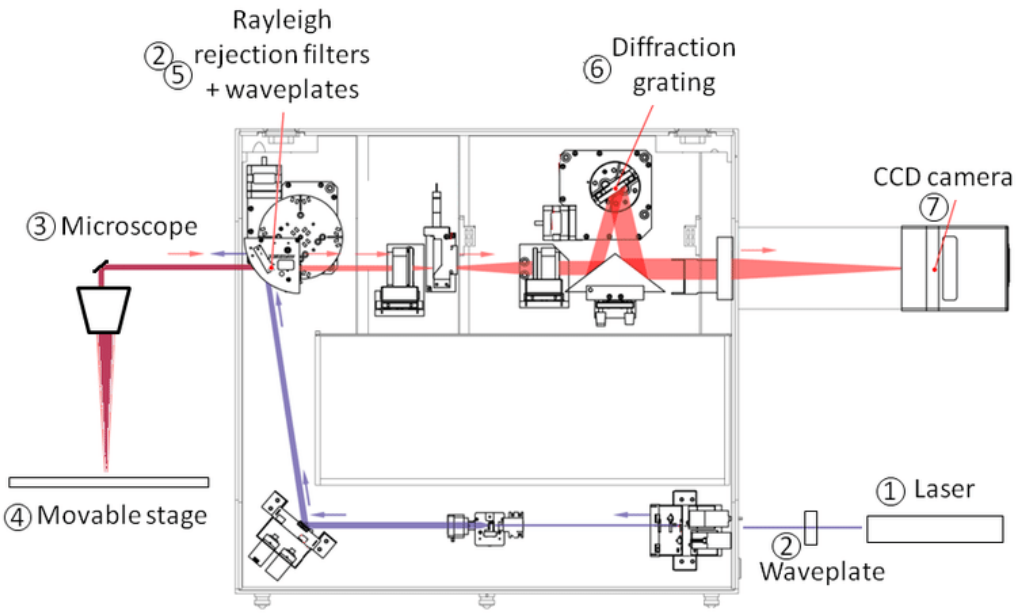

Figure 2.4 Schematic of simple Raman setup © Renishaw

The optical microscope within the setup allows for quick characterization of thin films and even monolayers (~1 nm thickness) due to the subtle optical contrast these materials will create on the substrate. While the technique is highly versatile to broad classes of materials, it is strictly limited to the analysis of only crystalline structures.

The figure indicates a typical Raman spectrometer, laser pinhole at the bottom right corner acts as a light excitation source from where an incoming monochromatic laser enters the system. Mirrors and filters direct the laser onto the sample through a microscope objective. The laser then interacts with the material and undergoes inelastic scattering by the phonons within the material, a phenomenon known as the Raman effect. The inelastically scattered light travels back the same optical path and is detected with the help of a photodetector (spectrometer). In contrast, Rayleigh or elastically scattered light is filtered out with the Rayleigh rejection filters.

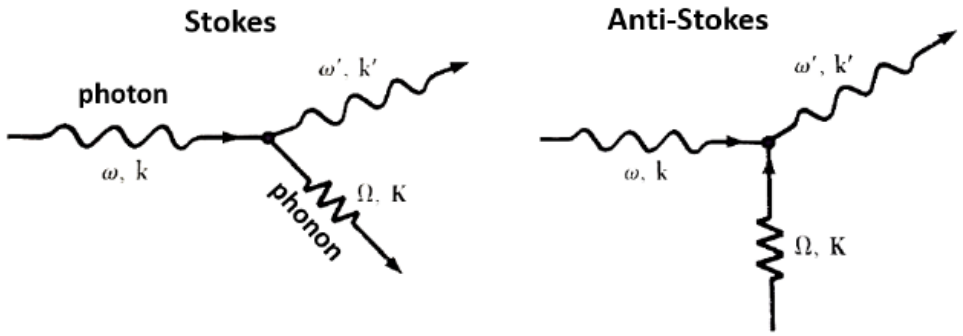

Figure 2.5 Processes indicating Stokes (left) and Anti-stokes (right)

The non-elastically scattered light comprises of stokes and anti-stokes scattered rays depending upon the type of interaction of a photon with the phonons within the sample. At room temperature, the probability of getting a Stokes shift is much higher than an anti-Stokes shift. The lower probability is attributed to the extra amount of energy required by the phonons for an anti-stokes process. The stokes and anti-stokes processes are detected by a spectrometer, which causes the emergence of peaks on the screen concerning a specific

wavenumber (frequency), thus indicating a mode of vibration from the material's symmetry, which can then be compared to either fingerprint signals or from a theoretical phonon dispersion curve.

Since most of the backscattered light is filtered out as Raleigh scattering and only a tiny majority of Stokes and the anti-stokes signal is collected in every measurement. An intensified CCDs is often required to enhance the signal to noise ratio coming from the sample without an extended period of exposure to a high-power laser.

Overexposure from the laser could cause surface modification and thus resulting in poor on improper data collection. Sensitive sample measurement must be performed at low laser powers to avoid sample degradation. Signal to noise ratio in such cases can be improved by increasing the number of accumulations that are acquired in a single measurement.

2.5. Photoluminescence Spectroscopy

Photoluminescence is another contactless nondestructive spectroscopic technique that is used to probe the electronic structure of the material. The spectroscopy is based on the photoexcitation principle and is usually performed with the same instrumentation used for Raman spectroscopy. The photoexcitation principle is based on the creation of electron-hole pairs due to incident radiation of a specified wavelength (or energy of the photon). If the minimum energy of photon irradiated on the sample is greater than or equal to the bandgap of that material, the incident radiation will cause the electron in the material to move into an excited state from the valence band (VB) to conduction band (CB). When

the system reaches an equilibrium, the excess energy is released and may include the emission of light (a radiative process) or may not (a non-radiative process).In a radiated process, the energy of the emitted light is called photoluminescence and relates to the difference in energy levels between the two-electron states involved in the transition between the excited state and the equilibrium state.

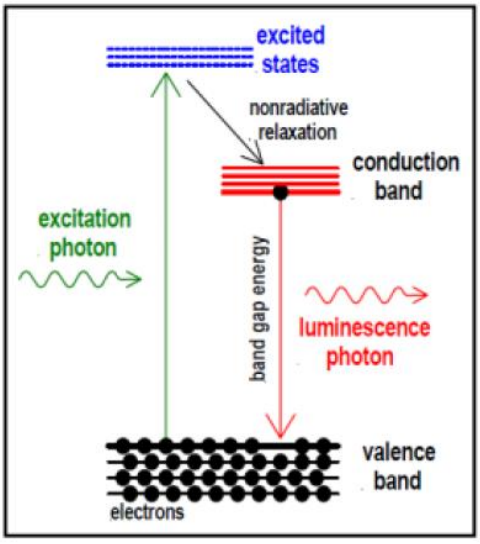

Figure 2.6 Basic principle of photoluminescence spectroscopy ©Renishaw

Thus, the process is exceptionally crucial in the determination of band gaps in electronic materials, analysis for recombination mechanisms, and study of surface structure and excited states. At room temperature, the energy of the photon emitted is either less than the bandgap or equal to the bandgap. This emitted photon is collected by a detector, and the energy of a photon can be observed on the screen. In the case of a direct bandgap material, one can easily extract out the optical bandgap of the material based on the plot of PL intensity vs. energy, where energy value for a peak suggests the optical bandgap. The

Full Width at Half Max (FWHM) of the peak can help determine the optical quality of the material or identify a relative concentration of defects into a material.

The PL spectrum at low sample temperatures often reveals spectral peaks associated with impurities contained within the host material. Fourier transform photoluminescence microspectroscopy, which is of high sensitivity, provides the potential to identify deficient concentrations of intentional and unintentional impurities that can strongly affect the material quality and device performance. At lower temperatures, the measurements performed on the sample follow Varshini's law and, the photoluminescence peak energy blue shifts [147]. The change in the relative position of the valence and conduction band due to temperature-dependent dilation of the lattice affects the electron lattice interaction, thus decreasing the bandgap of a material at low temperature. Varshini's law is expressed using the empirical expressions given as follows:[147]

$$E_g = E_0 - \frac{\alpha T^2}{(T+\beta)} \quad (1)$$

Where α and β are material constants, E_0 is bandgap at 0K, and E_g is bandgap at arbitrary temperature. Since Radiative transitions in semiconductors involve localized defect levels, the photoluminescence energy associated with these levels can also be used to identify specific defects. Furthermore, the amount of photoluminescence can be used to determine their concentration.

Non-radiative recombination process is assisted by phonons and which produce heat into the material rather than giving photoluminescence. This type of recombination is prominent in the case of indirect bandgap materials because excitation and recombination

of an electron from VB to CB and vice versa requires help from the phonons to conserve the momentum. The process of characterization by photoluminescence, therefore, is not a practical approach for indirect bandgap materials. In case of direct bandgap materials, however, it provides a means to quantify the elemental composition of compound semiconductors

2.6. Atomic Force Microscopy

Atomic force microscopy is one of the most fundamental characterization techniques in thin films and the semiconductor industry. It is used to measure the topology, work function, and surface roughness in the X and Y direction with a nanoscale resolution. Furthermore, the forces between the tip and the sample can be used to change the local properties of the sample in a precise and controlled manner, for instance, AFM is widely used for atomic manipulation and scanning probe lithography. Characterization techniques such as electron microscopy rely on the interaction of electrons with the material (sample). This usually requires careful sample preparation using FIB, which is often very expensive. Furthermore, electron microscopy is a destructive form of testing, and the sample cannot be reused for other measurements. On the contrary, in AFM, there is direct mechanical contact between the tip and sample, which enables the exact measurement of the sample's surface morphology without the need for extensive sample preparation.

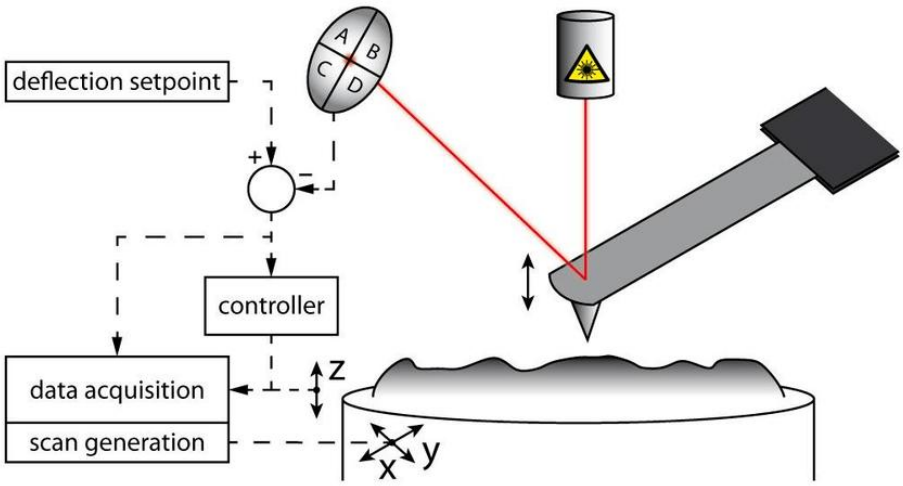

Figure 2.7 Schematic for AFM principle © Bruker

A typical AFM instrument consists of a cantilever (tip) assembly that directly interacts with the sample's surface. These cantilever tips are made of silicon or silicon nitride with a conductive or a non-conductive coating at the tip region used for specified applications. The probe interacts with the sample through a raster scanning motion over the substrate. A laser beam reflected from the top of the cantilever monitors the vertical and lateral motions of the AFM tip as it scans through the surface. The changes in the laser beam are tracked and recorded by a position-sensitive photodetector (PSPD), which then uses this information to create a high-resolution image of the surface. Since AFM is very sensitive to even small dust particles adhering to sample care must be taken to clean the sample of such contaminants.

3. Chapter 3 Selective Epitaxy Atomic Replacement:

3.1. Introduction to Plasma Processing Techniques

Plasma is one of the four fundamental states of matter (and the coolest one, in my opinion). It consists of a gas of ions and free electrons and is extremely conductive. Plasma can be artificially ignited by ionizing the gas molecules in the presence of a strong electromagnetic field. Examples of plasma in the natural world include Earth's ionosphere and the magnetosphere the interior of the Sun is also an example of fully ionized plasma, along with the solar corona and stars. The generation of plasma depends on the ionization energy of the involved gas species [148]; Helium has the highest ionization energy, while Cesium has the lowest of all. Plasma has also utilized for several purposes like spacecraft propulsion in case of ion hall thrusters, sputtering, nuclear-fusion reactors, microfabrication & fab process, and plasma torches for gas reforming of hazardous materials[149]. While several methods exist for the generation of plasma two of the most common ones are briefly mentioned here;

3.1.1. Capacitively Coupled Plasma

Plasma in a capacitively coupled system is generated through two parallel plate capacitors that are separated by a small distance [150]. The power supply is connected to one of the two electrodes, while the other one is typically grounded. The setup is held within a chamber at lower gas pressures, and a voltage drop is created by an RF or DC source across the plates. This generates an electric field between the plates in the direction of the anode to cathode. The gas molecules between these two electric filed are ionized and release electrons. These electrons are then accelerated by the RF field and can ionize the

gas directly or indirectly employing collisions with other gas molecules, thereby ionizing them and producing secondary electrons (impact ionization). This process is usually referred to as electron avalanche and is crucial in the generation of electrically conductive plasma[151]. The avalanche breakdown within a plasma is also accompanied by light emission from the excited atoms or molecules within the carrier gas[152].

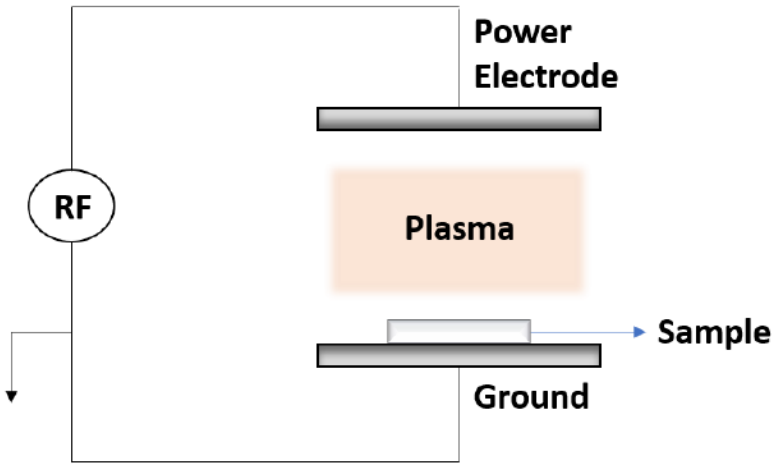

Figure 3.1 Basic schematic for CCP plasma generation

Interestingly, when atoms get ionized, they carry a positive charge and are consequently accelerated inside the field towards the plate, which is being grounded. Because of this property, these energetic ions can be used for etching/removing a material which is kept on the grounded plate by bombardment. The rate of etching can be manipulated by controlling the density and energy of plasma, which depends on several parameters such as pressure inside the chamber, amount of carrier gas available to ionize, choice of gas, applied RF or DC voltage across the plate, etc. [153].

However, despite controlling all the parameters mentioned above optimally, The etching rate of the structure is still dependent on the interaction of the ions with the sample material itself, factors such as binding energy of the atoms in the sample will have a strong influence on the processing time.

3.1.2. Inductively Coupled Plasma

Inductively coupled plasma refers to a plasma generation system in which the energy is supplied by a strong electric current that is sustained through an inductive power coupling [154]. The system is based on Faraday's law of electromagnetic induction for time-varying magnetic fields. This system has many advantages over a capacitively coupled plasma, such as low ion damage and effortless control on plasma density and ion energies[155]. Such features help in controlling the etching rate at sub-nano scales and are very useful in semiconductor display technology. The SEAR process in this thesis is based on inductively coupled plasma.

A typical ICP plasma generation system works by applying RF power on a helical copper coil (tesla coil) that is wound around a cylindrical dielectric chamber. The chamber is held at a lower pressure, and a process gas is flushed within this chamber, acts as the source of ions and free radicals. AC power is supplied to this coil using an RF source. In most commercial systems, the radio frequency is fixed at 13.56 MHz and is applied on the coil with a defined power value [156, 157].

When a time-varying electric current is passed through the coil, it creates a time-varying magnetic field around it, with flux.[158] The magnetic and electrical field ionizes the gas within the chamber resulting in free electrons, which are accelerated under the

influence of the field. These electrons will also interact with the freestanding atoms and molecules, dissociating and ionizing them further. (electron avalanche)

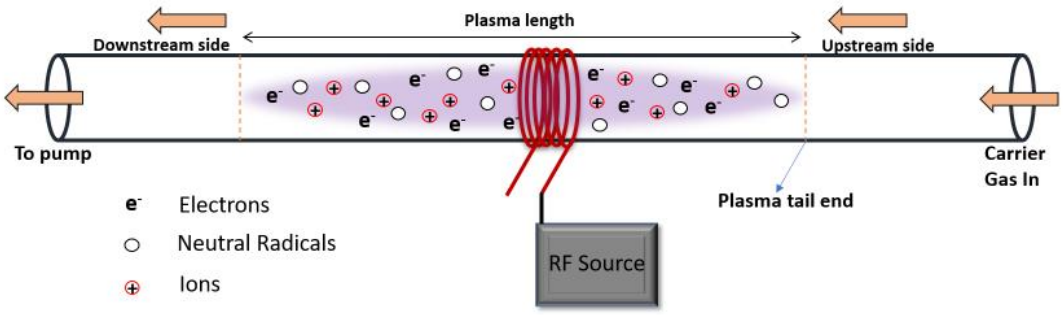

Figure 3.2 Schematic for basic ICP plasma generation

Several critical parameters affect the plasma characteristics and, thus, the overall outcome of the process. Parameters like pressure, gas flow rate, carrier gas type, and power from RF source are some of the most important parameters and are usually manipulated according to the process requirements[159]. Additional parameters such as the number of windings in the helical copper coil, the diameter of the coil, and the diameter of the wire used in the coil construction, tube wall thickness (dielectric) also have an accountable effect on plasma density and the energy of the plasma [160].

For instance, in the scope of our experiments, these initial parameters are established once and held constant. It is assumed that the parameters of coil and tube wall thickness are constant, and the effect of wear and damage over time were ignored. The number of windings in a coil dictates the extent and strength of the magnetic field generated while applying RF. If a fewer number of windings are used, then the intensity of the magnetic field is weaker, and the extent of the magnetic field is much smaller. So, the power needed to generate a plasma in such a case is higher. This will also impart more

kinetic energy to the ionized gas from the start and result in a harsher etching effect. On the other hand, if one uses many windings, then the power needed to generate the plasma is much lower. However, the extent of the magnetic field would create a stable plasma even at meager powers, and the effect of the magnetic field will be seen beyond the length of the visible plasma tail. This magnetic field can cause ionization and dissociation of gas molecules to a very far extent, which may not be observed in the visible spectra. Hence choosing an optimum number of windings that can balance both the effects is exceptionally crucial in the etching process.

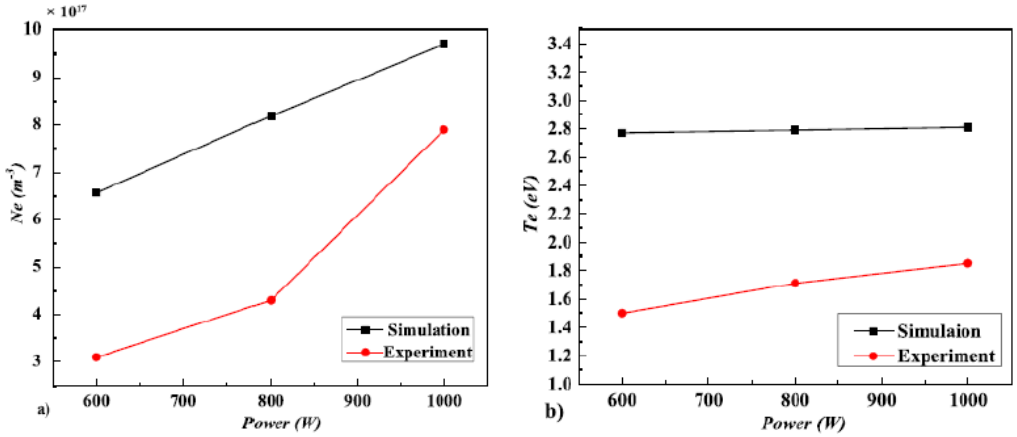

Figure 3.3 Electron density (left) and electron temperature (right) dependence on applied power [158]

In addition to the coil winding, an increase in the power applied also leads to an increase in electron density within the plasma [158, 160, 161]. Higher power also increases the temperature of the overall system due to higher scattering and bombardment. Similarly, the plasma density is also dependent on the pressure inside the chamber. When pressure is increased, the number of gas molecules within the chamber increases, thus increasing the

density of the plasma. There exists an absolute maximum threshold value till which the plasma density increases linearly with pressure[158]. Upon further increase of pressure, the density of plasma starts to decrease because of a higher rate of scattering and atomic interactions taking place. Similarly, when the gas flow rate is increased while keeping other parameters to be constant, the density of the plasma increases till an absolute threshold value is reached, after which the scattering increases and results in a lower plasma density. It is important to note that the selection of carrier gas is the most crucial part of this process because of the atomic size and weight of an atom, it can decide the rate of etching and energy required for ionization of that element.

3.2. SEAR Setup

The synthesis of Janus TMDS has only been achieved by two groups to date. The first method replaced the top selenium layer in $MoSe_2$ in the presence of sulfur vapor (S_2) at a high temperature (800 $^{\circ}$C) to produce Janus MoSSe [146]. In the other method, the sulfur layer was removed using a hydrogen (H_2) plasma, and selenium atoms were decorated on the surface at an elevated temperature (450 ºC) [162]. Both methods are highly specific to Janus MoSSe and require high processing temperatures, which in turn creates difficulties in controlling defect concentrations, achieving high material quality, and fabricating their vertical/lateral heterostructures. Due to the drawbacks in the synthesis methodology for these Janus process, an entirely new synthesis method was developed with an inductively coupled (ICP) setup for making the stripping process gentler. Since the method of ICP plasma follows the principle of generation of plasma-based on the

induced changing magnetic and electrical field generated by an RF source, the strength of this induced field can be tuned by the user.

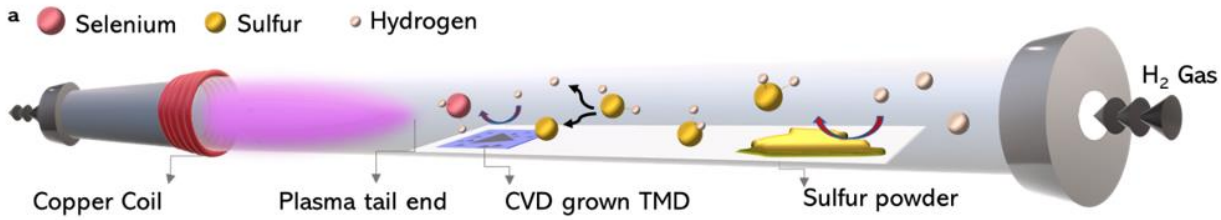

Figure 3.4 Schematic demonstration of the SEAR process through inductively coupled plasma

The induced electric and magnetic field accelerates electrons inside the chamber, and the strength of this field decreases with distance. This implies the carrier gas can ionize and dissociate well beyond the length of visible plasma tail on downstream as well as the upstream region. This invisible region is exceptionally crucial in our process and helps in stripping the top layer of chalcogen atoms at a languid pace.

The creation of Janus TMDs with the SEAR method was carried out in a home-built inductively coupled plasma setup. A 5-foot long quartz tube with 1-inch diameter was used as the processing chamber and kept off-centered on a Lindberg Blue/M single zone furnace. The furnace also acts as a grounding medium for the residual charges on the tube (if any). A 1.5-inch Cu inductor with five turns was fitted onto the center of the quartz tube. The end of the copper coil was connected to a 100W tunable RF power supply through an impedance match network. The reaction system was pumped down to a base pressure of 15 mTorr, after which the chamber was purged with 20 sccm H_2, maintaining an operation

pressure at 300 mTorr. Plasma was generated with 15W RF power, and the visible plasma tail position was marked on the quartz tube.

The SEAR process can be set up to create any 2D Janus structure from selenium as well as sulfur-based TMDs by merely varying the processing parameters. In the scope of this work, stripping of selenium atoms from the top of CVD grown and exfoliated monolayer was performed. $MoSe_2$, WSe_2, MoS_2, $NbSe_2$, and superlattices were effectively etched and converted into their respective Janus crystals using this method. The etching was performed in the range of eight to twenty-five mins while keeping the rest of the parameters as constant. Further, all SEAR samples were initially placed within the chamber without any chalcogen source; This was done in order to identify optimum processing time. These samples were then characterized using Raman spectroscopy.

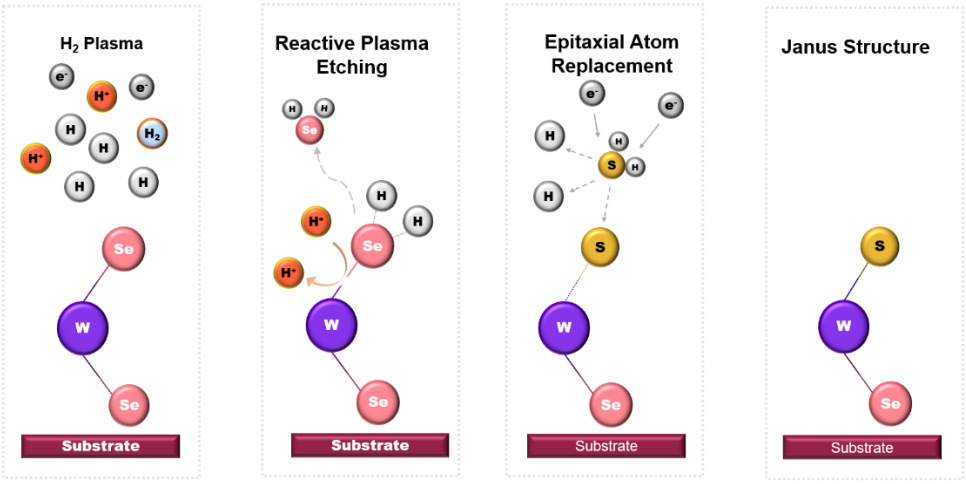

Figure 3.5 Working scheme of room temperature SEAR process

Successful etching can be identified by the loss of Raman intensity by the parent material from the stripping process once an optimum processing time has been established. One can radically vary the position of TMDs to optimize the etching rate further. After

SEAR parameters have been established, a sample substrate can be kept within the chamber in the presence of a chalcogen source for successful Janus synthesis. Establishing the SEAR parameters is essential whenever a new transition metal within a TMD is used. Depending upon the binding energy of the transition metal, the processing time for the SEAR process can be easily varied. This initial step is also necessary to ensure that the samples are not under-etched or over etched when kept within the chamber.

Determination of position is also crucial as a sample closer to the visible plasma tail experience a higher rate of ion bombardment and eventually suffer surface damage. This could arise due to excess of ions flowing over the downstream region from the plasma (as well inside plasma), which might obliterate the sample or could result in random etching. This implies that both the top and bottom layer of chalcogen atom undergo etching simultaneously at some regions on a monolayer flake, which in turn causes local diffusion of chalcogen atoms. All the situations mentioned above also affect the replacing chalcogen source.

Another important consideration is the rate of etching/stripping of the top chalcogen layer. In order to successfully synthesize Janus materials, the stripping process must be as gentle as possible to avoid over-etching as well as randomized etching. As the top chalcogen layer is getting etched, there will arise a high concentration gradient of these chalcogen atoms in the vicinity of the sample, and this gradient will drive the diffusion of some of the bottom chalcogen atoms to the top. As the etching continues, the ions also start knocking the bottom chalcogen atoms, thus creating vacancies and defects within the crystal. Since the metal sites become very active during stripping of the chalcogen from

the top, it eventually leads into strong diffusion of bottom chalcogen layer and re-emergence of the original TMD in some regions of the monolayer in a randomized manner. In this way, it is never possible for the process to completely strip the top layer of selenium in the absence of a replacement chalcogen source.

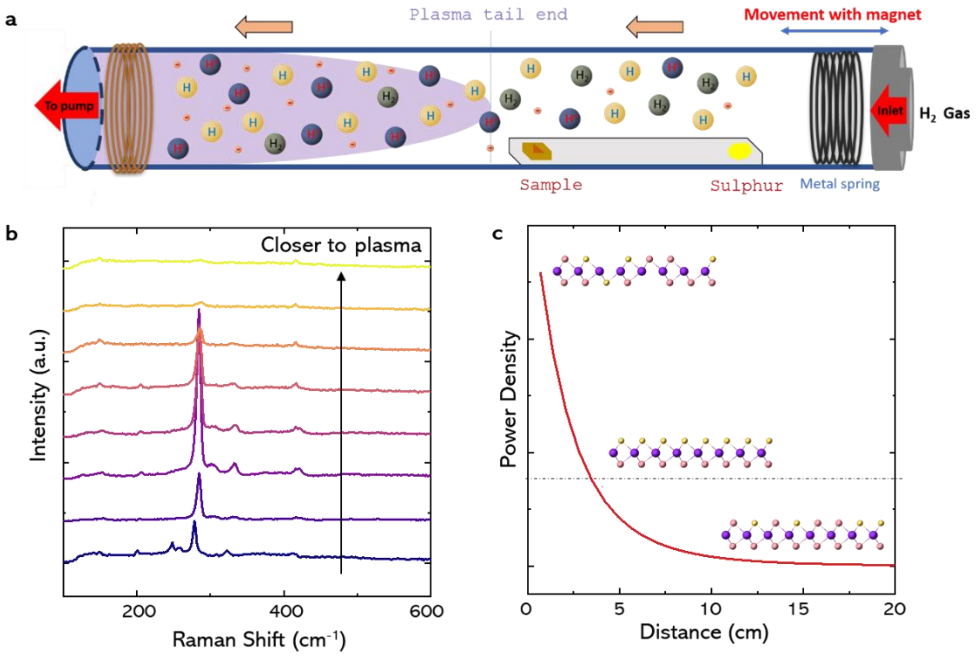

Figure 3.6 (a) Schematic of the SEAR process setup (b) The effect of TMDs layer distance from plasma tail on the efficiency for SEARs (c) Impact of Plasma gradient on material structure

The degree of over-etching is also dependent on the chalcogen source and the initial atom it is replacing in the TMD. Since the synthesis of the same Janus material can be approached by using different chalcogen based TMDS, precedence is given to replacement of selenium atoms in the TMD from sulfur source as it is energetically favorable to create Janus MoSSe from $MoSe_2$ instead of MoS_2. This can be explained based on the following argument. Since dissociation of a molecule into free radical requires significantly less

energy than ionization, the extent of hydrogen radicals in the plasma chamber is far beyond the visible plasma tail. These hydrogen radicals are highly reactive and get readily adsorbed on the surface of sulfur that is used as a replacement chalcogen. This deliberately helps in the formation of H_2S gas, which passes on top of the TMD substrate that kept downstream. The formation of plasma also creates hydrogen ions beyond the length of plasma, but the quantity of ions is far less than it is in the actual plasma region. H_2S gas molecules eventually pass over the sample substrate, where the magnetic field and electrical field strength. The energy from the coil is enough for the dissociation of H_2S molecule again into hydrogen and sulfur ions. The process of formation and dissociation of H_2S continues while passing over the sample substrate.

Species	Ionization energy (eV)	Dissociation energy (eV)
H	13.59	-
S	10.36	-
Se	9.75	-
H_2	-	2.27
H_2S	-	2.7
HS	-	1.95
H_2Se	-	2.36
HSe	-	1.72

Table 3-1. Ionization and dissociation energies calculated for select radicals and molecules participating in the SEAR process.

*Calculated using DFT by our collaborator Prof. Houlong Zhuang using finite displacement analysis***.**

The as-formed sulfur interacts with the surface and occupies vacant selenium sites, thus completing the formation of Janus TMD. The Janus TMD will not undergo further dissociation or etching since it is more stable than the parent TMD structure and requires more energy dissociation into constituent elements (i.e., moving substrate closer to the

plasma tail). Since the binding energy of H_2Se is much higher than H_2S, ionizing H_2Se into hydrogen and selenium is energetically intensive, and readsorption of selenium atoms in the vacant sulfur sites is much more challenging. It is also essential to optimize the distance of the chalcogen source from the plasma tail end. This distance is mainly decided based on the RF power of the plasma and the number of winding of the helical coil used in the process. Additionally, on all the other parameters that were mentioned, which affects the length and density of the plasma.

3.3. Processing Parameters:

3.3.1. Effect of Time

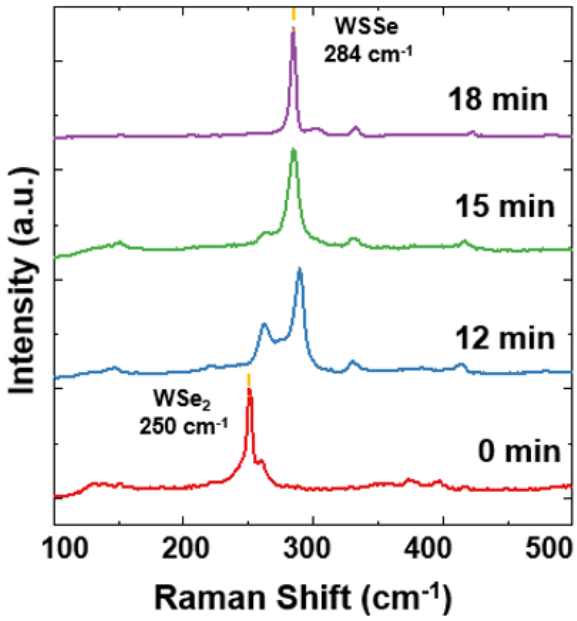

Figure 3.7 The evolution of Raman spectra of WSe_2 to Janus WSSe during the SEAR process with respect to time

Figure 3.7 shows a range of different SEAR processing time. When the sulfur powder is placed far away from the plasma tail, H_2S and S radical concentrations are significantly

reduced at the WSe_2 site. As such, the SEAR process is not sufficient, and incomplete replacement happens. As we move sulfur precursor closer to the sample, the SEAR process becomes highly effective, and Janus monolayer formation is successful. Similarly, the SEAR process time ultimately dictates how much chalcogen replacement takes place. Insufficient time (12 or 15 minutes) produce Janus layers with rather broad Raman signals. Only after enough time (18 minutes) the process yields highly crystalline Janus layers with a sharp Raman peak. We note that extensive processing time is also harmful since the samples undergo a more prolonged plasma exposure

3.3.2. Effect Of Position

The SEAR process with sulfur as the chalcogen source was carried out three samples of $MoSe_2$ to understand the effect of position on the sample substrate. The plasma parameters were kept constant during the process, and distances of the sample were varied from the plasma tail. The replacement chalcogen source was also kept constant during the entire synthesis step.

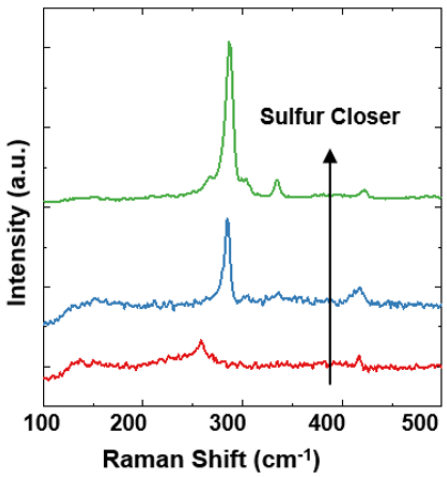

Figure 3.8 The evolution of Raman spectra of WSe_2 to Janus WSSe during the SEAR process with respect to time

The degree of stripping and sulfurization of the sample concerning the distance of the sample from the plasma tail is depicted in figure 3.8. The sample which was closest to the plasma tail end gets completely etched with a robust signal coming from SeMoS Janus structure. This is an optimum distance, and keeping the samples further downstream will result in the introduction of defects. On increasing the distance of the sample from the plasma tail end, there was an emergence of the shoulder on the left (lower frequency), which comes from the parent structure of $MoSe_2$. One can also observe a shift in the out-of-plane SeMoS peak at lower frequencies, which is an indication of incomplete etching of $MoSe_2$ flake.

In conclusion, there are also some top layer Se sites (heavy atom) bonded with Mo, which dampens the higher frequency of vibration caused by the bond of S atoms (lighter atom). This behavior can also be attributed to defects in the SeMoS structure, which could cause Raman signals to move away from the gamma symmetry point, as discussed before. These results are also consistent with SeWS Janus and indicate a universal attribute of the SEAR process.

3.4. SEAR Synthesis of Janus Mo-S-Se

The SEAR setup was initially designed to operate in two steps. First, the top layer of atoms within TMD material will be stripped completely, followed by a sulfurization step to fill the now-vacant chalcogen sites. The second step, therefore, can be undertaken in two-ways, Ex-Situ, or in-Situ sulfurization. In the case of ex-situ sulfurization, there are chances of oxidizing the Mo sites if the vacuum within the chamber is broken, furthermore removing the sample from the reaction chamber also poses a risk of introducing foreign contaminants

within the chamber that will alter the reaction process later. Naturally, In -Situ, sulfurization is therefore preferred to overcome these drawbacks. There, however, exist one tiny shortcoming of the Insitu process. Once the sample is loaded into the chamber, its position cannot be altered or tampered in case of discrepancies arising from vacuum equipment such as leakage Or power loss from the impedance network. The process parameters might change significantly and could result in poor repeatability.

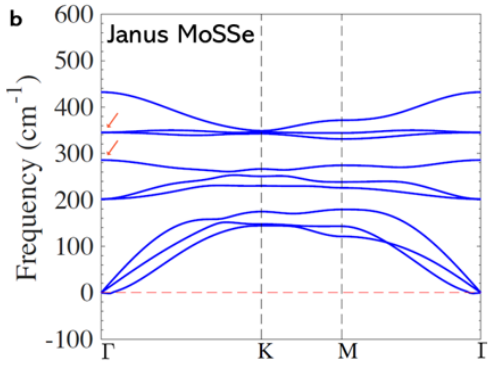

Figure 3.9 Calculated Phonon Dispersion of Janus MoSSE
*Calculated using finite displacement analysis by our collaborator Prof. Houlong Zhuang***.**

Insitu sulfurization was carried out in the same 1" quartz tube. A quartz boat containing $MoSe_2$ samples were placed at a pre-marked position where an optimum etching rate was observed. The chalcogen source in the form of sulfur powder (Sigma-Aldrich, 99.98% purity) was kept within the tube. The tube was initially pumped down to a base pressure of 15 mTorr and there for fifteen minutes. This was done in order to ensure that no residual gases remained within the tube during the SEAR process. After fifteen minutes, the chamber was flushed with high purity hydrogen gas for another ten minutes to ensure that there exists a uniform flow and concentration gradient of hydrogen gas throughout the tube.

Once the flow rate of the gas within the system has been stabilized, the operating pressure within the tube is recorded (280-320 mTorr) to ensure consistency with the initial trial runs. 15W power is applied through an RF source operating at 13.56 MHz to the copper coil. An impedance matching network is also connected to ensure lossless power to the coil. Once the pressure within the chamber has stabilized, the synthesis of Janus MoSSe is carried out [163, 164]for eleven minutes. After the processing time, the chamber is once again pumped down to lower pressure by shutting off the gas line. The vents on the chamber are slowly opened, and the substrate is further characterized using Raman and PL spectroscopy.

3.5. Characterization of Janus Mo-S-Se

3.5.1. Atomic Force Microscopy

The topology and height profile post SEAR process were measured by NT-MDT Atomic Force Microscopy setup in a non-contact AFM tapping mode. Janus monolayer on SiO2/Si substrate was raster-scanned with 512-pixel density. It was found that the thickness is still in the monolayer limit and is in good agreement with the established literature[165, 166], and however one cannot observe changes in the lateral height to a precise degree, and further characterization is needed using TEM to see the changes in the unit cell before and after the processing. Another interesting assessment that can be made from the AFM scans is the emergence of cracks on the surface of the monolayer. The ions within the plasma continuously bombard the surface and knock off the top selenium atoms, Since these ions have a high energy density, their interaction with the TMD surface often leads to cracks on

the surface due to their high impact energies. A Possibility of mitigating these surface cracks can exist if the interaction of the plasma with the substrate is limited.

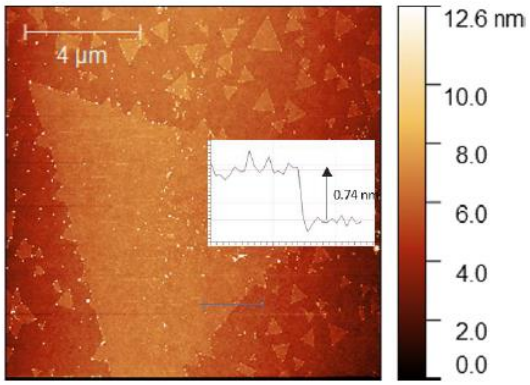

Figure 3.10 AFM height profile of MoSSe Janus

This can be achieved by keeping the substrate far away from the invisible plasma tail and increasing the processing time, which could result in fewer cracks. Interestingly if MoSSe Janus materials are synthesized from MoS_2 instead of $MoSe_2$, then the replacement of sulfur by selenium atoms usually results in significant defects and huge holes. This is attributed to ionization of Se (much more massive and thus high impact energies).

3.5.2. Raman and PL Spectroscopy

The Raman and photoluminescence (PL) spectra of homogenous MoSSe grown via the room-temperature SEAR technique is taken with a blue laser (488 nm) at 5% power and ten seconds of exposure.

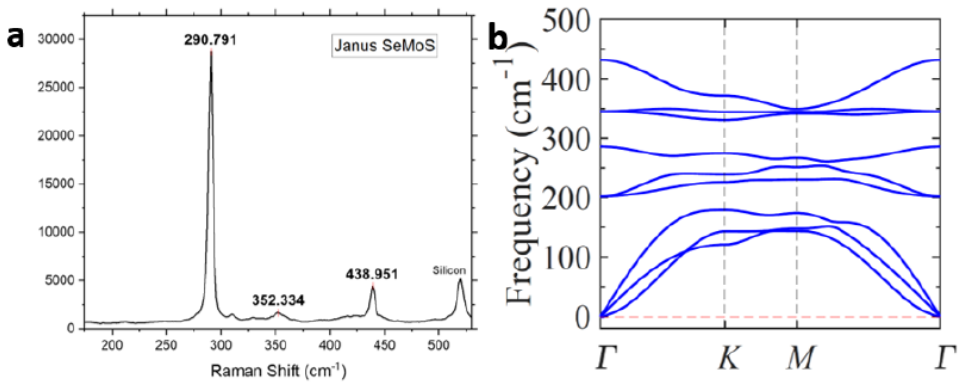

Figure 3.11 (a) Raman Spectra of MoSSe janus & (b) corresponding phonon dispersion for Janus MoSSe

*(b) was Calculated using finite displacement analysis by our collaborator Prof. Houlong Zhuang***.**

The Raman spectra of Janus MoSSe is significantly different when compared with their parent TMD materials (i.e., MoS_2, $MoSe_2$). The observed Raman spectra also differ from 2D alloy MoSSe. Moreover, our calculated vibrational dispersion, together with the Published predictions for MoSSe, match reasonably well with our experimental datasets. These observations validate that the as-synthesized layers have a Janus structure instead of random alloying. The intense peak at 290.8 cm^{-1} indicates the out-of-plane A_{1g} mode, while a small peak observed at 352.3 cm^{-1} is an in-plane E_{12g} mode of vibration. Another peek at 438.9 cm^{-1} was also observed and represented a B_{12g} mode of vibration. This peak has only been observed with a blue laser and showed a very diminishing behavior when low energy green (532 nm) and red (633 nm) lasers were used; this indicates that the mode can only be observed at higher energies.

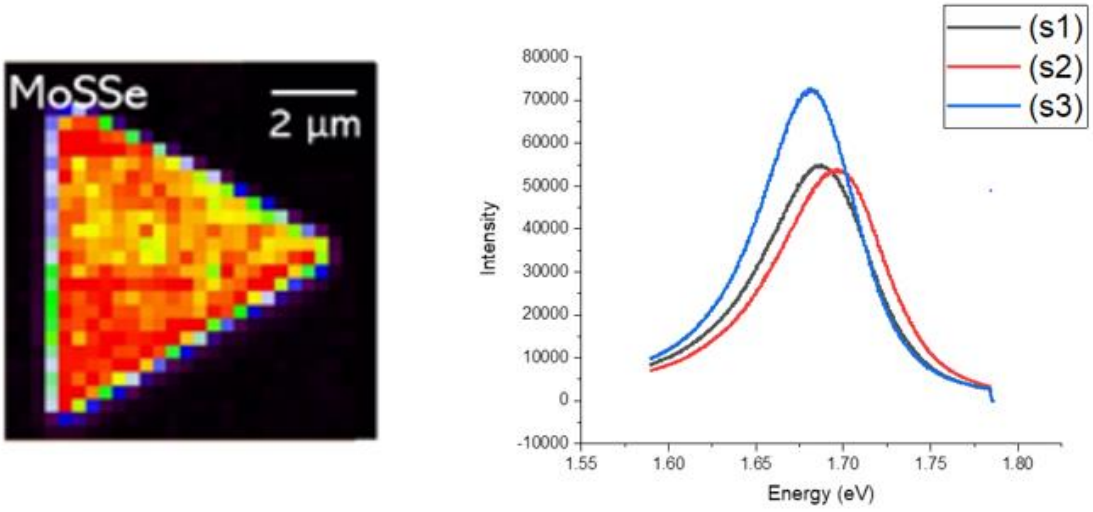

Figure 3.12 Raman mapping of MoSSe at 290 cm-1 (left) and corresponding PL Spectra at 1.68 eV (right) taken from three different substrates s1, s2 and s3 indicating repeatability of the SEAR technique

Overall, 2D Raman maps at the characteristic Janus vibrational mode 290 cm^{-1} for MoSSe show a remarkable uniformity across the synthesized 2D Janus layers. More importantly, the FWHM of the synthesized 2D Janus TMDs reaches as low as ~ 5.1 cm^{-1}. These values are much smaller compared to Janus MoSSe produced by the previous techniques and are comparable to high-quality conventional TMDs crystals[145, 146].

The photoluminescence (PL) spectra of the SeMoS Janus structure was also measured with similar setup and parameters. The PL peak position was observed to be at 1.67 eV. This is in excellent agreement with the first principle calculations. The observed Janus PL spectra show a blue shift when compared to the PL spectra of its parent structure, i.e., $MoSe_2$ (1.51 eV) [100, 143, 167, 168]. The measured PL spectra also substantiate the high crystal quality given that the PL intensity is comparable to that of CVD grown classical TMD monolayer. The PL FWHM is at least 30-40% sharper compared to the PL

from Janus crystals produced by high-temperature methods; this indicates the advantages of SEAR processing over its contemporaries[145, 146]. PL mapping also shows similar intensity across the entire sample, thus indicating the true nature of conversion this technique offers.

3.5.3. Power dependent and Low-Temperature PL Spectroscopy

In addition to carrying out PL spectroscopy at room temperatures, another set of measurements were carried out at cryogenic temperatures (4 -10K) in order to understand the excitonic dynamics of these crystals. Since the defects do not play a significant role at such temperatures, the emission energy is understood to be strongly dependent on the symmetry alone, and thus sharp peaks can be observed and analyzed.

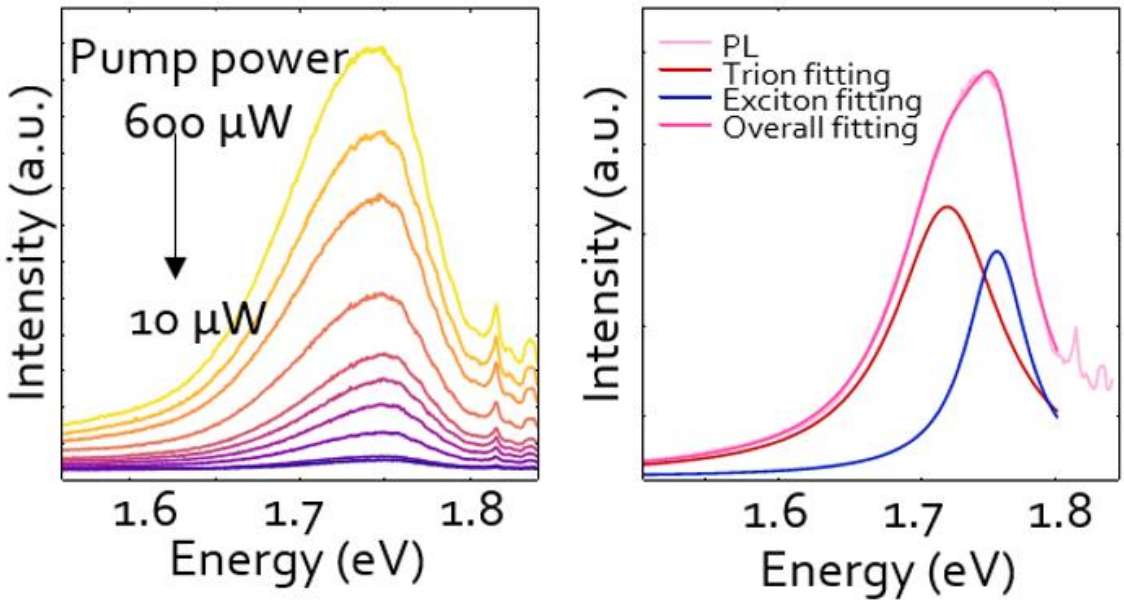

Figure 3.13 (left) Powerdependent PL of MoSSe at 10K, (right) Fitted power dependence of peakintensity vs excitation power

The emission energy of the 2D Janus MoSSe at 10 K is found to be 1.75 eV, whereas, at room temperature, the energy is measured to be about 1.68 eV. The excitonic

nature of these PL peaks is apparent from the power-dependent measurements. The PL intensity of MoSSe yields an almost linear slope ($\alpha \sim 0.99$), suggesting monomolecular (excitonic) recombination processes[52, 169]. Some of the PL spectra collected are broader and asymmetric, which can be interpreted as the convolution of at least two peaks. Power dependent emission shows that the intensity of the low energy peak has a higher slope with excitation power (exponent ~1.07 ± 0.01) than the high-energy peak (slope ~ 0.95 ± 0.02), thus suggesting the presence of co-existing many-body states, possibly trions and neutral excitons[170].

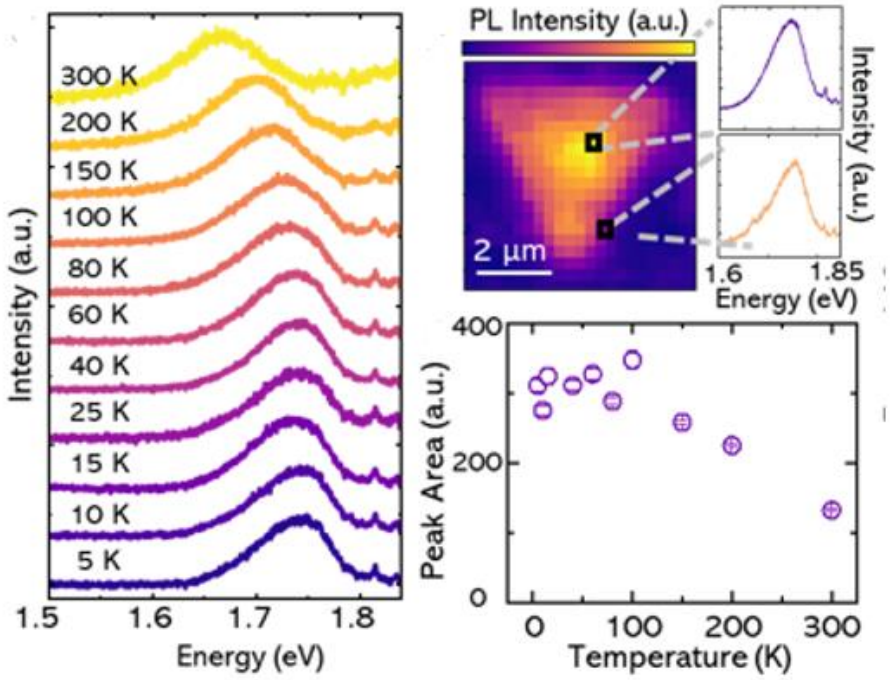

Figure 3.14 (Left) Temperature dependent PL spectra (300 K-10 K). (Top-Right) PL mapping (10 K) and (Bottom-right) PL peak intensity (integrated area) vs. temperature for Janus WSSe.

Temperature-dependent PL measurements on 2D Janus MoSSe layers show two main effects. First, the position of the PL peak is fitted with a Lorentzian function, and the PL peak positions show a hypsochromic shift at lower temperatures and the PL line shape becomes narrower, Here, the variation of the PL peak position with temperature can be well-explained within Varshni law, $E_g(T) = E_g(0) - \frac{\alpha T^2}{T+\beta}$, which has been successfully used for traditional semiconductors as well as 2D $MoSe_2$, and WSe_2. Typical Varshni fitting process offers excellent fit with $E_g(0) = 1.74\ eV$, $\alpha = 3.95 \times 10^{-4}\ eV/K$, $\beta = 216.71\ K$ for MoSSe[147].

PL mapping at low temperatures reveals that the PL emission intensity and wavelength have some degree of variation across the sample. Interestingly, Some of the layers exhibit an edge PL enhancement effect. The PL spectra collected from the edges and the other segments of the 2D Janus layers show that PL peak shifts by ΔE ~ 40 meV. This ΔE value is comparable with the ionization energy of charged excitons observed in classical TMDs (~ 20 - 40 meV), suggesting an interplay between neutral and charged exciton complexes [171, 172]. The outer regions of the Janus monolayers may have a higher defect density and a different charge-doping distribution compared to the central region, which increases photoluminescence at these positions as well as shifts the emission energy. This defect and charge inhomogeneity may arise from a non-uniform substitution of the selenide atoms during the growth process, which could further explain the observed PL intensity and emission energy pattern.

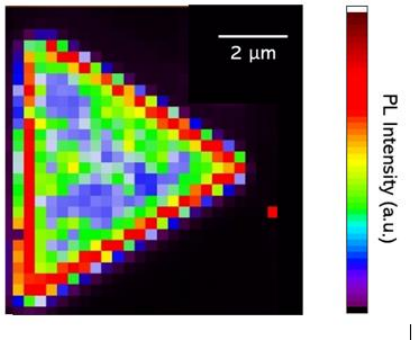

Figure 3.15 MoSSe PL peak area mapping with peak center at 1.68 eV with a bandwidth of 95 meV (room temperature)

3.6. SEAR Synthesis of Janus W-S-Se

In order to demonstrate the versatility of the SEAR process, synthesis of a theoretically predicted Janus material (WSSe) was undertaken using tungsten-based TMD as the parent structure. The structural and vibrational analysis based on first-principle calculations has shown that Janus WSSe forms a dynamically stable structure in the 2H phase. Owing to its non-centrosymmetric structure, the monolayer Janus has two in-plane (E) and two out-of-plane (A) Raman active phonon modes. The eigenfrequencies of the prominent Raman active modes were predicted to be 277 (A) and 322 (E) cm^{-1} [167]. For the synthesis of WSSe Janus, monolayer WSe_2 was grown on sapphire by means of atmospheric pressure-chemical vapor deposition using the parameters mentioned before. Before the synthesis, the as-grown WSe_2 monolayer on the sapphire substrate was initially characterized with the help of Raman and PL spectroscopy for identifying the optical quality of the starting material. Since the element that is being replaced is the same in both the cases (Se), a protocol like the SEAR synthesis of MoSSe was followed. However, modification of the SEAR chamber was adapted in order to enable Insitu Raman and PL measurements in the

future. The new SEAR chamber was designed to dramatically reduce the interaction of ionized plasma with the sample substrate. One observation that was made based on the previous design was that the uniform distribution of the ionized plasma due to the geometry of the chamber results in severe cracking of the TMD monolayer.

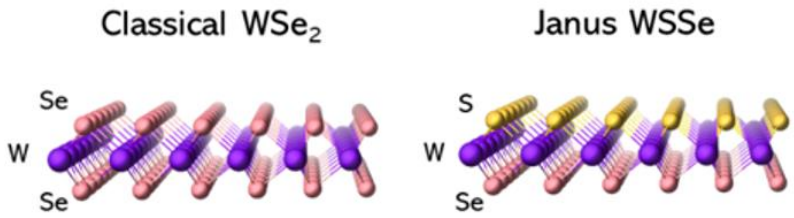

Figure 3.16 The crystal structure of WSe_2 monolayer and WSSe Janus monolayer

This can be attributed to the change in edge to center Plasma density ratios in two-dimensional plasma discharges. As one approaches closer to the visible plasma tail, the etching effect due to collisions increases, however, the geometry of the tube imparts asymmetric plasma density around the visible plasma tail. This effectively reduces the working distance in which one can effectively etch the TMD without causing further damage. In order to mitigate this disadvantage, the following modification in the geometry of the tube was adopted. The new chamber was also equipped to enable objective lenses within a 2 cm working distance. Since the determination of optimum working parameters requires several trial and error measurements, a modification of the chamber was created in order to facilitate in situ Raman and PL measurements in the future. Furthermore, two capacitance manometers and a pressure control valve were attached to the new chamber to control the pressure within five mTorr tolerance accurately.

The as-grown WSe_2 monolayers were loaded into the new SEAR chamber at ~300 mTorr operating pressure in the presence of high purity 16 sccm H_2 gas. The flow-rate within the new chamber was adjusted in order to mimic operating pressure within the previous studies. The samples were kept at the center of the chamber where the plasma density is visibly dilated. Inductively coupled plasma was generated by supplying 15W RF power at 13.56 MHz frequency to a copper coil, which ionizes and disassociated H_2 molecules into H^+ ions and H free radicals. The concentration of ionized species and the extent of the plasma tail is once again controlled by varying the RF power. Since the newer geometry enables very low plasma density, the sufficient working distance within the camber was dramatically increased, Similarly the newer geometry enables the generation of plasma input powers than before.

In the process of Janus WSSe conversion from WSe_2, hydrogen radicals are first adsorbed on WSe_2 and form weak bonds with the top Se atoms, creating intermediate species. Highly energetic hydrogen ions bombard and knock-off these intermediates, which result in Se vacancies as well as H_2Se/HSe^+ byproducts, as established in the literature[146]. Like MoSSe, we find that the distance from the plasma tail and exposure time ultimately dictates the Se vacancy generation rate; when increasing the distance beyond the ideal position, vacancy creation becomes inefficient and prevents Janus structure formation. Similarly, moving samples closer to the plasma tail exposes monolayers to energetic ions and results in heavily defected samples. Another crucial part of the Janus synthesis is the introduction of sulfur upstream from the TMDs sample in the SEAR process, which helps in the effective incorporation of sulfur atoms into plasma

stripped WSe_2 monolayers without any thermal assistance. Since the dissociation energy is much lower than the required energy for ionization, the extent of hydrogen radicals is far beyond the visible plasma glow, which results in the formation of H_2S vapor near the sulfur through a similar reaction process described previously. The H_2S molecules are then transported towards the TMD sample by the gas flow and dissociate into individual radical species of S and H (by higher RF power). S radicals then incorporate into the chemically active V_{Se} sites to form a stable WSSe Janus structure. The Se etching and S replacement processes happen simultaneously and continue until all the upper Se are replaced by S.

Additionally, as the cohesive energy with respect to selenium is higher in tungsten when compared with molybdenum, care must be taken to adjust the stripping time for the synthesis of Janus WSSe. Well-optimized processing times and enough supply of sulfur (in the form of H_2S or S radicals) are required to prevent over-etching, to stabilize the Janus structure, and to create highly crystalline Janus layers of WSSe. Post synthesis Raman and PL characterization were performed with the same setup as mentioned for characterizing $MoSe_2$ and SeMoS.

3.7. Characterization of Janus W-S-Se

3.7.1. Atomic Force Microscopy

The topology and height profile post SEAR process were measured by NT-MDT Atomic Force Microscopy setup in a non-contact AFM tapping mode. Janus monolayer on SiO2/Si substrate was raster-scanned with 512-pixel density. Once more, it is evident from Fig 3.17 that the SEAR process does not cause any detrimental surface damage, as evidenced in the post SEAR AFM topography for WSSe Janus monolayer. Furthermore,

the profile observed from before and after the SEAR process shows no significant change in the lateral height and is consistent with the established literature [166, 173].

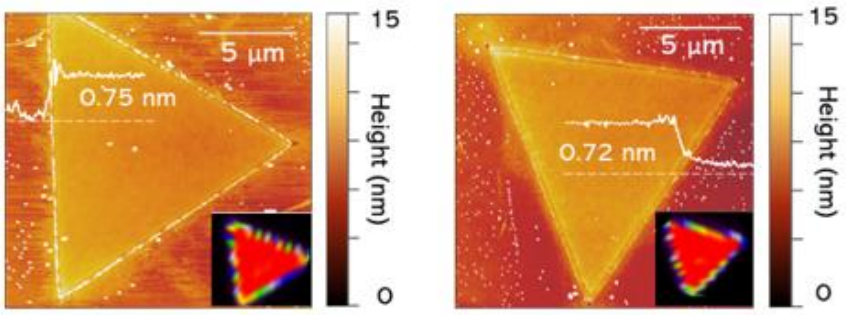

Figure 3.17 AFM Height profile of WSe_2 (left) prior conversion and AFM Height profile of Janus WSSe post SEAR (right)

3.7.2. Raman and Photoluminescence Spectroscopy

The Raman and photoluminescence (PL) spectra of homogenous WSSe grown via the room-temperature SEAR technique was also taken with a blue laser (488 nm) at 5% power with ten seconds of exposure time. Like Janus MoSSe, the Raman spectra of Janus WSSe is entirely different when compared with their parent TMD materials (i.e., WS_2, WSe_2). The new emerging peaks of Janus WSSe peaks were observed to be at 284.51 cm^{-1} and 333.18 $cm^{-1,}$ which are in close agreement with the first principle DFT calculations, as evident from the phonon dispersion calculation[117, 167]. The peak at 284.51 cm^{-1} is an out-of-plane A_{1g} mode of vibration, while a peak at 333.18 cm^{-1} is an in-plane E^{12}_{g} mode of vibration.

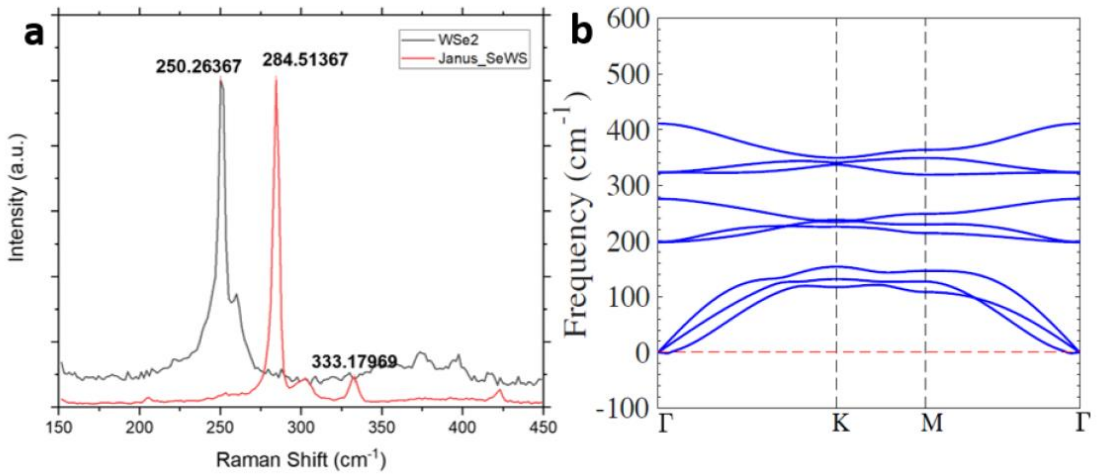

Figure 3.18 (a) Raman spectra of WSe_2 monolayer (black) as compared to WSSe Janus (red), (b) Corresponding phonon dispersion spectra of WSSe Janus

*(b) Calculated using DFT by our collaborator Prof. Houlong Zhuang***.**

The observed Raman spectra also differ significantly from 2D alloy WSSe. Moreover, our calculated vibrational dispersion, together with the published predictions for WSSe, also matches reasonably well with our experimental datasets with a deviation of around 1.1%. 2.8%, these deviations can be attributed to the induced strain within the monolayer as a result of CVD growth [173]. These observations validate that the as-synthesized layers have Janus structure instead of random alloying.

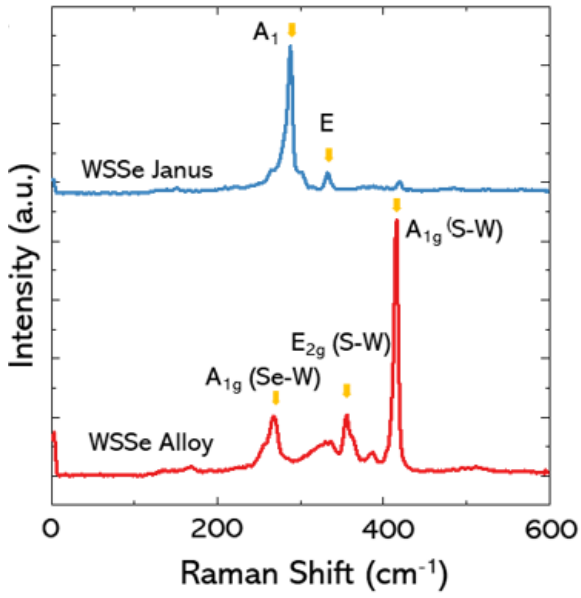

Figure 3.19 The Comparison between Janus WSSe and classical two-dimensional W-S-Se alloy

2D Raman maps at the characteristic Janus vibrational mode frequency of 284 cm^{-1} for WSSe also show a remarkable uniformity across the synthesized 2D Janus. Furthermore, The FWHM of A_{1g} mode of this new WSSe structure was even smaller than that of the actual WSe_2 growth dictating a very superior quality Janus structure creation that could be achieved if the parameters are optimized accordingly. The effects of the distance of the sample from the plasma tail end and the effects of duration of the SEAR process accounts to be one of the significant criteria for deciding the quality of new emerging structure with a replaced top atomic layer. Few experiments were carried out to determine optimum parameters for obtaining perfect crystalline Janus WSSe from a CVD grown WSe_2 monolayers.

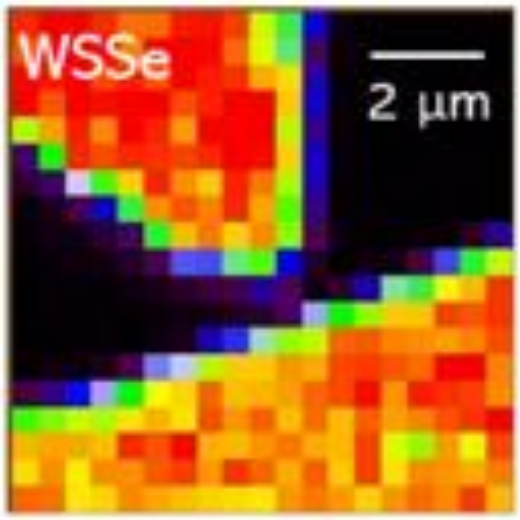

Figure 3.20 Collected Raman mapping from 2D Janus WSSe monolayer using prominent 284 cm^{-1} peak

Photoluminescence spectroscopy was performed on the as-synthesized Janus WSSe layers using the same Raman set up with the 5 % laser power and five sets of accumulations within ten seconds. The emission energy of the 2D Janus WSSe at room temperature was recorded to be around 1.78 eV, which once again is in excellent agreement with the established literature as well as out DFT studies. Furthermore, the PL intensity for the Janus structure is comparable to that of CVD grown classical TMD and does not diminish with plasma processing, and this indicated the gentle nature of synthesis and with the FWHM being at least 30% sharper. The PL mapping, in the case of WSSe Janus, also shows overall uniform intensity across the samples.

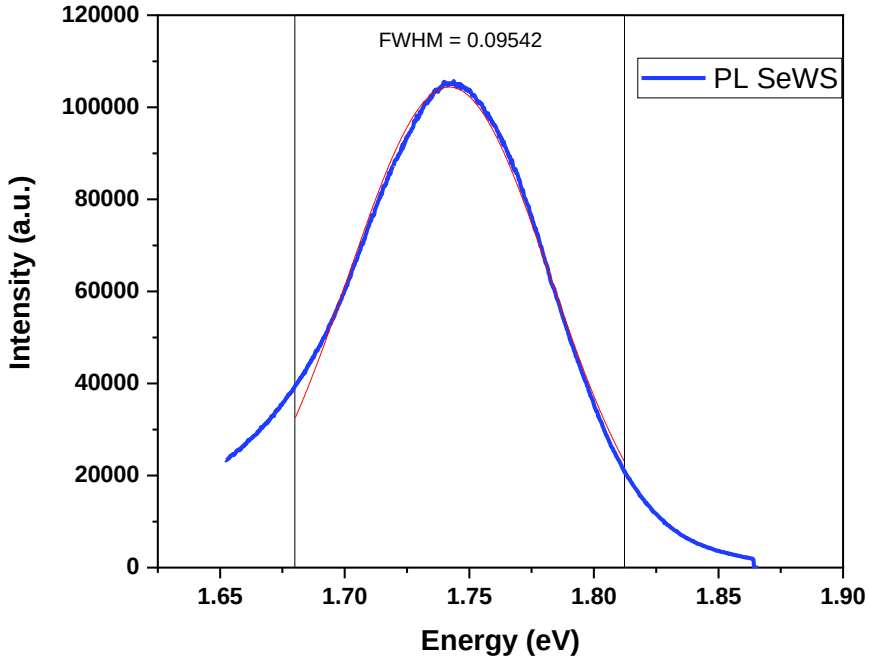

Figure 3.21 PL Spectra of 2D Janus WSSe with FWHM measuring, indicating a high degree of crystallinity.

3.7.3. Low-Temperature Raman and PL Spectroscopy

Low-Temperature Raman and PL measurements were performed on Janus WSSe monolayers like our previous MoSSe measurements. These measurements were collected at cryogenic temperatures (4 -10K) in order to understand the excitonic dynamics of WSSe fully. The emission energy of the 2D Janus WSSe at 10 K is found to be 1.85 eV, whereas, at room temperature, the energy is measured to be about 1.78 eV. The PL intensity of WSSe also yielded a linear slope ($\alpha \sim 0.99$) from the power-dependent measurements, suggesting monomolecular excitonic recombination processes. Furthermore, WSSe PL spectra also

exhibit a broader peak suggesting the convolution of two peaks that are hypothesized to be neutral exciton and trions[170].

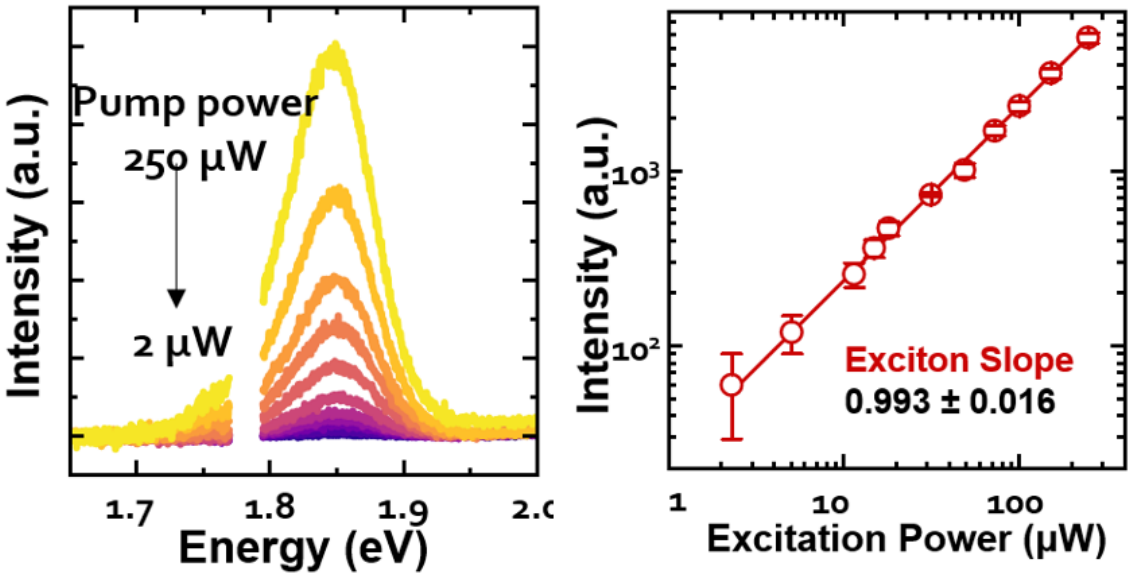

Figure 3.22 (left) Power Dependent PL of WSSe at 10K, (right) Fitted power dependence of peak intensity versus excitation power of WSSe

The Lorentzian fitting of these peaks at a lower temperature is also in excellent agreement with the typical Varshni fitting for these process with $E_g(0) = 1.87\ eV$, $\alpha = 5.09 \times 10^{-4}\ eV/K$, $\beta = 260.02\ K$ for monolayer WSSe furthermore, the integrated PL peak intensity increases with decreasing suggesting a bright exciton ground state, which is opposite to what is found for W-based classical TMDs and warrants further studies [147].

Like MoSSe, the overall PL emission intensity across an entire 2D Janus WSSe exhibit edge PL enhancement. The low-temperature PL mapping that the emission intensity and wavelength have some degree of variation across the sample. The ΔE is approximately 40 meV and comparable with the ionization energy of charged excitons observed in classical

TMDs once again, suggesting there is an interplay between neutral and charged exciton complexes[171].

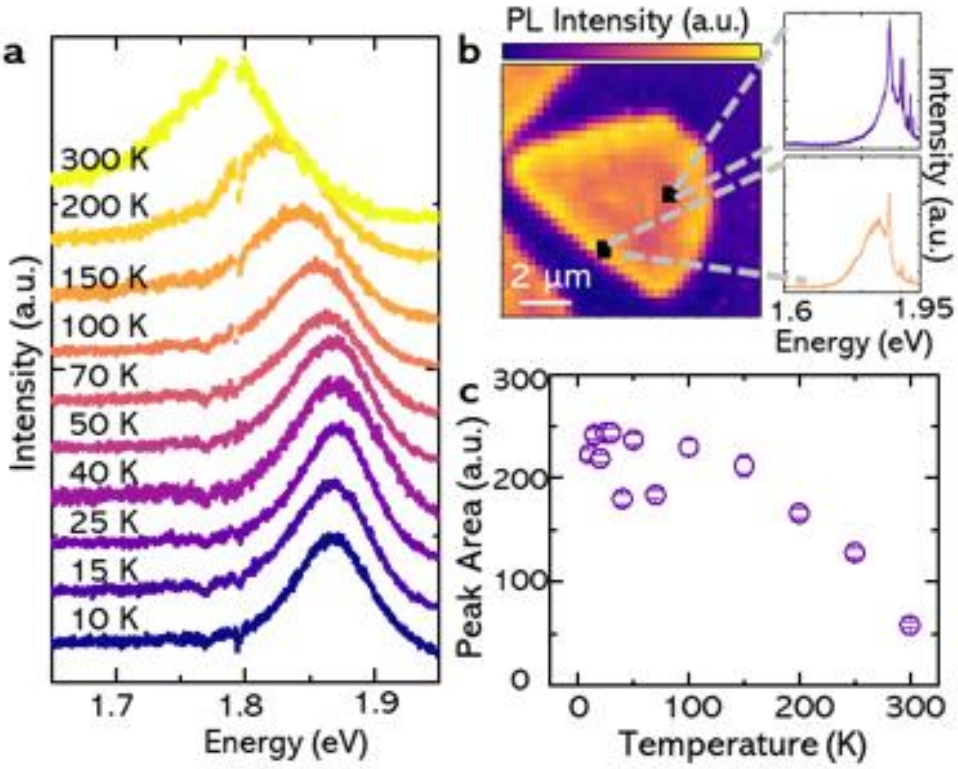

Figure 3.23 (a) Temperature-dependent PL spectra (b) PL mapping (10 K) and (c) PL peak intensity (integrated area) vs. temperature for Janus WSSe

Since the outer regions of the Janus monolayers may have a higher defect density and a different charge-doping distribution compared to the central region, there is an increase in the photoluminescence intensity at these positions as well as shifts the emission energy [174]. The charge inhomogeneity is attributed to a non-uniform substitution of the selenide atoms during the growth process and warrants further investigation.

4. Chapter 4 Selective Epitaxy Atomic Replacement: Superlattices

4.1. Introduction to 2D Heterostructures

Owing to the mild processing conditions of our ambient temperature synthesis, we aimed to demonstrate the first-of-a-kind realization of lateral and vertical heterostructures of 2D Janus layers. In addition to superior features of TMD single layers, bilayers of TMDs present significant properties for electronic devices with a scalable fabrication process via van der Waals assembly of TMDs. For instance, an ultrafast charge transfer has been demonstrated in the bilayer heterostructures of MoS_2 and WS_2, and the interlayer coupling in MoS_2/WS_2 bilayer can be tuned with a vacuum thermal annealing. Van der Waals heterostructures of molybdenum and tungsten chalcogenides with different configurations have been produced as photo-voltaic devices that possess spectacular electronic and optoelectronic properties.

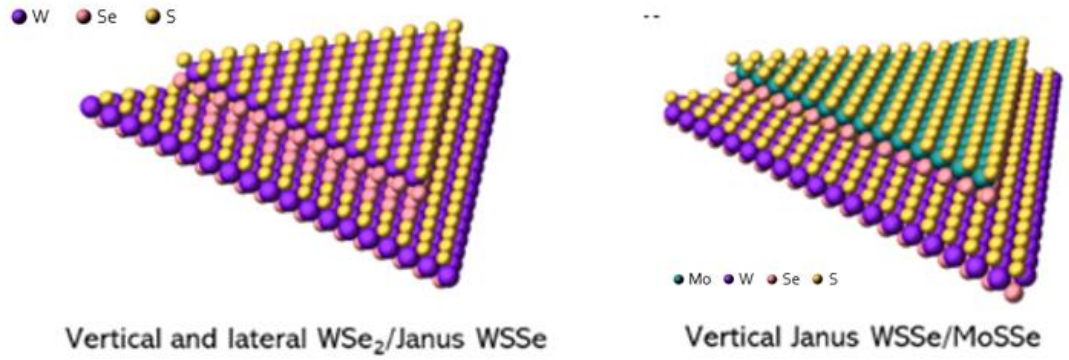

Figure 4.1 Schematic representation of Janus heterostructures

Since Janus TMD enhances many of the fascinating properties observed within regular transition metal chalcogenides owing to the broken mirror symmetry, superlattices of these structures will pose and demonstrate unusual quantum behavior that is just not possible to achieve within regular structures. Indeed, many theoretical studies have identified that vertical and lateral heterostructures of 2D Janus layers offer unique quantum effects and functionalities.

For instance, in MoSSe van der Waals (vdW) structures, the intrinsic electric field results in a broad interlayer band offset, which can be used as a driving force for interlayer excitons. These excitons can endow ultralong carrier lifetimes within the material and might further dissociate into free carriers. The stacking order in two dimensional Janus WSSe has also been shown to have distinctive Raman characteristics in their vibrational frequencies that stem from the different interlayer interactions within these materials. Furthermore, in WSSe/MoSSe van der Waals (vdW) heterostructures[117], the intralayer/interlayer potential drops lead to significantly larger band offset than MX_2 heterolayers, ensuring the long lifetimes for valley polarized interlayer excitons. The Rashba-type spin splitting has been predicted to co-exist with the valley spin splitting within these materials, and Rashba polarization can be enhanced in these vertical heterostructures due to improved electric polarity in the z-direction[104, 109, 115]. In the case of lateral heterostructures, the photoresponse and absorption coefficients show optical activity in a broad visible light range. It is of interest that both types of heterostructures reveal type-II band alignment, enabling the separation of excitons[84, 167].

Additionally, the grain boundaries in Janus MoSSe heterostructures behave as one-dimensional (1D) metallic quantum wires, suggesting the possible formation of a 1D electron or hole. Theoretical calculations on the energies of intra- and interlayer excitons as a function of film thickness, have revealed that the Janus multilayer films are ideally suited for achieving ultrafast charge separation over atomic length scales without the need for chemical doping or applied electric fields. The calculated density of states and electronic structures reveal that the introduction of in-gap states and a shift in the Fermi level in hydrogen adsorbed systems due to Janus asymmetry is the origin of an enhanced HER activity within these materials[143, 144].

Despite keen theoretical interest in these sophisticated structures, their synthesis has not been realized using other high-temperature processing techniques. The difficulty presented by the previous methods is that at high temperatures, it is easier to deteriorate one of the constituent materials, or it is more likely to form an alloy instead of 2D Janus layers. The SEAR process aims to circumvent this fundamental challenge by the creation of these fantastic structures.

TMD based lateral and vertical heterostructures have been synthesized using a variety of known experimental techniques such as AP-CVD, epitaxial growth on CVD thin films and deterministic transfer of monolayer TMDs, etc. In the scope of this thesis, two methodologies have been adopted for the creation of these remarkable structures. Firstly, a deterministic transfer approach was adopted in order to create vertical heterostructures of Janus MoSSe and WSSe. Secondly, two-step synthesis of Tungsten and Molybdenum TMD's were undertaken to create atomically stitched lateral heterosturres. These structures

were then transferred into the newly modified SEAR chamber to realize Janus lateral heterostructures. Finally, a vertical TMD heterostructure was created using AP-CVD by varying the process parameters; the as-synthesized vertical heterostructure was then converted to Janus-TMD vertical heterostructure using SEAR.

4.2. Vertical 2D TMDs

4.2.1. Deterministic Transfer of 2D Monolayers

For the creation of a vertical heterostructure of Janus MoSSe/WSSe, a standard PDMS-assisted transfer process was employed[167]. A thin layer of PDMS was placed on top of CVD-grown $MoSe_2$ on SiO_2, and the assembly was immersed in a 50 $^{\circ}$C 2M KOH solution for 1 min to etch SiO_2 away. The sample was then taken out and rinsed with DI water. PDMS was peeled off from SiO_2 and deterministically stamped on as-synthesized WSSe. After careful removal of the PDMS again, the $MoSe_2$/WSSe was then transformed to MoSSe/WSSe by the SEAR method. Further characterization of the superlattices was performed using Raman and PL spectroscopy.

4.2.2. CVD Synthesis: Bilayer WSe_2 heterostructure

The creation of Janus WSSe can be undertaken by converting WSe_2 bilayers into WSSe Janus by selenisation. Controlled synthesis of WSe_2 heterostructures is more accessible compared to $MoSe_2$ synthesis, and large domains of WSe_2 bilayers can be obtained through AP-CVD. Synthesis of Bilayer WSe_2 was obtained by keeping 60 mg of WO_3 precursor was placed in a ceramic boat at the center of the single-zone tube furnace. Double side polished sapphire substrates were placed on the ceramic boat. Selenium powder was placed

upstream in a ceramic crucible in excess, where the temperature was maintained at 250 °C. High purity Ar (≥99.99%) and H_2 gas were passed at 36 sccm and four sccm flow rates, respectively, during the entire growth process. The furnace was ramped up with a rate of 30 °C/min to 850 °C and held at 850 °C for 20 minutes before natural cooling to room temperature and held for 13 min before naturally cooling to room temperature. The as-synthesized flaked were then characterized using Raman spectroscopy.

4.2.3. SEAR Synthesis of Vertical Janus Heterostructure

Both types of vertical heterostructures, i.e., Bilayer MoS_2 and WSe_2, were converted into Janus MoSSe by using the modified SEAR chamber. In the case of Bilayer MoS_2, selenium precursor was used instead of sulfur for the conversion process. As mentioned before, since selenium will have high impact energy with the substrate, the chalcogen source was kept far away from the substrate to reduce the rate of impact. Although this does not reduce the impact energy of the ion, visual evidence from the optical images suggest that it does seem to influence the overall defects that are introduced on the TMD.

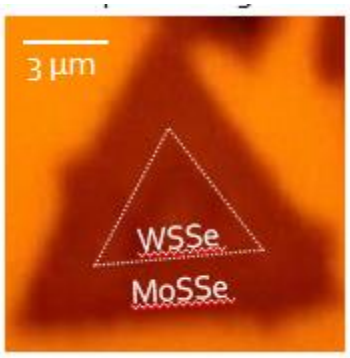

Figure 4.2 Optical Image of MoSSe/WSSe Vertical Heterostructure.

Further studies are, therefore, warranted in order to understand the underlying mechanism of the process thoroughly. The processing time was also decreased since the binding energy of MoS_2 is far less than that of $MoSe_2$. The newly created Janus structure consists of a TMD-Janus interface. The SEAR process successfully converts the exposed TMD structure in Janus; however, the underlying layer that was not exposed to the plasma treatment remains unchanged. The as-synthesized structure, therefore, has a Raman signal from MoS_2 as well as MoSSe Janus.

Another type of vertical heterostructure was created using WSe_2 and $MoSe_2$ monolayers. The substrate, in this case, we are also kept inside the modified SEAR chamber; however, the chalcogen source was replaced by Sulfur. In the creation of this bi-metal heterostructure, the processing time must be optimized in order to convert both the TMDs into their respective Janus structures. Since the binding energy of the tungsten-based TMD materials is higher than their respective molybdenum based TMDs, their conversion into Janus materials usually takes longer processing times; this, however, poses a problem in case of conversion of $MoSe_2$ into MoSSe Janus increasing the process times beyond the maximum limit will introduce defects. This drawback can be mitigated by altering the position of the substrate with respect to the plasma tail. In the case of the vertical bi-metal heterostructure, the position of the substrate with respect to the visible plasma tail was increased in order to make the stripping process slow and extremely gentle. The as-synthesized Janus structures were then characterized using Raman and PL spectroscopy.

4.3. Characterization of Janus Vertical Heterostructures

4.3.1. Raman Spectroscopy & Photoluminescence Spectroscopy

Since the synthesis of vertical heterostructures has restrictions due to the surface-limited nature of the SEAR process. For instance, when CVD-grown bilayer WSe_2, consisting of a more extensive monolayer base and a smaller WSe_2 triangle on top, undergoes our SEAR process, we find that the exposed selenium atoms are successfully replaced with sulfur. However, selenium atoms covered by the smaller WSe_2 triangle remain unaffected. As a result, the final structure has both vertical WSe_2/Janus WSSe and lateral WSSe/WSe_2 heterostructures.

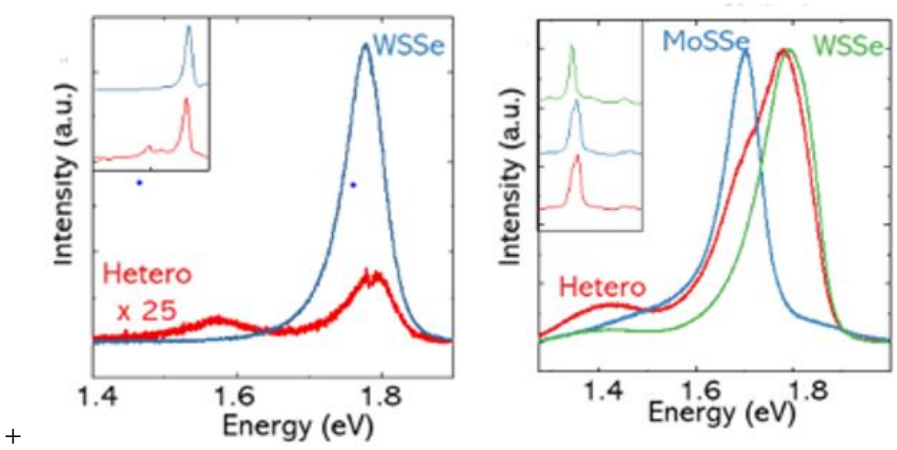

Figure 4.3 Comparison between edge WSSe area and center WSSe/WSe_2 area (Left) and PL spectra collected from Janus MoSSe, WSSe, and their vertical heterostructure regions (right)

Raman mapping at 250 cm^{-1} in shows that the underlying WSe_2 layer remains in the central triangular region. This suggests that the SEAR process is surface limited, and the reactive chalcogen or hydrogen radicals cannot intercalate between the layers. Since sulfur atoms successfully replaced all the exposed selenium atoms, the 284 cm^{-1} peaks for Janus WSSe can be found across the entire sample. Here, the central segment shows a slightly lower 284 cm^{-1} WSSe peak intensity.

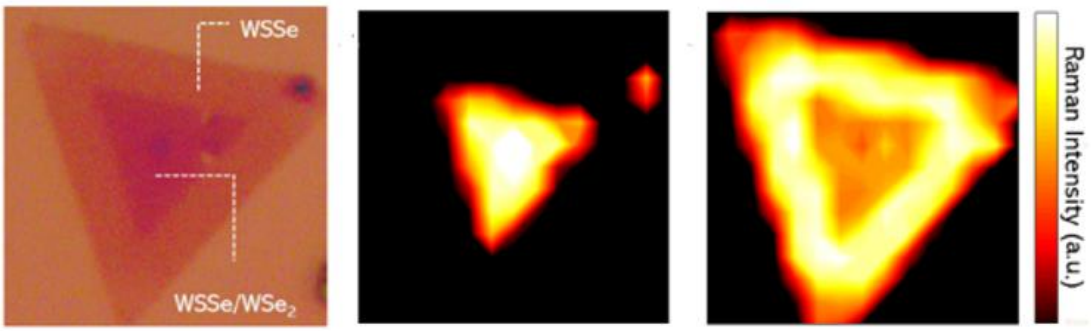

Figure 4.4 Optical image of Janus WSSe/WSe_2 vertical heterostructure (right) and corresponding Raman mapping of WSe_2 at 250 cm^{-1} (center) and WSSe at 284 cm^{-1} (left)

The observed Raman reduction in both WSSe and WSe_2 Raman signal on the vertical heterostructure is most likely related to the presence of interlayer coupling between WSe_2 and Janus WSSe layers, much like those observed in the classical bilayer and trilayer TMDs

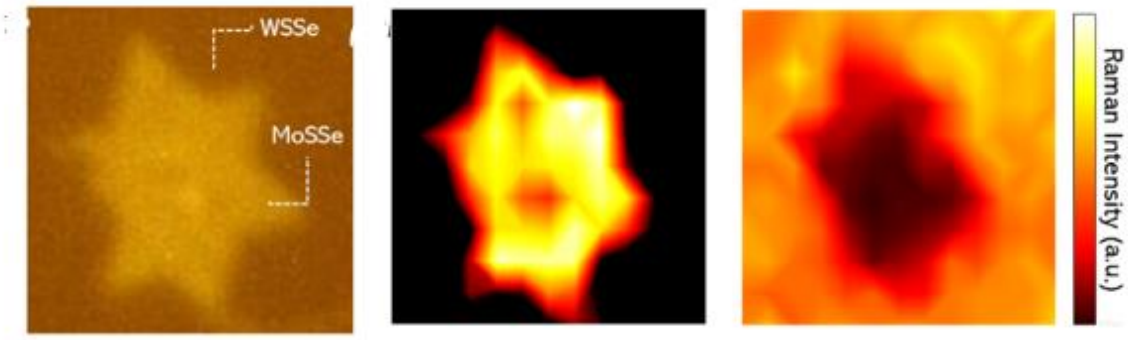

Figure 4.5 Optical image of vertical Janus MoSSe/WSSe heterostructure (left) , Raman mapping of MoSSe at 290 cm^{-1} (center) and WSSe peak 284 cm^{-1} (right)

To form truly 2D Janus vertical heterostructures and to further demonstrate the capability of the SEAR process, we have transferred monolayer $MoSe_2$ on Janus WSSe monolayers ($MoSe_2$/WSSe) using polymer assisted techniques before the SEAR process. During the conversion process, the exposed selenium atoms on the $MoSe_2$ monolayer got replaced by the sulfur atoms, but the underlying Janus WSSe layer, as well as exposed (monolayer) regions, remained intact to form 2D Janus MoSSe/WSSe vertical heterostructure.

Raman intensity mapping using the MoSSe A_1 mode at 290 cm^{-1} and the WSSe A_1 mode at 284 cm^{-1} demonstrate the formation of MoSSe/WSSe bilayer stacks as shown in The MoSSe signal is observed only from the central segment of the sample, while the other regions mainly yield WSSe related Raman peak. This suggests that it is possible to form MoSSe/WSSe vertical junctions starting with classical/Janus vertical heterolayers, followed by the SEAR process. The PL spectra acquired from the monolayer regions show sharp peaks at 1.68 eV and 1.78 eV, respectively, corresponding to the direct excitonic

transition energy in monolayer Janus MoSSe and WSSe. PL spectra collected from the bilayer MoSSe/WSSe region show that these two peaks co-exist with each other.

4.4. Lateral 2D TMDS

4.4.1. CVD Synthesis: $MoSe_2$-WSe_2 heterostructure

The CVD synthesis of $MoSe_2$ WSe_2 heterostructure was carried out in a two-step CVD approach. Since the synthesis of Tungsten based TMDS is carried out at a higher temperature, it was given precedence in the two-step synthesis approach. 285 nm SiO_2/Si substrates were initially cleaned with ethanol and IPA solution for ten minutes each.

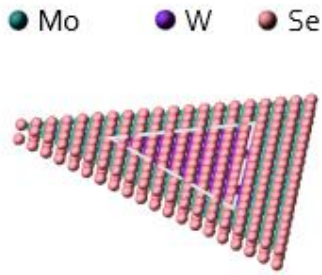

Figure 4.6 Schematic representation of TMD Lateral Heterostructure

The substrates were dried with nitrogen and cleaned with Argon plasma for another fifteen minutes to remove any surface contaminants. The cleaning process also increases the surface energy of the substrate that aids in the nucleation during the CVD reaction. After the cleaning process, one of the substrates was treated with a 50 μM solution of PTAS. The perylene salt solution helps in the rapid nucleation of the tungsten precursors. A clean ceramic boat is loaded with 50 mg of WoO_3 precursor; the Double side polished sapphire substrates were placed on the ceramic boat. Selenium powder was placed

upstream in a ceramic crucible in excess, where the temperature was maintained at 250 °C. High purity Ar (≥99.99%) and H_2 gas were passed at 36 sccm and four sccm flow rates, respectively, during the entire growth process.

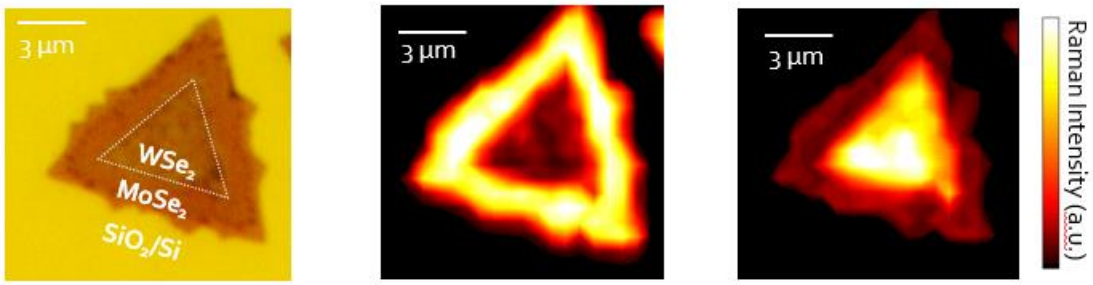

Figure 4.7 Optical Images of TMD Lateral Heterostructure (left) and corresponding Raman maps $MoSe_2$ at 245cm^{-1} (center) and (right) WSe_2 at 250cm^{-1}

The furnace was ramped up with a rate of 30 °C/min to 850 °C and held at 850 °C for 20 minutes before natural cooling to room temperature. After the synthesis, the samples were first characterized using Raman spectroscopy, after which they were loaded into another ceramic boat containing 1mg MoO_3. The new ceramic boat was loaded onto a newer quartz tube to avoid cross-contamination. Selenium precursor was placed upstream in a ceramic crucible in excess, where the temperature was maintained at 300 °C. High purity Ar (≥99.99%) and H_2 were passed at 46 sccm and 4 sccm flow rates, respectively, during the entire growth process.

The furnace was ramped up with a rate of 30 °C/min to 760 °C and held at 760 °C for 13 minutes before natural cooling to room temperature. The $MoSe_2$ grows from the edge of WSe_2, which acts as a nucleation site for the new crystal. Synthesis of lateral

heterostructures takes place in the 750-800 °C temperature regime. Increasing the temperature beyond 800°C result in a vertical growth

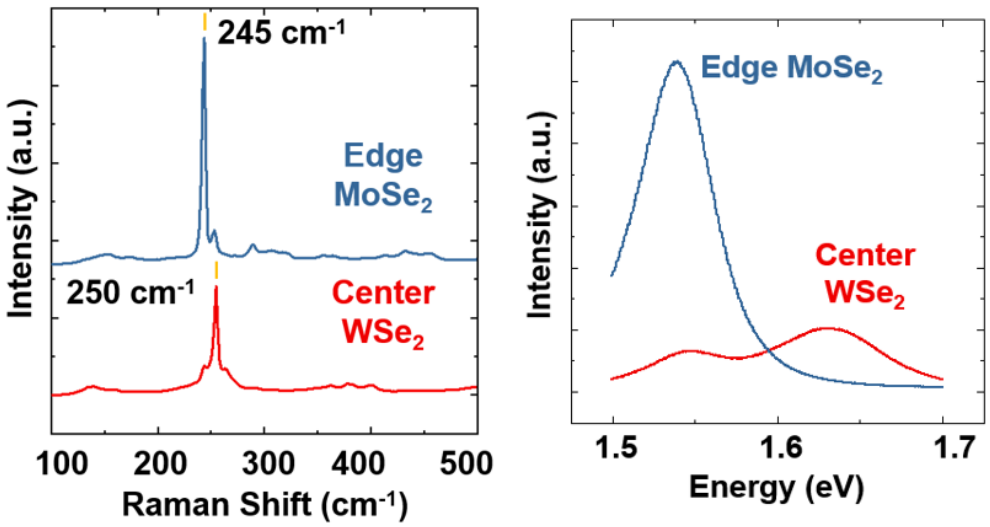

Figure 4.8 Raman Spectra of TMD heterostructure (left) and corresponding PL spectra of TMD heterostructure collected at the edge $MoSe_2$ and center WSe_2

4.4.2. SEAR Synthesis of Janus MoSSe-WSSe Lateral Heterostructure

SEAR synthesis of Janus WSSe MoSSe lateral heterostructure was carried using the modified SEAR chamber. Once again, the processing conditions were changed in order to facilitate the successful conversion of these TMDs into Janus materials. Additionally, the substrates were also kept a greater distance from the plasma tail in order to enable a prolonged etching rate (like the case of $MoSe_2/WSe_2$ vertical heterostructures). The processing time was also increased to twenty minutes in order to facilitate the change. After the successful synthesis of the Janus structures, we characterize them using the Raman Spectroscopy.

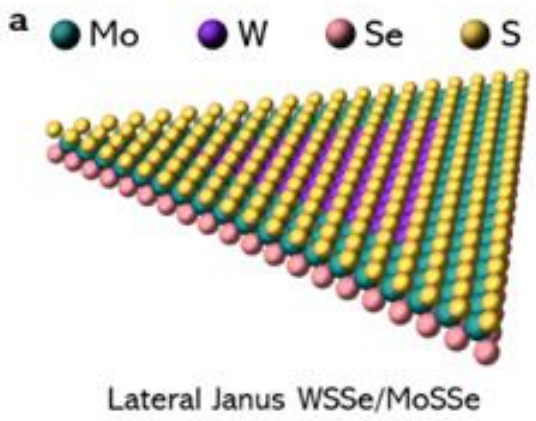

Figure 4.9 Schematic representation of Janus Heterostructure

4.5. Raman & Photoluminescence Spectroscopy

We carried out our established ambient temperature SEAR process on as-synthesized $WSe_2/MoSe_2$ structures to produce Janus lateral heterostructures.

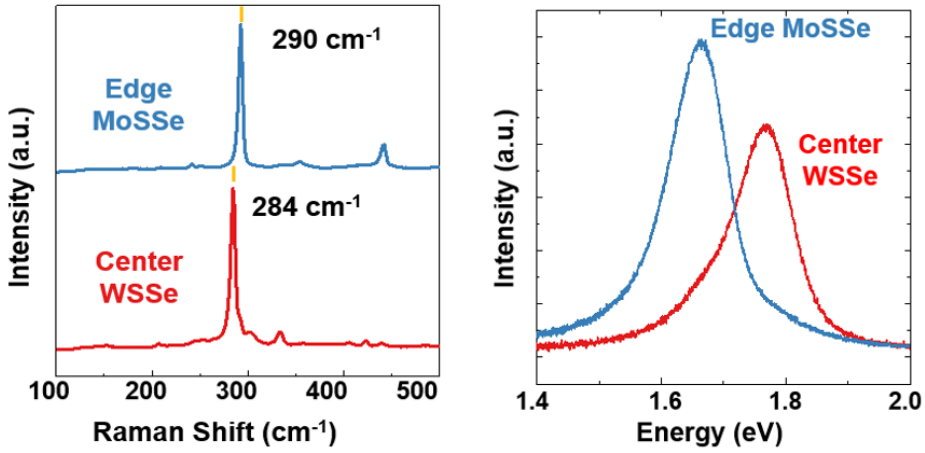

Figure 4.10 Raman Spectra of Janus heterostructure (left) and corresponding PL spectra of collected at the edge MoSSe and center WSSe (right)

Raman mapping characteristic MoSSe A_1 peak (290 cm^{-1}) and WSSe A_1 peak (284 cm^{-1}) confirm the formation of a Janus WSSe/MoSSe lateral heterostructures with WSSe monolayer as the core and MoSSe monolayer being the outer shell.

Similarly, PL spectra acquired from the outer domain and inner domain, show characteristic PL peaks of 2D Janus MoSSe (~1.68 eV) and WSSe (~1.78 eV), and the PL position mapping also reveals the core-shell structure of this unique lateral heterostructure. The PL collected at the MoSSe/WSSe interface shows that emission from individual domains is super-imposed onto each other (red spectra) since the probing spot (1 μm) is much larger than the exciton wavefunction. The presented results, enabled by this simple, scalable, growth process allows us to fabricate first of its kind lateral Janus heterostructures.

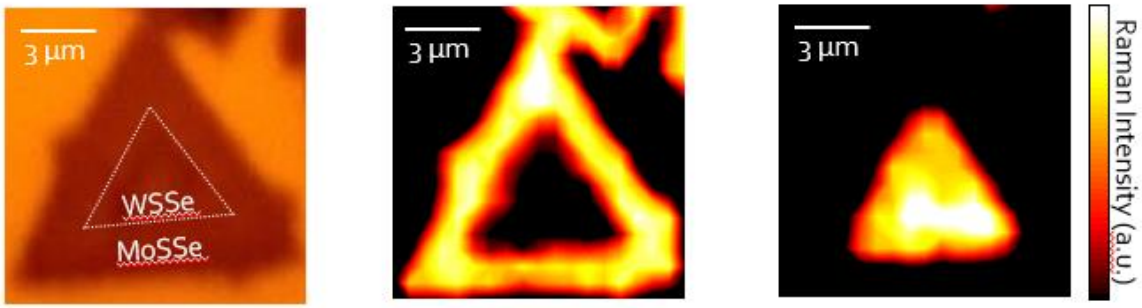

Figure 4.11 Optical Images of janus lateral heterostructure (left) and corresponding Raman maps MoSSe at 290cm^{-1} (center) and WSSe at 284cm^{-1} (right)

Chapter 5 Future Directions and Conclusions

To date, extensive theoretical studies have been done on various aspects of Janus TMDs, and however, due to limitations of previous studies to effectively create a highly crystalline Janus structure, these new properties remained experimentally unknown. The full potential of Two-dimensional Janus materials can now be explored by creating a variety of highly crystalline Janus TMD structures by using the SEAR process mentioned in this work

A critical aspect and one of the key innovations of this methodology is the ability to synthesize large-area and highly crystalline 2D Janus layers and their superlattices without alloying them. Energetically, it is rather easy to alloy chalcogens to form 2D alloys as it has been conventionally done by many research groups. However, the SEAR synthesis will enable researchers to probe many quantum effects arising from 2D Janus layers without any ambiguity.

For establishing better control over the parameters for SEAR few aspects need to be emphasized as reflected below:

1. The level of defects generated during the process can be controlled by manipulating the parameters and thus improving the overall efficiency of the process.
2. The introduction of defects is more likely to be expected when the distance of the sample and the new element is not optimized correctly.
3. Plasma etching rate increases with the increase of the atomic weight of the carrier gas, because the bombardment of a heavier atom can displace or break the bonds and atomic sites very effectively.

4. When a heavier atom weight needs to be incorporated, the pressure and gas flow rate inside the chamber must be raised optimally, at the same time also controlling the other plasma parameters, thus increasing the ion-scattering and thereby reducing the impact energy of the ions being bombarded.
5. Higher flow rate increases the density of plasma up to a certain threshold, followed by a reduction in the energy of plasma due to scattering, at the same time, it would help reduce the impact energy of the ions on the sample, resulting into more gentle stripping and replacement.
6. The application of this innovation will not be limited to replacing Se (one chalcogen) atomic layer with S atoms (another chalcogen). However, it could also be adopted in the future for functionalizing the surface by different elements without altering the parent crystal structure, as demonstrated by our synthesis of vertical and lateral heterostructures. Though care must be taken when trying to incorporate heavy elements into the parent structure.
7. The SEAR technique is extremely versatile in its use, and its principles can be extended to exfoliated TMDs as well as other exotic TMDs (Group V)

Using the established growth process, we may continue to improve the crystal quality of 2D Janus crystals throughout the family to Janus TMDC by optimally playing with the parameters of plasma during the replacement process. To further improve the crystallinity, it is advisable to determine the lowest possible plasma power required to strip-off the top

atomic (chalcogen) layer in order to minimize plasma-induced defects. This versatile technique is flexible enough to synthesize other yet-to-be-discovered 2D Janus crystals.

Lastly, theoretical studies are needed to help stimulate the plasma properties to a more significant extent, such as the induced magnetic field and electrical field from the coil, which could eventually help determine the extent of ionization and dissociation based on the energy generated concerning distance from the coil. This will thus help decide an ideal position for the sample, which has to be etched and the element which must be replaced during the entire process. More efforts must be laid towards the actual kinetics of the mechanism proposed to firm up the conclusions.

Optimum control over the plasma parameters for a different set of element's replacements could be worked out by starting the SEAR process from a parent structure with the different top atomic layer. Janus materials could thus help explore rich quantum physics, which is still unknown to the date. There could now be a possibility to experimentally evidence Rashba splitting by adopting various characterization techniques for these Janus materials. Hetero and Homo structures made from different Janus structures could begin a potential field of piezoelectricity, which could create a significant impact on technological advancements in industries.

In summary, the results from this thesis aim to demonstrate the high-quality synthesis of 2D Janus layers using our room temperature Selective Epitaxy Atomic Replacement Technique (SEAR), and this allows us to synthesize not only 2D Janus MoSSe monolayers but the method can also be expanded to other 2D Janus layers such as WSSe and NbSSe the results in this thesis also highlight the versatility of the room temperature SEAR

technique by fabricating utterly different kind of Janus heterojunction, we demonstrate the growth of high-quality 2D Janus vertical and lateral heterostructures using our room-temperature Selective Epitaxy Atomic Replacement (SEAR) technique. Overall, our technique offers significant advances to the synthesis and fabrication of 2D Janus materials and enables their combination in heterostructures without sacrificing structural or optical quality, thus providing a much-needed platform for the study of unique physical phenomena and further unlocking the transfer of new properties into cutting-edge applications.

REFERENCES

1. Hoffmann R, Kabanov AA, Golov AA, Proserpio DM: Homo Citans and Carbon Allotropes: For an Ethics of Citation. *Angewandte Chemie International Edition* 2016, 55(37):10962-10976.

2. Novoselov KS, Geim AK, Morozov SV, Jiang D, Zhang Y, Dubonos SV, Grigorieva IV, Firsov AA: Electric Field Effect in Atomically Thin Carbon Films. *Science* 2004, 306(5696):666-669.

3. Wallace PR: The band theory of graphite. *Physical review* 1947, 71(9):622.

4. Abergel D, Apalkov V, Berashevich J, Ziegler K, Chakraborty T: Properties of graphene: a theoretical perspective. *Advances in Physics* 2010, 59(4):261-482.

5. Celebi K, Buchheim J, Wyss RM, Droudian A, Gasser P, Shorubalko I, Kye J-I, Lee C, Park HG: Ultimate permeation across atomically thin porous graphene. *Science* 2014, 344(6181):289-292.

6. Geim AK, Novoselov KS: The rise of graphene. *Nature Materials* 2007, 6(3):183-191.

7. Lee C, Wei X, Kysar JW, Hone J: Measurement of the elastic properties and intrinsic strength of monolayer graphene. *science* 2008, 321(5887):385-388.

8. Castro Neto AH, Guinea F, Peres NMR, Novoselov KS, Geim AK: The electronic properties of graphene. *Reviews of Modern Physics* 2009, 81(1):109-162.

9. Wang H, Nezich D, Kong J, Palacios T: Graphene frequency multipliers. *IEEE Electron Device Letters* 2009, 30(5):547-549.

10. Tian J, Jauregui LA, Lopez G, Cao H, Chen YP: Ambipolar graphene field effect transistors by local metal side gates. *Applied Physics Letters* 2010, 96(26):263110.

11. Banszerus L, Schmitz M, Engels S, Dauber J, Oellers M, Haupt F, Watanabe K, Taniguchi T, Beschoten B, Stampfer C: Ultrahigh-mobility graphene devices from chemical vapor deposition on reusable copper. *Science advances* 2015, 1(6):e1500222.

12. Kim K, Choi J-Y, Kim T, Cho S-H, Chung H-J: A role for graphene in silicon-based semiconductor devices. *Nature* 2011, 479(7373):338-344.

13. The nature of the chemical bond and the structure of molecules and crystals, by Linus Pauling. 2nd Edition. xvi + 450 pages. Cornell University Press, Ithaca, N.

Y., 1940. Price, $4.50. *Journal of the American Pharmaceutical Association* 1941, 30(1):30-30.

14. Phillips P: Mottness. *Annals of Physics* 2006, 321(7):1634-1650.

15. Novoselov KS, Geim AK, Morozov S, Jiang D, Katsnelson MI, Grigorieva I, Dubonos S, Firsov, AA: Two-dimensional gas of massless Dirac fermions in graphene. *nature* 2005, 438(7065):197-200.

16. Stone M: Quantum Hall Effect: World Scientific; 1992.

17. Myoung N, Ihm G: Tunneling of Dirac fermions through magnetic barriers in graphene. *Physica E: Low-dimensional Systems and Nanostructures* 2009, 42(1):70-72.

18. Deacon R, Chuang K-C, Nicholas R, Novoselov K, Geim A: Cyclotron resonance study of the electron and hole velocity in graphene monolayers. *Physical Review B* 2007, 76(8):081406.

19. Peres N, Guinea F, Neto AC: Electronic properties of disordered two-dimensional carbon. *Physical Review B* 2006, 73(12):125411.

20. Neto AC, Guinea F, Peres N: Edge and surface states in the quantum Hall effect in graphene. *Physical Review B* 2006, 73(20):205408.

21. Calogeracos A, Dombey N: History and physics of the Klein paradox. *Contemporary physics* 1999, 40(5):313-321.

22. Itzykson C, Zuber J: Quantum Field Theory, Section 5.3. In.: Dover Publications; 2006.

23. Zawadzki W, Rusin TM: Zitterbewegung (trembling motion) of electrons in semiconductors: a review. *Journal of Physics: Condensed Matter* 2011, 23(14):143201.

24. Rydberg H, Dion M, Jacobson N, Schröder E, Hyldgaard P, Simak S, Langreth DC, Lundqvist BI: Van der Waals density functional for layered structures. *Physical review letters* 2003, 91(12):126402.

25. Mak KF, Shan J, Heinz TF: Electronic structure of few-layer graphene: experimental demonstration of strong dependence on stacking sequence. *Physical review letters* 2010, 104(17):176404.

26. Morpurgo A, Kong J, Marcus C, Dai H: Gate-controlled superconducting proximity effect in carbon nanotubes. *Science* 1999, 286(5438):263-265.

27. González J, Perfetto E: Cooper-pair propagation and superconducting correlations in graphene. *Physical Review B* 2007, 76(15):155404.

28. Recher P, Trauzettel B, Rycerz A, Blanter YM, Beenakker C, Morpurgo A: Aharonov-Bohm effect and broken valley degeneracy in graphene rings. *Physical Review B* 2007, 76(23):235404.

29. Kharitonov MY, Efetov KB: Universal conductance fluctuations in graphene. *Physical Review B* 2008, 78(3):033404.

30. Nam Y, Yoo JS, Park YW, Lindvall N, Bauch T, Yurgens A: The Aharonov-Bohm effect in graphene rings with metal mirrors. *Carbon* 2012, 50(15):5562-5568.

31. Rickhaus P, Maurand R, Liu M-H, Weiss M, Richter K, Schönenberger C: Ballistic interferences in suspended graphene. *Nature communications* 2013, 4(1):1-6.

32. Wunsch B, Stauber T, Guinea F: Electron-electron interactions and charging effects in graphene quantum dots. *Physical Review B* 2008, 77(3):035316.

33. Güttinger J, Frey T, Stampfer C, Ihn T, Ensslin K: Spin states in graphene quantum dots. *Physical review letters* 2010, 105(11):116801.

34. Trauzettel B, Bulaev DV, Loss D, Burkard G: Spin qubits in graphene quantum dots. *Nature Physics* 2007, 3(3):192-196.

35. Chen J-H, Li L, Cullen WG, Williams ED, Fuhrer MS: Tunable Kondo effect in graphene with defects. *Nature Physics* 2011, 7(7):535-538.

36. Sols F, Guinea F, Neto AC: Coulomb blockade in graphene nanoribbons. *Physical Review Letters* 2007, 99(16):166803.

37. Manzeli S, Ovchinnikov D, Pasquier D, Yazyev OV, Kis A: 2D transition metal dichalcogenides. *Nature Reviews Materials* 2017, 2(8):17033.

38. Zurutuza A, Marinelli C: Challenges and opportunities in graphene commercialization. *Nature nanotechnology* 2014, 9(10):730-734.

39. Xu M, Liang T, Shi M, Chen H: Graphene-like two-dimensional materials. *Chemical reviews* 2013, 113(5):3766-3798.

40. Fiori G, Bonaccorso F, Iannaccone G, Palacios T, Neumaier D, Seabaugh A, Banerjee SK, Colombo L: Electronics based on two-dimensional materials. *Nature nanotechnology* 2014, 9(10):768.

41. Mak KF, Shan J: Photonics and optoelectronics of 2D semiconductor transition metal dichalcogenides. *Nature Photonics* 2016, 10(4):216.

42. Schaibley JR, Yu H, Clark G, Rivera P, Ross JS, Seyler KL, Yao W, Xu X: Valleytronics in 2D materials. *Nature Reviews Materials* 2016, 1(11):1-15.

43. Liu X, Hersam MC: 2D materials for quantum information science. *Nature Reviews Materials* 2019, 4(10):669-684.

44. Hong X, Kim J, Shi S-F, Zhang Y, Jin C, Sun Y, Tongay S, Wu J, Zhang Y, Wang F: Ultrafast charge transfer in atomically thin MoS 2/WS 2 heterostructures. *Nature nanotechnology* 2014, 9(9):682-686.

45. Geim AK, Grigorieva IV: Van der Waals heterostructures. *Nature* 2013, 499(7459):419-425.

46. Gupta A, Sakthivel T, Seal S: Recent development in 2D materials beyond graphene. *Progress in Materials Science* 2015, 73:44-126.

47. Miró P, Audiffred M, Heine T: An atlas of two-dimensional materials. *Chemical Society Reviews* 2014, 43(18):6537-6554.

48. Tanjil MR-E, Jeong Y, Yin Z, Panaccione W, Wang MC: Ångström-Scale, Atomically Thin 2D Materials for Corrosion Mitigation and Passivation. *Coatings* 2019, 9(2):133.

49. Gan Z, Liu L, Wu H, Hao Y, Shan Y, Wu X, Chu PK: Quantum confinement effects across two-dimensional planes in MoS2 quantum dots. *Applied Physics Letters* 2015, 106(23):233113.

50. Kang J, Tongay S, Li J, Wu J: Monolayer semiconducting transition metal dichalcogenide alloys: Stability and band bowing. *Journal of Applied Physics* 2013, 113(14):143703.

51. Luo X, Zhao Y, Zhang J, Toh M, Kloc C, Xiong Q, Quek SY: Effects of lower symmetry and dimensionality on Raman spectra in two-dimensional WSe 2. *Physical Review B* 2013, 88(19):195313.

52. Wang G, Chernikov A, Glazov MM, Heinz TF, Marie X, Amand T, Urbaszek B: Colloquium: Excitons in atomically thin transition metal dichalcogenides. *Reviews of Modern Physics* 2018, 90(2):021001.

53. Splendiani A, Sun L, Zhang Y, Li T, Kim J, Chim C-Y, Galli G, Wang F: Emerging photoluminescence in monolayer MoS2. *Nano letters* 2010, 10(4):1271-1275.

54. Latzke DW, Zhang W, Suslu A, Chang T-R, Lin H, Jeng H-T, Tongay S, Wu J, Bansil A, Lanzara A: Electronic structure, spin-orbit coupling, and interlayer interaction in bulk MoS 2 and WS 2. *Physical Review B* 2015, 91(23):235202.

55. Chhowalla M, Liu Z, Zhang H: Two-dimensional transition metal dichalcogenide (TMD) nanosheets. *Chemical Society Reviews* 2015, 44(9):2584-2586.

56. Kan M, Nam HG, Lee YH, Sun Q: Phase stability and Raman vibration of the molybdenum ditelluride (MoTe 2) monolayer. *Physical Chemistry Chemical Physics* 2015, 17(22):14866-14871.

57. Kuc A, Zibouche N, Heine T: Influence of quantum confinement on the electronic structure of the transition metal sulfide T S 2. *Physical Review B* 2011, 83(24):245213.

58. Friend R, Yoffe A: Electronic properties of intercalation complexes of the transition metal dichalcogenides. *Advances in Physics* 1987, 36(1):1-94.

59. Jiang L, Lin B, Li X, Song X, Xia H, Li L, Zeng H: Monolayer MoS2–graphene hybrid aerogels with controllable porosity for lithium-ion batteries with high reversible capacity. *ACS applied materials & interfaces* 2016, 8(4):2680-2687.

60. Park J, Choudhary N, Smith J, Lee G, Kim M, Choi W: Thickness modulated MoS2 grown by chemical vapor deposition for transparent and flexible electronic devices. *Applied Physics Letters* 2015, 106(1):012104.

61. Ghatak S, Pal AN, Ghosh A: Nature of electronic states in atomically thin MoS2 field-effect transistors. *ACS nano* 2011, 5(10):7707-7712.

62. Late DJ, Liu B, Matte HR, Dravid VP, Rao C: Hysteresis in single-layer MoS2 field effect transistors. *ACS nano* 2012, 6(6):5635-5641.

63. Frindt R, Yoffe A: Physical properties of layer structures: optical properties and photoconductivity of thin crystals of molybdenum disulphide. *Proceedings of the Royal Society of London Series A Mathematical and Physical Sciences* 1963, 273(1352):69-83.

64. Allen MJ, Tung VC, Kaner RB: Honeycomb carbon: a review of graphene. *Chemical reviews* 2010, 110(1):132-145.

65. Li H, Wu J, Yin Z, Zhang H: Preparation and applications of mechanically exfoliated single-layer and multilayer MoS2 and WSe2 nanosheets. *Accounts of chemical research* 2014, 47(4):1067-1075.

66. Yi M, Shen Z: A review on mechanical exfoliation for the scalable production of graphene. *Journal of Materials Chemistry A* 2015, 3(22):11700-11715.

67. Kan M, Wang J, Li X, Zhang S, Li Y, Kawazoe Y, Sun Q, Jena P: Structures and phase transition of a MoS2 monolayer. *The Journal of Physical Chemistry C* 2014, 118(3):1515-1522.

68. Lembke D, Bertolazzi S, Kis A: Single-layer MoS2 electronics. *Accounts of chemical research* 2015, 48(1):100-110.

69. Jawaid A, Nepal D, Park K, Jespersen M, Qualley A, Mirau P, Drummy LF, Vaia RA: Mechanism for liquid phase exfoliation of MoS2. *Chemistry of Materials* 2016, 28(1):337-348.

70. Imanishi N, Toyoda M, Takeda Y, Yamamoto O: Study on lithium intercalation into MoS2. *Solid State Ionics* 1992, 58(3-4):333-338.

71. Zhan B, Li C, Yang J, Jenkins G, Huang W, Dong X: Graphene field-effect transistor and its application for electronic sensing. *Small* 2014, 10(20):4042-4065.

72. He Q, Zeng Z, Yin Z, Li H, Wu S, Huang X, Zhang H: Fabrication of flexible MoS2 thin-film transistor arrays for practical gas-sensing applications. *Small* 2012, 8(19):2994-2999.

73. Ray S: First-principles study of MoS2, phosphorene and graphene based single electron transistor for gas sensing applications. *Sensors and Actuators B: Chemical* 2016, 222:492-498.

74. Liu Y, Hao L, Gao W, Xue Q, Guo W, Wu Z, Lin Y, Zeng H, Zhu J, Zhang W: Electrical characterization and ammonia sensing properties of MoS2/Si p–n junction. *Journal of Alloys and Compounds* 2015, 631:105-110.

75. Wang Y, Cong C, Yang W, Shang J, Peimyoo N, Chen Y, Kang J, Wang J, Huang W, Yu T: Strain-induced direct–indirect bandgap transition and phonon modulation in monolayer WS 2. *Nano Research* 2015, 8(8):2562-2572.

76. Gutiérrez HR, Perea-López N, Elías AL, Berkdemir A, Wang B, Lv R, López-Urías F, Crespi VH, Terrones H, Terrones M: Extraordinary room-temperature

photoluminescence in triangular WS2 monolayers. *Nano letters* 2013, 13(8):3447-3454.

77. Kumar A, Ahluwalia P: Electronic structure of transition metal dichalcogenides monolayers 1H-MX 2 (M= Mo, W; X= S, Se, Te) from ab-initio theory: new direct band gap semiconductors. *The European Physical Journal B* 2012, 85(6):186.

78. Roldán R, Silva-Guillén JA, López-Sancho MP, Guinea F, Cappelluti E, Ordejón P: Electronic properties of single-layer and multilayer transition metal dichalcogenides MX2 (M = Mo, W and X = S, Se). *Annalen der Physik* 2014, 526(9-10):347-357.

79. Yu L, Zubair A, Santos EJ, Zhang X, Lin Y, Zhang Y, Palacios T: High-performance WSe2 complementary metal oxide semiconductor technology and integrated circuits. *Nano letters* 2015, 15(8):4928-4934.

80. Gil CJ, Pham A, Yu A, Li S: An ab initio study of transition metals doped with WSe2 for long-range room temperature ferromagnetism in two-dimensional transition metal dichalcogenide. *Journal of Physics: Condensed Matter* 2014, 26(30):306004.

81. Lei B, Hu Z, Xiang D, Wang J, Eda G, Han C, Chen W: Significantly enhanced optoelectronic performance of tungsten diselenide phototransistor via surface functionalization. *Nano Research* 2017, 10(4):1282-1291.

82. Yang M, Zhao R, Wang J, Zhang L, Xie Q, Liu Z, Liu Z: Bandgap opening in Janus-type mosaic graphene. *Journal of Applied Physics* 2013, 113(8):084313.

83. Guo Y, Zhou S, Bai Y, Zhao J: Enhanced piezoelectric effect in Janus group-III chalcogenide monolayers. *Applied Physics Letters* 2017, 110(16):163102.

84. Idrees M, Din H, Ali R, Rehman G, Hussain T, Nguyen C, Ahmad I, Amin B: Optoelectronic and solar cell applications of Janus monolayers and their van der Waals heterostructures. *Physical Chemistry Chemical Physics* 2019, 21(34):18612-18621.

85. Yagmurcukardes M, Qin Y, Ozen S, Sayyad M, Peeters FM, Tongay S, Sahin H: Quantum properties and applications of 2D Janus crystals and their superlattices. *Applied Physics Reviews* 2020, 7(1):011311.

86. Bui HD, Jappor HR, Hieu NN: Tunable optical and electronic properties of Janus monolayers Ga2SSe, Ga2STe, and Ga2SeTe as promising candidates for ultraviolet photodetectors applications. *Superlattices and Microstructures* 2019, 125:1-7.

87. Casagrande C, Fabre P, Raphael E, Veyssié M: “Janus beads”: realization and behaviour at water/oil interfaces. *EPL (Europhysics Letters)* 1989, 9(3):251.

88. Sofo JO, Chaudhari AS, Barber GD: Graphane: A two-dimensional hydrocarbon. *Physical Review B* 2007, 75(15):153401.

89. Peng Q, Dearden AK, Crean J, Han L, Liu S, Wen X, De S: New materials graphyne, graphdiyne, graphone, and graphane: review of properties, synthesis, and application in nanotechnology. *Nanotechnology, science and applications* 2014, 7:1.

90. Podlivaev A, Openov L: On the thermal stability of graphone. *Semiconductors* 2011, 45(7):958-961.

91. Xiang H, Kan E, Wei S-H, Gong X, Whangbo M-H: Thermodynamically stable single-side hydrogenated graphene. *Physical Review B* 2010, 82(16):165425.

92. Yang M, Zhou L, Wang J, Liu Z, Liu Z: Evolutionary chlorination of graphene: from charge-transfer complex to covalent bonding and nonbonding. *The Journal of Physical Chemistry C* 2012, 116(1):844-850.

93. Pumera M, Wong CHA: Graphane and hydrogenated graphene. *Chemical Society Reviews* 2013, 42(14):5987-5995.

94. Wheeler V, Garces N, Nyakiti L, Myers-Ward R, Jernigan G, Culbertson J, Eddy Jr C, Gaskill DK: Fluorine functionalization of epitaxial graphene for uniform deposition of thin high-κ dielectrics. *Carbon* 2012, 50(6):2307-2314.

95. Zhou J, Wang Q, Sun Q, Jena P: Electronic and magnetic properties of a BN sheet decorated with hydrogen and fluorine. *Physical Review B* 2010, 81(8):085442.

96. Jiang J, Liu Z, Sun Y, Yang H, Rajamathi C, Qi Y, Yang L, Chen C, Peng H, Hwang C: Signature of type-II Weyl semimetal phase in MoTe 2. *Nature communications* 2017, 8:13973.

97. Neto AC: Charge density wave, superconductivity, and anomalous metallic behavior in 2D transition metal dichalcogenides. *Physical review letters* 2001, 86(19):4382.

98. Xi X, Wang Z, Zhao W, Park J-H, Law KT, Berger H, Forró L, Shan J, Mak KF: Ising pairing in superconducting NbSe 2 atomic layers. *Nature Physics* 2016, 12(2):139-143.

99. Zhu Z, Cheng Y, Schwingenschlögl U: Giant spin-orbit-induced spin splitting in two-dimensional transition-metal dichalcogenide semiconductors. *Physical Review B* 2011, 84(15):153402.

100. Guo S-D: Phonon transport in Janus monolayer MoSSe: a first-principles study. *Physical Chemistry Chemical Physics* 2018, 20(10):7236-7242.

101. He J, Li S: Two-dimensional Janus transition-metal dichalcogenides with intrinsic ferromagnetism and half-metallicity. *Computational Materials Science* 2018, 152:151-157.

102. Li R, Cheng Y, Huang W: Recent progress of Janus 2D transition metal chalcogenides: From theory to experiments. *Small* 2018, 14(45):1802091.

103. Bychkov YA, Rashba ÉI: Properties of a 2D electron gas with lifted spectral degeneracy. *JETP lett* 1984, 39(2):78.

104. Bychkov YA, Rashba VMnE: Effect of spin-orbit coupling on the energy spectrum of a 2D electron system in a tilted magnetic field. *Zh Eksp Teor Fiz* 1990, 98:726.

105. Cheng Y, Zhu Z, Tahir M, Schwingenschlögl U: Spin-orbit–induced spin splittings in polar transition metal dichalcogenide monolayers. *EPL (Europhysics Letters)* 2013, 102(5):57001.

106. McGuire T, Potter R: Anisotropic magnetoresistance in ferromagnetic 3d alloys. *IEEE Transactions on Magnetics* 1975, 11(4):1018-1038.

107. Schliemann J, Loss D: Anisotropic transport in a two-dimensional electron gas in the presence of spin-orbit coupling. *Physical Review B* 2003, 68(16):165311.

108. Trushin M, Výborný K, Moraczewski P, Kovalev AA, Schliemann J, Jungwirth T: Anisotropic magnetoresistance of spin-orbit coupled carriers scattered from polarized magnetic impurities. *Physical Review B* 2009, 80(13):134405.

109. Eremeev S, Nechaev I, Chulkov E: Giant Rashba-type spin splitting at polar surfaces of BiTel. *Письма в Журнал экспериментальной и теоретической физики* 2012, 96(7-8):484-491.

110. Liu Q, Guo Y, Freeman AJ: Tunable Rashba effect in two-dimensional LaOBiS2 films: ultrathin candidates for spin field effect transistors. *Nano letters* 2013, 13(11):5264-5270.

111. Chen J, Wu K, Ma H, Hu W, Yang J: Tunable Rashba spin splitting in Janus transition-metal dichalcogenide monolayers via charge doping. *RSC Advances* 2020, 10(11):6388-6394.

112. Chen W: Topological pairings in Janus monolayer TaSSe. *arXiv preprint arXiv:190709925* 2019.

113. Zhou BT, Taguchi K, Kawaguchi Y, Tanaka Y, Law K: Spin-orbit coupling induced valley Hall effects in transition-metal dichalcogenides. *Communications Physics* 2019, 2(1):1-7.

114. Ishizaka K, Bahramy M, Murakawa H, Sakano M, Shimojima T, Sonobe T, Koizumi K, Shin S, Miyahara H, Kimura A: Giant Rashba-type spin splitting in bulk BiTeI. *Nature materials* 2011, 10(7):521.

115. Yao Q-F, Cai J, Tong W-Y, Gong S-J, Wang J-Q, Wan X, Duan C-G, Chu J: Manipulation of the large Rashba spin splitting in polar two-dimensional transition-metal dichalcogenides. *Physical Review B* 2017, 95(16):165401.

116. Absor MAU, Kotaka H, Ishii F, Saito M: Tunable spin splitting and spin lifetime in polar WSTe monolayer. *Japanese Journal of Applied Physics* 2018, 57(4S):04FP01.

117. Zhou W, Chen J, Yang Z, Liu J, Ouyang F: Geometry and electronic structure of monolayer, bilayer, and multilayer Janus WSSe. *Physical Review B* 2019, 99(7):075160.

118. Fei Z, Huang B, Malinowski P, Wang W, Song T, Sanchez J, Yao W, Xiao D, Zhu X, May AF: Two-dimensional itinerant ferromagnetism in atomically thin Fe 3 GeTe 2. *Nature materials* 2018, 17(9):778-782.

119. Yu XZ, Kanazawa N, Zhang WZ, Nagai T, Hara T, Kimoto K, Matsui Y, Onose Y, Tokura Y: Skyrmion flow near room temperature in an ultralow current density. *Nature Communications* 2012, 3(1):988.

120. Maier TA, Jarrell M, Schulthess T, Kent P, White J: Systematic study of d-wave superconductivity in the 2d repulsive hubbard model. *Physical review letters* 2005, 95(23):237001.

121. Obokata T, Ono I, Oguchi T: Padé approximation to ferromagnet with anisotropic exchange interaction. *Journal of the Physical Society of Japan* 1967, 23(3):516-521.

122. Zaspel C: Mobile nonlinear excitations in the two-dimensional isotropic Heisenberg ferromagnet. *Physical Review B* 1993, 48(2):926.

123. Gong C, Li L, Li Z, Ji H, Stern A, Xia Y, Cao T, Bao W, Wang C, Wang Y: Discovery of intrinsic ferromagnetism in two-dimensional van der Waals crystals. *Nature* 2017, 546(7657):265.

124. Huang B, Clark G, Navarro-Moratalla E, Klein DR, Cheng R, Seyler KL, Zhong D, Schmidgall E, McGuire MA, Cobden DH: Layer-dependent ferromagnetism in a van der Waals crystal down to the monolayer limit. *Nature* 2017, 546(7657):270.

125. Bonilla M, Kolekar S, Ma Y, Diaz HC, Kalappattil V, Das R, Eggers T, Gutierrez HR, Phan M-H, Batzill M: Strong room-temperature ferromagnetism in VSe 2 monolayers on van der Waals substrates. *Nature nanotechnology* 2018, 13(4):289.

126. O'Hara DJ, Zhu T, Trout AH, Ahmed AS, Luo YK, Lee CH, Brenner MR, Rajan S, Gupta JA, McComb DW: Room temperature intrinsic ferromagnetism in epitaxial manganese selenide films in the monolayer limit. *Nano letters* 2018, 18(5):3125-3131.

127. Deng Y, Yu Y, Song Y, Zhang J, Wang NZ, Sun Z, Yi Y, Wu YZ, Wu S, Zhu J: Gate-tunable room-temperature ferromagnetism in two-dimensional Fe 3 GeTe 2. *Nature* 2018, 563(7729):94.

128. Fei Z, Huang B, Malinowski P, Wang W, Song T, Sanchez J, Yao W, Xiao D, Zhu X, May AF: Two-dimensional itinerant ferromagnetism in atomically thin Fe 3 GeTe 2. *Nature materials* 2018, 17(9):778.

129. Zhang C, Nie Y, Sanvito S, Du A: First-Principles Prediction of a Room-Temperature Ferromagnetic Janus VSSe Monolayer with Piezoelectricity, Ferroelasticity, and Large Valley Polarization. *Nano letters* 2019, 19(2):1366-1370.

130. Moaied M, Lee J, Hong J: A 2D ferromagnetic semiconductor in monolayer Cr-trihalide and its Janus structures. *Physical Chemistry Chemical Physics* 2018, 20(33):21755-21763.

131. Liang J, Chshiev M, Fert A, Yang H: Very large Dzyaloshinskii-Moriya interaction in two-dimensional Janus manganese dichalcogenides and its application to realize field-free skyrmions. *arXiv preprint arXiv:190600648* 2019.

132. Yuan J, Yang Y, Wu Y, Feng YP, Chen Y, Yan X, Shen L: Zero-field Sub-50-nm Skyrmions in Monolayer Janus Van der Waals Magnets. *arXiv preprint arXiv:190610836* 2019.

133. Huang P, Zhang P, Xu S, Wang H, Zhang X, Zhang H: Recent advances in two-dimensional ferromagnetism: materials synthesis, physical properties and device applications. *Nanoscale* 2020, 12(4):2309-2327.

134. Tong Q, Chen M, Yao W: Magnetic Proximity Effect in a van der Waals Moir\'e Superlattice. *Physical Review Applied* 2019, 12(2):024031.

135. Tong Q, Liu F, Xiao J, Yao W: Skyrmions in the Moiré of van der Waals 2D Magnets. *Nano Letters* 2018, 18(11):7194-7199.

136. Schaibley JR, Yu H, Clark G, Rivera P, Ross JS, Seyler KL, Yao W, Xu X: Valleytronics in 2D materials. *Nature Reviews Materials* 2016, 1(11):16055.

137. Laheld U, Pedersen F, Hemmer PC: Excitons in type-ii quantum dots: Finite offsets. *Physical Review B* 1995, 52(4):2697.

138. Xiao J, Wang Y, Wang H, Pemmaraju C, Wang S, Muscher P, Sie EJ, Nyby CM, Devereaux TP, Qian X: Berry curvature memory via electrically driven stacking transitions. *arXiv preprint arXiv:191201037* 2019.

139. Xia C, Xiong W, Du J, Wang T, Peng Y, Li J: Universality of electronic characteristics and photocatalyst applications in the two-dimensional Janus transition metal dichalcogenides. *Physical Review B* 2018, 98(16):165424.

140. Riis-Jensen AC, Pandey M, Thygesen KS: Efficient Charge Separation in 2D Janus van der Waals Structures with Built-in Electric Fields and Intrinsic p–n Doping. *The Journal of Physical Chemistry C* 2018, 122(43):24520-24526.

141. Dong L, Lou J, Shenoy VB: Large in-plane and vertical piezoelectricity in Janus transition metal dichalchogenides. *ACS nano* 2017, 11(8):8242-8248.

142. Luo YF, Pang Y, Tang M, Song Q, Wang M: Electronic properties of Janus MoSSe nanotubes. *Computational Materials Science* 2019, 156:315-320.

143. Tang ZK, Wen B, Chen M, Liu LM: Janus MoSSe nanotubes: tunable band gap and excellent optical properties for surface photocatalysis. *Advanced Theory and Simulations* 2018, 1(10):1800082.

144. Peng J, Chen X, Ong W-J, Zhao X, Li N: Surface and heterointerface engineering of 2D MXenes and their nanocomposites: insights into electro-and photocatalysis. *Chem* 2019, 5(1):18-50.

145. Zhang J, Jia S, Kholmanov I, Dong L, Er D, Chen W, Guo H, Jin Z, Shenoy VB, Shi L *et al*: Janus Monolayer Transition-Metal Dichalcogenides. *ACS Nano* 2017, 11(8):8192-8198.

146. Lu A-Y, Zhu H, Xiao J, Chuu C-P, Han Y, Chiu M-H, Cheng C-C, Yang C-W, Wei K-H, Yang Y *et al*: Janus monolayers of transition metal dichalcogenides. *Nature Nanotechnology* 2017, 12(8):744-749.

147. Varshni YP: Temperature dependence of the energy gap in semiconductors. *Physica* 1967, 34(1):149-154.

148. Poulsen R: Plasma etching in integrated circuit manufacture—A review. *Journal of Vacuum Science and Technology* 1977, 14(1):266-274.

149. Pelletier J, Anders A: Plasma-based ion implantation and deposition: A review of physics, technology, and applications. *IEEE Transactions on Plasma Science* 2005, 33(6):1944-1959.

150. Yang JG, Hoffman DJ, Carducci JD, Buchberger Jr DA, Miller ML, Chiang K-L, Delgadino GA, Hagen RB: Capacitively coupled plasma reactor with uniform radial distribution of plasma. In.: Google Patents; 2005.

151. Bergeron K: Theory of the secondary electron avalanche at electrically stressed insulator-vacuum interfaces. *Journal of Applied Physics* 1977, 48(7):3073-3080.

152. Eliasson B, Kogelschatz U: Modeling and applications of silent discharge plasmas. *IEEE transactions on plasma science* 1991, 19(2):309-323.

153. Coburn J: Surface processing with partially ionized plasmas. *IEEE transactions on plasma science* 1991, 19(6):1048-1062.

154. Bukowski J, Graves D, Vitello P: Two-dimensional fluid model of an inductively coupled plasma with comparison to experimental spatial profiles. *Journal of Applied Physics* 1996, 80(5):2614-2623.

155. Shul R, McClellan G, Casalnuovo S, Rieger D, Pearton S, Constantine C, Barratt C, Karlicek Jr R, Tran C, Schurman M: Inductively coupled plasma etching of GaN. *Applied physics letters* 1996, 69(8):1119-1121.

156. Smith S, Wolden C, Bremser M, Hanser A, Davis R, Lampert W: High rate and selective etching of GaN, AlGaN, and AlN using an inductively coupled plasma. *Applied physics letters* 1997, 71(25):3631-3633.

157. Perry A, Boswell R: Fast anisotropic etching of silicon in an inductively coupled plasma reactor. *Applied physics letters* 1989, 55(2):148-150.

158. Meziani T, Colpo P, Rossi F: Design of a magnetic-pole enhanced inductively coupled plasma source. *Plasma Sources Science and Technology* 2001, 10(2):276.

159. Penkov OV, Khadem M, Lim W-S, Kim D-E: A review of recent applications of atmospheric pressure plasma jets for materials processing. *Journal of Coatings Technology and Research* 2015, 12(2):225-235.

160. Lee C, Gu E, Dawson M, Friel I, Scarsbrook G: Etching and micro-optics fabrication in diamond using chlorine-based inductively-coupled plasma. *Diamond and Related Materials* 2008, 17(7-10):1292-1296.

161. Lei F, Li X, Liu Y, Liu D, Yang M, Yu Y: Simulation of a large size inductively coupled plasma generator and comparison with experimental data. *AIP Advances* 2018, 8(1):015003.

162. Lu A-Y, Zhu H, Xiao J, Chuu C-P, Han Y, Chiu M-H, Cheng C-C, Yang C-W, Wei K-H, Yang Y: Janus monolayers of transition metal dichalcogenides. *Nature nanotechnology* 2017, 12(8):744-749.

163. Liu W, Liu M, OuYang Y, Hou H, Lei M, Wei Z: CVD-grown MoSe2 with high modulation depth for ultrafast mode-locked erbium-doped fiber laser. *Nanotechnology* 2018, 29(39):394002.

164. Utama MIB, Lu X, Yuan Y, Xiong Q: Detrimental influence of catalyst seeding on the device properties of CVD-grown 2D layered materials: A case study on MoSe2. *Applied Physics Letters* 2014, 105(25):253102.

165. Tao L, Chen K, Chen Z, Chen W, Gui X, Chen H, Li X, Xu J-B: Centimeter-scale CVD growth of highly crystalline single-layer MoS2 film with spatial homogeneity and the visualization of grain boundaries. *ACS applied materials & interfaces* 2017, 9(13):12073-12081.

166. Özden A, Ay F, Sevik C, Perkgöz NK: CVD growth of monolayer MoS2: role of growth zone configuration and precursors ratio. *Japanese Journal of Applied Physics* 2017, 56(6S1):06GG05.

167. Li F, Wei W, Zhao P, Huang B, Dai Y: Electronic and optical properties of pristine and vertical and lateral heterostructures of Janus MoSSe and WSSe. *The journal of physical chemistry letters* 2017, 8(23):5959-5965.

168. Li F, Wei W, Wang H, Huang B, Dai Y, Jacob T: Intrinsic Electric Field-Induced Properties in Janus MoSSe van der Waals Structures. *The journal of physical chemistry letters* 2019, 10(3):559-565.

169. Chernikov A, Berkelbach TC, Hill HM, Rigosi A, Li Y, Aslan OB, Reichman DR, Hybertsen MS, Heinz TF: Exciton binding energy and nonhydrogenic Rydberg series in monolayer WS 2. *Physical review letters* 2014, 113(7):076802.

170. Mak KF, He K, Lee C, Lee GH, Hone J, Heinz TF, Shan J: Tightly bound trions in monolayer MoS 2. *Nature materials* 2013, 12(3):207-211.

171. Ross JS, Wu S, Yu H, Ghimire NJ, Jones AM, Aivazian G, Yan J, Mandrus DG, Xiao D, Yao W: Electrical control of neutral and charged excitons in a monolayer semiconductor. *Nature communications* 2013, 4(1):1-6.

172. Berkelbach TC, Hybertsen MS, Reichman DR: Theory of neutral and charged excitons in monolayer transition metal dichalcogenides. *Physical Review B* 2013, 88(4):045318.

173. Perea-López N, Lin Z, Pradhan NR, Iñiguez-Rábago A, Elías AL, McCreary A, Lou J, Ajayan PM, Terrones H, Balicas L: CVD-grown monolayered MoS2 as an effective photosensor operating at low-voltage. *2D Materials* 2014, 1(1):011004.

174. Wei X, Yu Z, Hu F, Cheng Y, Yu L, Wang X, Xiao M, Wang J, Wang X, Shi Y: Mo-O bond doping and related-defect assisted enhancement of photoluminescence in monolayer MoS2. *Aip Advances* 2014, 4(12):123004.